

AD-762 453

REMOTE TECHNIQUES FOR CAPILLARY WAVE
MEASUREMENT

Kamala S. Krishnan, et al

Stanford Research Institute

Prepared for:

Office of Naval Research
Defense Advanced Research Projects Agency

2 April 1973

DISTRIBUTED BY:

NTIS

National Technical Information Service
U. S. DEPARTMENT OF COMMERCE
5285 Port Royal Road, Springfield Va. 22151

Technical Report

Covering the Period 21 May to 31 December 1972

REMOTE TECHNIQUES FOR CAPILLARY WAVE MEASUREMENT

By: K. S. KRISHNAN and N. A. PEPPERS

Prepared for:

OFFICE OF NAVAL RESEARCH
DEPARTMENT OF THE NAVY
ARLINGTON, VIRGINIA 22217

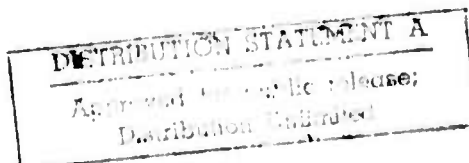
Attention: MR. JOHN J. KANE
FIELD PROJECTS PROGRAM, CODE 418



Sponsored by:

DEFENSE ADVANCED RESEARCH PROJECTS AGENCY
ARPA ORDER NO. 2185

Reproduced by
NATIONAL TECHNICAL
INFORMATION SERVICE
U S Department of Commerce
Springfield VA 22151



STANFORD RESEARCH INSTITUTE
Menlo Park, California 94025 • U.S.A.



STANFORD RESEARCH INSTITUTE
Menlo Park, California 94025 · U.S.A.

Technical Report

Covering the Period 21 May to 31 December 1972

April 2, 1973

REMOTE TECHNIQUES FOR CAPILLARY WAVE MEASUREMENT

By: K. S. KRISHNAN and N. A. PEPPERS

Prepared for:

OFFICE OF NAVAL RESEARCH
DEPARTMENT OF THE NAVY
ARLINGTON, VIRGINIA 22217

Attention: MR. JOHN J. KANE
FIELD PROJECTS PROGRAM, CODE 418

Sponsored by:

DEFENSE ADVANCED RESEARCH PROJECTS AGENCY

ARPA ORDER NO. 2185

CONTRACT N00014-70-C-0413

Modification No. P00007

Contract Amount \$45,000*

Program Code Nos. 1N10, 2E20

21 May 1972 — 31 December 1972

SRI Project ERU 8727-100

*Supplementary to the \$2,500,081.00 funded under ARPA Order No. 1856 covered in separate reports.

The views and conclusions contained in this document are those of the authors and should not be interpreted as necessarily representing the official policies, either expressed or implied, of the Advanced Research Projects Agency of the U.S. Government.

Approved by:

EARLE D. JONES, *Director*
Electronics and Bioengineering Laboratory

BONNAR T. COX, *Executive Director*
Information Sciences and Engineering Division

UNCLASSIFIED

Security Classification

AD 762453

DOCUMENT CONTROL DATA - R & D

(Security classification of title, body of abstract and indexing annotation must be entered when the overall report is classified)

1. ORIGINATING ACTIVITY (Corporate author) Stanford Research Institute 333 Ravenswood Avenue Menlo Park, California 94025		2a. REPORT SECURITY CLASSIFICATION Unclassified	
3. REPORT TITLE REMOTE TECHNIQUES FOR CAPILLARY WAVE MEASUREMENT		2b. GROUP	
4. DESCRIPTIVE NOTES (Type of report and inclusive dates) Technical Report 21 May 1972 - 31 December 1972			
5. AUTHOR(S) (First name, middle initial, last name) Kamala S. Krishnan, Norman A. Peppers			
6. REPORT DATE 2 April 1973		7a. TOTAL NO. OF PAGES 159	7b. NO. OF PAGES 24
8a. CONTRACT OR GRANT NO. N00014-70-C-0413		9a. ORIGINATOR'S REPORT NUMBER(S)	
b. PROJECT NO. Modification No. P00007			
c. ERU 8727-100		9b. OTHER REPORT NO(S) (Any other numbers that may be assigned this report)	
d. ISE 2422			
10. DISTRIBUTION STATEMENT Distribution of this document is unlimited.			
11. SUPPLEMENTARY NOTES		12. SPONSORING MILITARY ACTIVITY Defense Advanced Research Projects Agency Order No. 2185 Program Code Nos. 1N10, 2E20	
13. ABSTRACT <p>The concept of a wave-height profilometer based on phase-ranging with a VHF-modulated carbon dioxide (CO₂) laser was examined. Experimental measurements of the diffusely backscattered CO₂ laser radiation from the surface of water were made. Based on these measurements, the conclusion is that a laser profilometer can be assembled mainly from commercially available components. Two designs are recommended: one for use at a range of 3 m for measurements in a wind-wave tank and the other for use at a range of 10 m from a tower in the ocean.</p> <p>The possibility of inferring surface-wave statistics from the properties of the speckle pattern resulting when the surface is illuminated with a laser was investigated. The general theory of speckle patterns was strengthened and extended. The conclusion was that the apparent discrepancies among several theories result from improper interpretation of the results rather than differences in the theories. The ensemble average intensity distribution in the receiver is shown to be related by a Fourier transformation to the ensemble average spatial coherence of the field at the surface. Further, this spatial coherence is related to rms surface roughness and the surface height autocorrelation function when Gaussian statistics can be assumed for the wave-height distribution. The spatial coherence in the receiver is related to the intensity distribution at the surface and contains no information about the surface characteristics. The physical significance of wave height, slope, and curvature power spectral densities and the effect of realistic perturbations are under continued investigation.</p>			

DD FORM 1473 (PAGE 1)

S/N 0101-807-6801

UNCLASSIFIED
Security Classification

14

KEY WORDS

LINK A

LINK B

LINK C

ROLE

WT

ROLE

WT

ROLE

WT

Remote sensing

Capillary waves

Laser profilometer

Phase-ranging radar

Laser speckle

Coherent illumination

Diffuse Backscatter

Temporal coherence

ABSTRACT

The concept of a wave-height profilometer based on phase-ranging with a VHF-modulated carbon dioxide (CO_2) laser was examined. Experimental measurements of the diffusely backscattered CO_2 laser radiation from the surface of water were made. Based on these measurements, the conclusion is that a laser profilometer can be assembled mainly from commercially available components. Two designs are recommended: one for use at a range of 3 m for measurements in a wind-wave tank and the other for use at a range of 10 m from a tower in the ocean.

The possibility of inferring surface-wave statistics from the properties of the speckle pattern resulting when the surface is illuminated with a laser was investigated. The general theory of speckle patterns was strengthened and extended. The conclusion was that the apparent discrepancies among several theories result from improper interpretation of the results rather than differences in the theories. The ensemble average intensity distribution in the receiver is shown to be related by a Fourier transformation to the ensemble average spatial coherence of the field at the surface. Further, this spatial coherence is related to rms surface roughness and the surface height autocorrelation function when Gaussian statistics can be assumed for the wave-height distribution. The spatial coherence in the receiver is related to the intensity distribution at the surface and contains no information about the surface characteristics. The physical significance of wave height, slope, and curvature power spectral densities and the effect of realistic perturbations are under continued investigation.

CONTENTS

DD FORM 1473

ABSTRACT	i
LIST OF ILLUSTRATIONS	v
LIST OF TABLES	vi
FOREWORD	vii
ACKNOWLEDGEMENTS	ix
I INTRODUCTION	1
II LASER PROFILOMETER	3
A. General Considerations	3
B. Experimental Measurements	6
1. Design	8
2. Apparatus	10
3. Calibration	15
4. Results	16
C. Performance Evaluation of the Laser Profilometer	25
1. General	25
2. Laser	25
3. Modulator	26
4. Transmitter and Receiver Optics	28
5. Detector	57
6. Phase Measurement	61
7. Design Logic for the Profilometer System	62
D. Discussion and Recommendations	63

III	THEORY OF SPECKLE PATTERNS	67
A.	Summary of Results	67
B.	General Theory	69
1.	Two Equivalent Forms of the Huygens-Fresnel Principle	69
2.	Ensemble Definitions and Relationships	75
C.	Further Approximations to the General Theory	79
1.	Ensemble Average Intensity and Mutual Intensity	82
2.	Ensemble Average Power Spectral Density for Finite Aperture	88
D.	Spatial Coherence as a Function of Surface Characteristics	96
E.	Comparison of Results with Previous Work	98
1.	The Work of Crane	98
2.	The Early Work of Goodman and Goldfischer	101
F.	Scattering from the Sea	103
1.	General	103
2.	Conditions of Validity	104
3.	Numerical Calculations and Physical Interpretation	106
	REFERENCES	117
	APPENDICES	
A	NOTES ON DISCUSSIONS ON SPECKLE THEORIES	A-1
B	COMPARISON OF VARIOUS THEORIES CONCERNING LASER SPECKLE	B-1
C	THE VALIDITY OF $\overline{I_1 I_2} = \overline{I_1} \overline{I_2} (1 + \lambda ^2)$ FOR SPACE VARYING COMPLEX GAUSSIAN PROCESSES	C-1

ILLUSTRATIONS

1	Block Diagram of Wave Height Measurement System	3
2	Wavelength Dependence of the Skin Depth in Water	5
3	Experimental Setup for Determining Relative Magnitudes of the Specularly and Diffusely Backscattered Components . .	7
4	Geometry of Experimental Measurements	9
5	Definition of Angles in Experiment	11
6	Block Diagram of Experimental Apparatus	12
7	Experimental Arrangement	13
8	Scattering Apparatus	14
9	Angular Dependence of Scattering Parameter of Asbestos ($\beta = 15^\circ$, $\phi = 90^\circ$)	17
10	Angular Dependence of Scattering Parameter of Seawater and Deionized Water ($\beta = 45^\circ$, $\phi = 90^\circ$)	19
11	Angular Dependence of Scattering Parameter of Seawater ($\beta = 45^\circ$, $\phi = 225^\circ$)	20
12	Angular Dependence of Scattering Parameter of Seawater at Two Power Levels ($\beta = 18^\circ$, $\phi = 110^\circ$)	21
13	Non-Linear Power Dependence of Scattering Parameter of Seawater ($\beta = 18^\circ$, $\theta = 45^\circ$, $\phi = 90^\circ$)	23
14	Geometry of the Ranging System	31
15	Receiver Optics	37
16	Dependence of Depth of Field of Receiver on Aperture for Spot Size of 1 mm for 10.6 μm Radiation	40
17	Dependence of Depth of Field of Receiver on Aperture for Spot Size of 2 mm for 10.6 μm Radiation	41
18	Dependence of Depth of Field of Receiver on Aperture for Spot Size of 5 mm for 10.6 μm Radiation	42
19	Dependence of Depth of Field of Receiver on Aperture for Spot Size of 1 mm for 2 μm Radiation	43
20	Dependence of Transmitting Aperture on Size of Beam Waist for Different Ranges or Optical Wavelengths	45

21	Dependence of Gaussian Beam $(1/e^2)$ Radius on Distance from the Beam Waist	46
22	Signal-to-Noise Performance of IR Receiver with Different Power Levels and Detector Sizes	60
23	Summary of Relationships Between Physical Quantities in the Target and Receiver Plane	71
24	Geometry and Coordinate Systems Used in the Huygens-Fresnel Principle	72
25	Assumed Form of the Power Spectral Densities of Natural Wave Height and Perturbation	110
26	Plots of Average Intensity Distribution Showing Effect of Different Strengths of Gaussian Perturbation of Constant Width	113
27	Plots of Average Intensity Distribution Showing Effect of Different Widths of Gaussian Perturbation of Constant Strength	114
B-1	Geometry and Coordinate Systems Used in the Huygens-Fresnel Principle	B-8
B-2	Region of Integration in the (u, u_1) Plane Showing Strips Where Value of $\exp \{ 2\sigma_\beta^2 \rho_w (u-u_1, v-v_1) \}$ Differs from Unity	B-11
B-3	Cross Section of Power Spectral Density for $L \times L$ Square Scattering Spot	B-20
B-4	Normalized Power Spectral Density for Smooth and Rough Surfaces for Which $(L/R) = 10^3$	B-23

TABLES

1	Characteristics of Profilometer Designs for Two Ranges . .	64
B-1	Limiting Forms of the Power Spectral Density for an Illuminated Square Surface $L \times L$ and a Surface Correlation Length R	B-22

FOREWORD

This technical report covers the activity during the period 21 May 1972 through 31 December 1972. The work is expected to be continued with additional funds. The principal investigator, Dr. Kamala S. Krishnan, was responsible for the research activity under SRI Project ERU 8727-100/ISE 2422. The technical direction of the program was provided by Dr. Richard F. Hoglund, Chief, Advanced Concepts Division, Strategic Technology Office, Defense Advanced Research Projects Agency, Arlington, Virginia.

The research program discussed in this report was supported by the Defense Advanced Research Projects Agency of the Department of Defense and was monitored by the Office of Naval Research under Contract No. N00014-70-C-0413.

The views and conclusions contained in this document are those of the authors and should not be interpreted as necessarily reflecting the official policies, either expressed or implied, of the Defense Advanced Research Projects Agency or the U. S. Government.

Reproduction of this report in whole or in part is permitted for any purpose of the U. S. Government.

ACKNOWLEDGMENTS

The authors acknowledge with gratitude the contributions of Dr. Joseph W. Goodman of Stanford University and Dr. Robert B. Crane of Willow Run Laboratories, University of Michigan, Ann Arbor, as consultants during the course of the work. In addition to acting as a consultant, Dr. Goodman has contributed Appendices B and C of this report. The authors are indebted to Drs. Richard C. Honey and Harold C. Guthart of SRI for many valuable suggestions. The discussions with Drs. Richard F. Hoglund of DARPA, Frank Sercik of General Research Corporation, Washington, D. C., and Philip Selwyn of IDA, Washington, D. C. were of considerable value during the program.

I INTRODUCTION

In the study of the surface of the oceans, the capillary wave-height spectrum plays an important role in the coupling of wind energy into the sea, in the turbulent flow and mixing in both the sea and the atmosphere (near the interface), and in the growth of gravity waves on the surface. A possibility also exists for detecting subsurface processes by observing the changes in the natural wave-height spectrum produced as a result of complex and poorly understood interactions between natural and artificial internal waves, the mixed upper layer of the ocean, and the air-sea interface. Ideally, the measurement of ocean surface characteristics should be accomplished remotely without contacting the surface. To be of value in an operational sense, the technique should be capable of data rates consistent with adequate redundancy and effective coverage of the truly vast surface area of the oceans.

The major objective of this program was the analysis of the feasibility of two active laser techniques that have potential for remote sensing. In the laser profilometer technique, a VHF-modulated laser beam is used to irradiate a small area (for spatial resolution) on the surface, and the relative wave amplitude is obtained by phase comparison of the return against the modulating signal. In the speckle approach, a broad area on the surface is illuminated by a laser beam and the surface-wave statistics may be inferred from the properties of the scattered radiation. With both techniques, the use of a CO_2 laser is contemplated because of its small depth of penetration in water. This is crucial to ensure that the radiation is received from the surface and not from the bulk of the water.

This report deals with the two methods in the above order. Laboratory measurements of the diffusely back scattered radiation from the surface of water needed for the evaluation of the profilometer are first described. An analysis and recommendation of a laboratory system for measuring the wave

heights on the surface of water follows. The current status of the theory of speckle patterns pertinent to the measurement of surface characteristics is next described. Application of the theory to scattering from the sea surface is made. Our initial results are then presented.

The work on this program is expected to be continued under another contract. In that sense, this report is an interim status report on the work, although it is intended also to satisfy the requirement for a final report under the current contract.

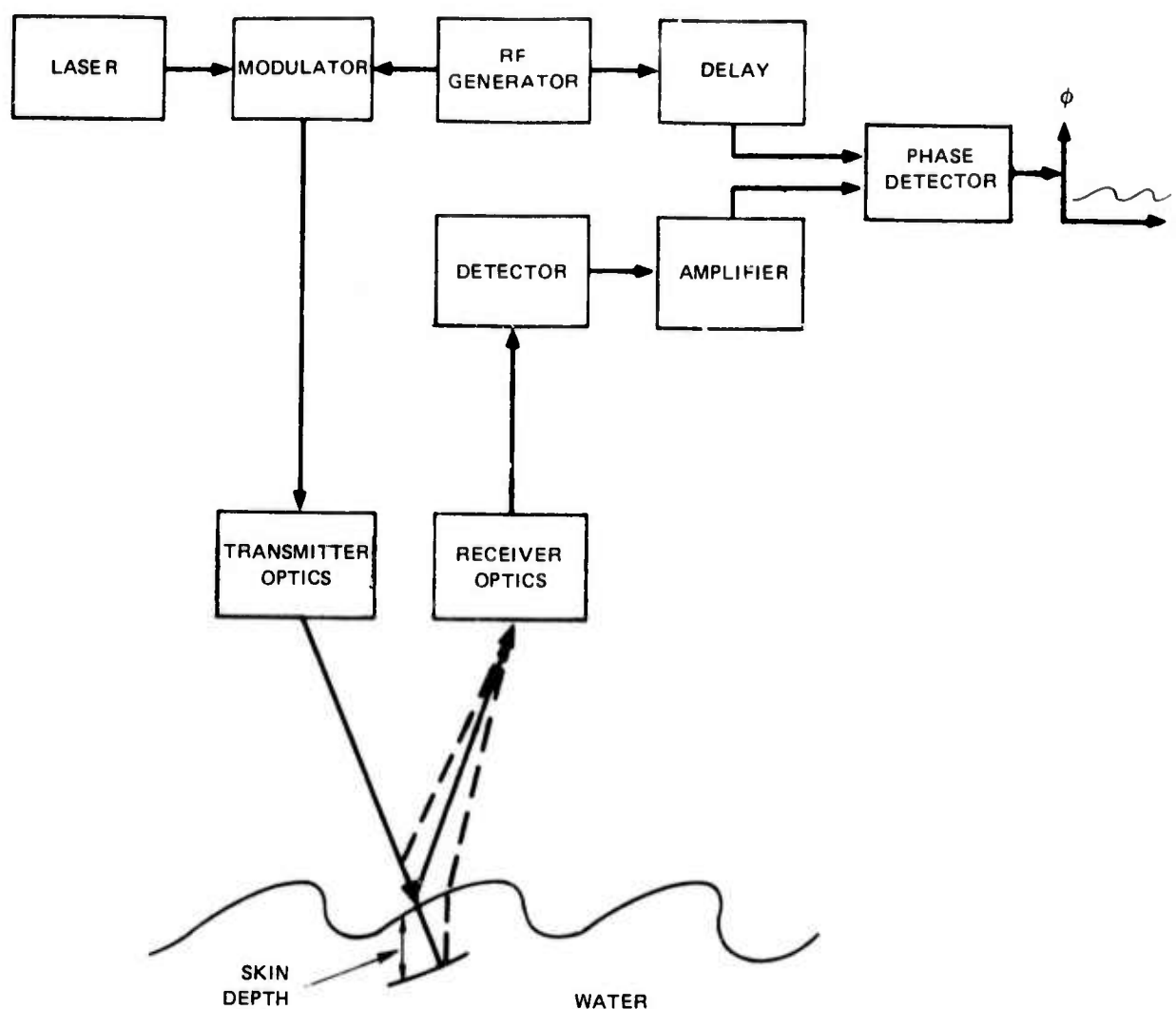
II LASER PROFILOMETER

A. GENERAL CONSIDERATIONS

The technique proposed by SRI uses a VHF-modulated CO_2 laser beam to irradiate an area on the ocean surface that is small compared with the capillary wave structure. The radiation that is scattered back from the ocean surface is collected by suitable optics and detected. The output of the detector as well as a VHF signal representing the modulated output of the laser are now fed into a differential phase-measuring system. A block diagram of the system is shown in Figure 1.

Because the capillary wave structure has dimensions on the order of centimeters, the laser beam must illuminate an area substantially smaller than this in order to resolve details of the capillary wave heights. If the beam illuminates an area large compared with the capillary wave structure, a high probability exists of a specular component being received from some facet of a capillary wave within the illuminated area. This specular component would dominate other diffusely reflected components, and the system would be useful only for monitoring the gravity wave (or large-scale) structure. Thus, to monitor the small-scale structure associated with capillary waves, the vertical and horizontal resolutions have to be on the order of one millimeter.

If an optical beam with a diameter on the order of 1 millimeter is incident on the surface, two components are reflected -- one specular and one diffuse. The specular component will not, in general, be directed back toward the transmitter because the slope of that facet on the surface will not, in general, be normal to the direction of the incident beam. On the assumption that the transmitted beam is focused on the surface, the specularly reflected beam will have a diffraction beamwidth larger than or, at best, equal to that of the interrogating beam; i.e., its beamwidth at the transmitter will be equal to or larger than the transmitting aperture (neglecting atmospheric turbulence).



TA-640583-5R

FIGURE 1 BLOCK DIAGRAM OF WAVE HEIGHT MEASUREMENT SYSTEM

The second component of reflected energy will be diffusely scattered by the bulk of the water or surface imperfections--with an angular distribution in the back hemisphere that is quite broad and well-behaved (at least in the visible portion of the spectrum). This is the component that will, in general, be available to the receiver, and only occasionally will a spike of specularly reflected energy be received. This spike will have not only the proper phase but also a much greater amplitude than the diffusely reflected component.

If the wavelength is in the blue-green region of the spectrum, the beam transmitted through the surface will attenuate slowly with depth--approximately 10 m to the $1/e$ or -4.34 dB point (hereafter referred to as the skin depth) in average surface ocean waters. As a consequence, the center-of-gravity or the phase center of the backscattered light received from this beam could be as much as several m below the surface and could thus lead to a very large error in the apparent height of the sea surface. Even at 642.8 nm (the He-Ne laser), the skin depth can be several m in typical surface ocean waters.^{1,2*}

For this reason, a wavelength must be selected whose depth of penetration in the water is comparable to or less than the vertical resolution desired. A plot of this depth of penetration for infrared wavelengths is shown in Figure 2 (data are calculated from Zolotarev et al.).³

For the system to have reasonable ranges in the atmosphere, it is also essential to select a wavelength in which the atmosphere is reasonably transparent. Reference 4 shows a number of absorption spectra over 300-m atmospheric paths. For narrow-band lasers, higher resolution studies should be consulted to determine whether any narrow atmospheric absorption bands exist at the laser wavelength.

A third factor, the magnitude of the specularly reflected component, is also important. To minimize the amplitude of the occasional specularly reflected spike that the receiver must handle, this reflection should be as small as possible. Reference 2 (pp. 362-363) tabulates this reflection coefficient as a function of wavelength.

After consideration of all factors, as well as the laser state of the art, it was decided that a CO_2 laser ($\lambda = 10.6 \mu\text{m}$) has the following desirable features for this application:

- Available in well-engineered, reliable packages with good power outputs at high efficiency.
- High atmospheric transmission in the absence of water droplets or fog.
- Specular reflection coefficient of less than 1 percent.
- Skin depth in water of about $10 \mu\text{m}$.

*References are listed at the end of this report.

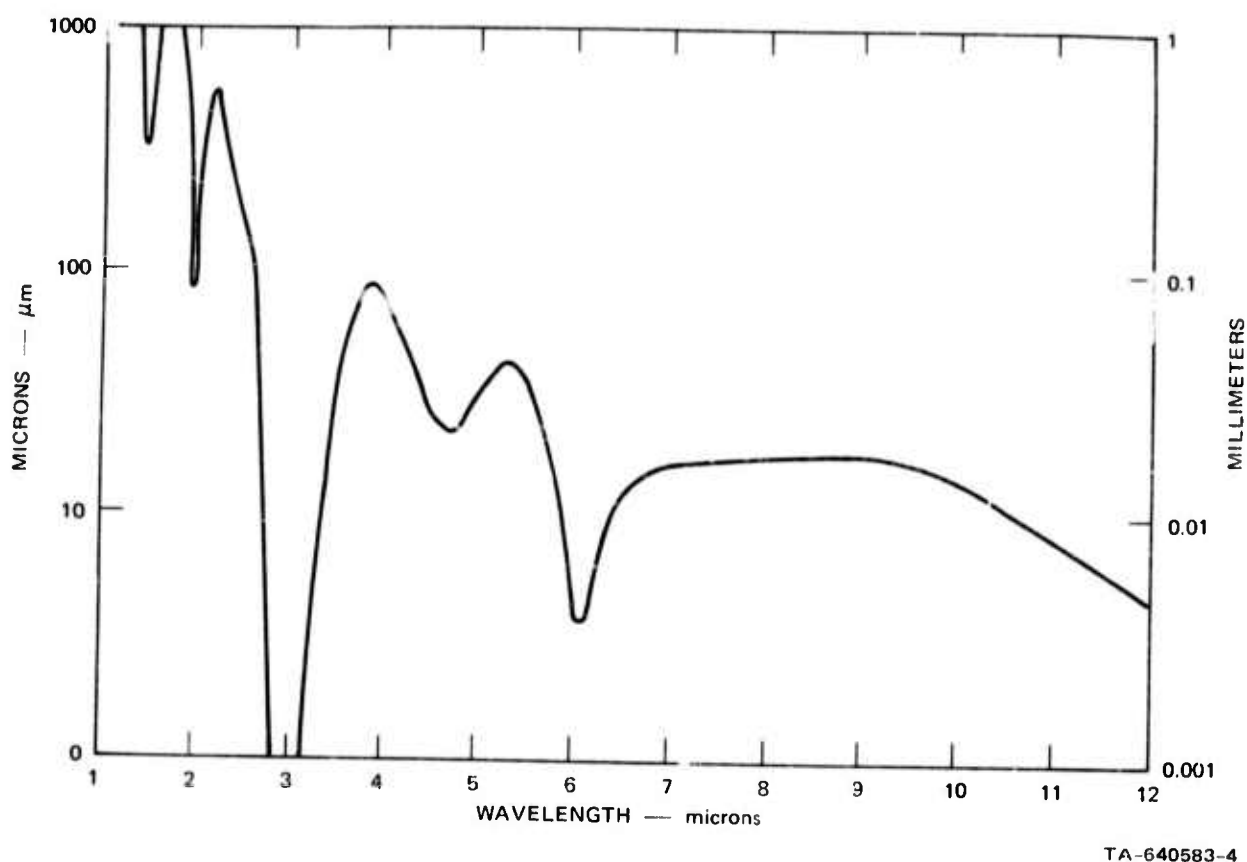


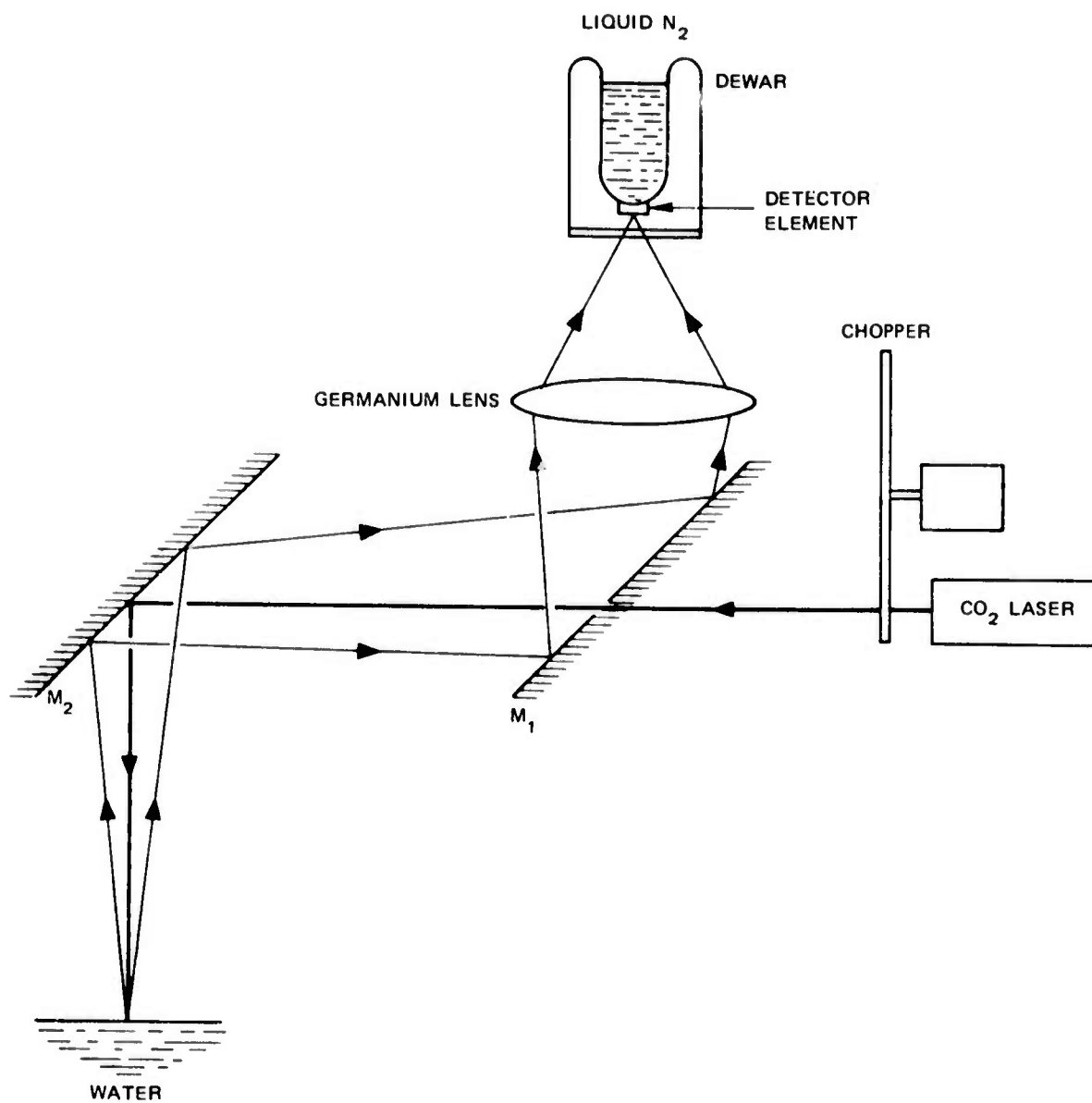
FIGURE 2 WAVELENGTH DEPENDENCE OF THE SKIN DEPTH IN WATER

Source: Zolotarev, V.M., et al., Optics and Spectroscopy, 27,

B. EXPERIMENTAL MEASUREMENTS

Before SRI submitted the proposal to perform work on a phase-ranging radar based on a CO_2 laser, preliminary and limited experiments were performed to measure the relative magnitudes of the specularly and diffusely backscattered components.

The experimental setup is shown in Figure 3. A CO_2 laser with a power output on the order of 1 W is chopped at 900 c/s. The chopped beam passes through a hole in a mirror, M_1 , and is reflected down onto the surface of a pan of water by another mirror, M_2 . The mirrors act as collectors for the radiation from the surface of the water, which is focused onto a liquid-nitrogen-cooled photoconductive (gold-doped germanium) detector.



TA-640583-6R

FIGURE 3 EXPERIMENTAL SET UP FOR DETERMINING RELATIVE MAGNITUDES OF THE SPECULARLY AND DIFFUSELY BACKSCATTERED COMPONENTS

During these experiments, the signal from the backscattered component was found to be 3 to 4 orders of magnitude smaller than that from the specular component, but it was well within the dynamic range constraints of the proposed phase detector and well above the sensitivity of the proposed optical detector. It should be kept in mind that the signal received from the scattered component depends on the size of the receiving aperture, but the specular component does not. Further, it was found that focusing the laser beam onto the surface of the water created a dimple. The effect of this dimple is to enhance the backscatter signal strength by creating, in effect, a specular component in the backscattered radiation.

However, during these preliminary experiments, geometrical limitations restricted the range of angles over which the measurements could be performed. A larger range is to be encountered in the sea-slope spectrum. Further, the detector used in these experiments was not the optimum detector for $10.6 \mu\text{m}$ radiation. For these reasons, we felt that before a feasibility analysis and a firm recommendation concerning the construction of a demonstration profilometer could be made, more reliable and complete data were required. Therefore, we designed and executed an experiment to obtain these data. The following subsections describe the design of the experiment, the apparatus used, the calibration procedure, and the results.

1. Design

In order not to constrain the profilometer design for lack of information on the angular distribution of the diffusely scattered radiation, it was decided that data should be taken over a range of incidence angles and over a range of azimuth and elevation angles of the receiver. Although the number of data points to be taken would be determined by the extent to which structure was manifested in the results, provision was made in the design of the apparatus to permit data to be taken over a full hemisphere, thus taking advantage of the inherent symmetry of the geometry to cover a small range where the physical obstructions were unavoidable. However, because of the finite acceptance angle

of the detector, a small zone of the hemisphere near the horizontal plane cannot be treated in a manner equivalent to the rest of the sphere.

Figure 4 shows the basic geometry of the experiment. A Gaussian beam from a CO₂ laser is incident on the surface of the water, and the radiation that is scattered into a solid angle Ω_0 , not in the specular direction, is collected by an optical system that forms an image of the incident spot on the detector element. The optical system is designed such that this image is always smaller than the detector element for all angles used.

We define a scattering parameter $\sigma(\beta, \theta, \varphi)$ by

$$\sigma(\beta, \theta, \varphi) \triangleq \frac{\Delta P(\beta, \theta, \varphi)}{P_i \Omega_c} = \frac{R(\beta, \theta, \varphi)}{\Omega_0} \quad (2.1)$$

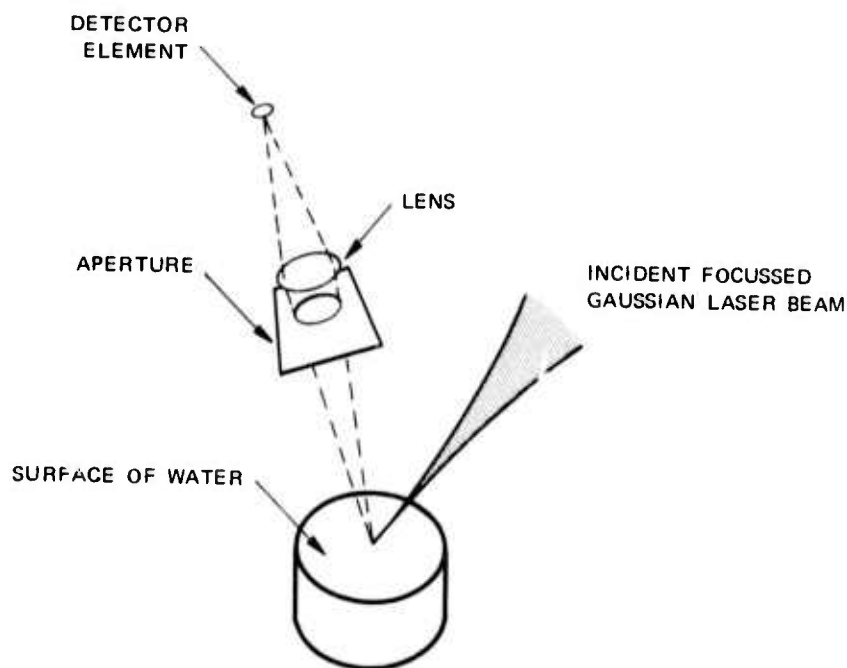


FIGURE 4 GEOMETRY OF EXPERIMENTAL MEASUREMENTS

where ΔP is the amount of power scattered into solid angle Ω_0 , P_i is the incident power, and $R(\beta, \theta, \varphi)$ is defined by

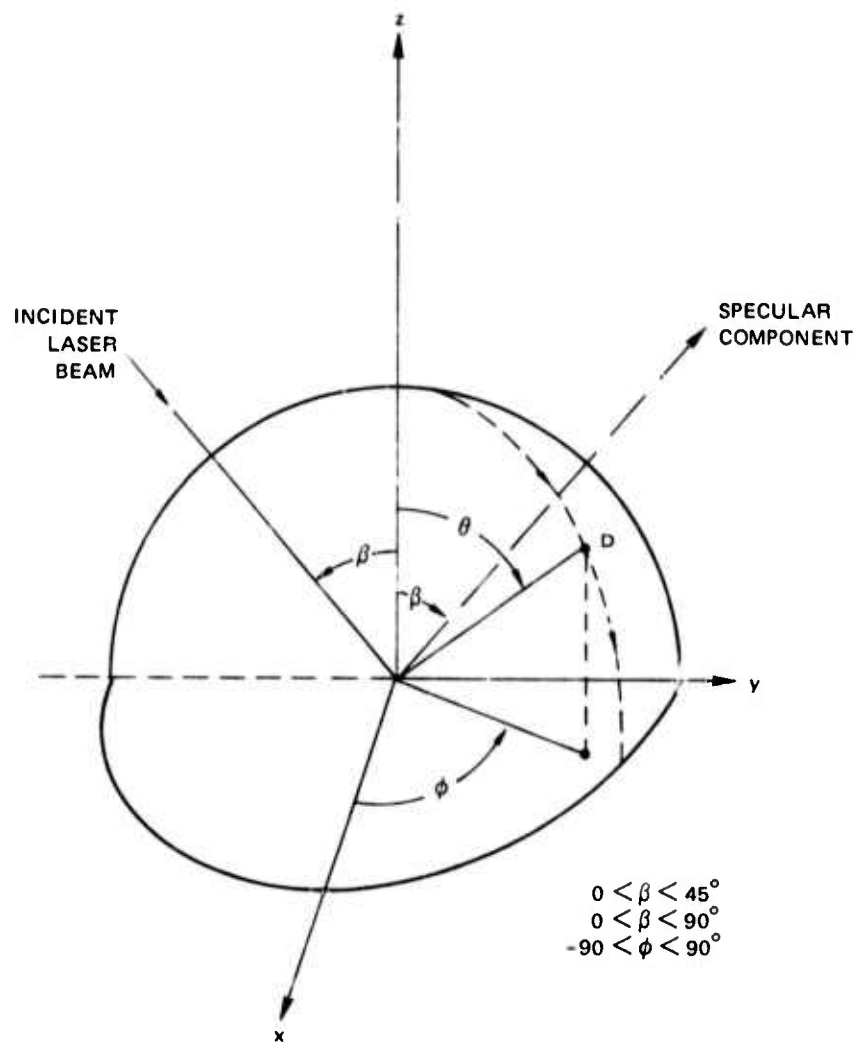
$$R(\beta, \theta, \varphi) \triangleq \frac{\Delta P(\beta, \theta, \varphi)}{P_i}. \quad (2.2)$$

Figure 5 defines the angles β, θ, φ . Thus, experimentally, we measure ΔP , P_i , and Ω_0 so that scattering phenomenon can be completely characterized by Eq. (2.1).

2. Apparatus

A block diagram of the experimental apparatus is shown in Figure 6. The experimental arrangement is shown in Figure 7. An He-Ne laser is used for alignment purposes; and a mirror that can be flipped in and out of position, is adjusted before the experiment such that the laser's visible beam is accurately coaxial with the CO_2 laser beam. Another He-Ne laser, called the reference laser, is used to provide a reference signal for phase-sensitive detection. During the experiment, the beam from this laser crosses the CO_2 laser beam at the point where it is chopped and is incident on detector D_r that provides a reference signal to the phase-sensitive detector. Thus, both the incident CO_2 laser beam and the reference He-Ne laser beam are square-wave modulated at 150 Hz. The ΔP signal from the scattering apparatus is measured by the phase-sensitive detector and is then sent to the Y channel of an X-Y recorder. A signal from the scattering apparatus that is proportional to the angle θ feeds the X channel of this recorder. The phase-sensitive detector was used with an integration time of 3 s and a roll-off of 12 dB per octave. A CR Model 201 power meter inserted in the beam before and after data were taken was used to monitor the CO_2 laser power.

A photograph of the scattering apparatus is shown in Figure 8. The CO_2 laser beam is reflected by mirror M_1 to mirror M_2 that focuses it onto the surface of the water contained in plastic cup C located on the center of the rotating table T. Detector D is a Laser Precision Corporation pyroelectric detector (Model number Kt-4110 with Kth-111 preamplifier and with a load resistor $R = 10\text{M}\Omega$) located on a motor driven arm that can be moved on the circumference of a circle whose center is the point of intersection of the CO_2 laser beam and the water surface adjusted to a prescribed level. The collecting optics



SA-2422-2

FIGURE 5 DEFINITION OF ANGLES IN EXPERIMENT

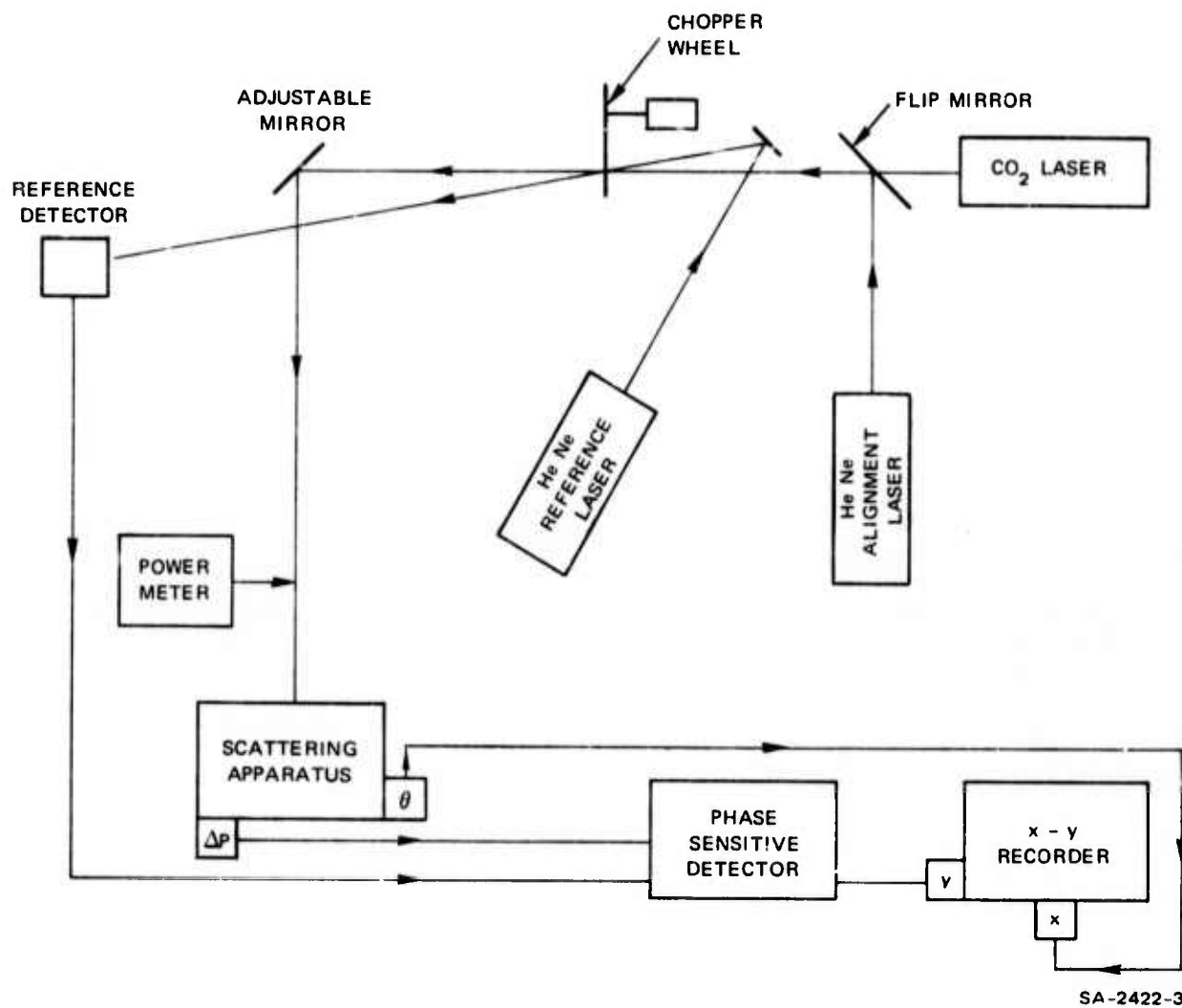


FIGURE 6 BLOCK DIAGRAM OF EXPERIMENTAL APPARATUS

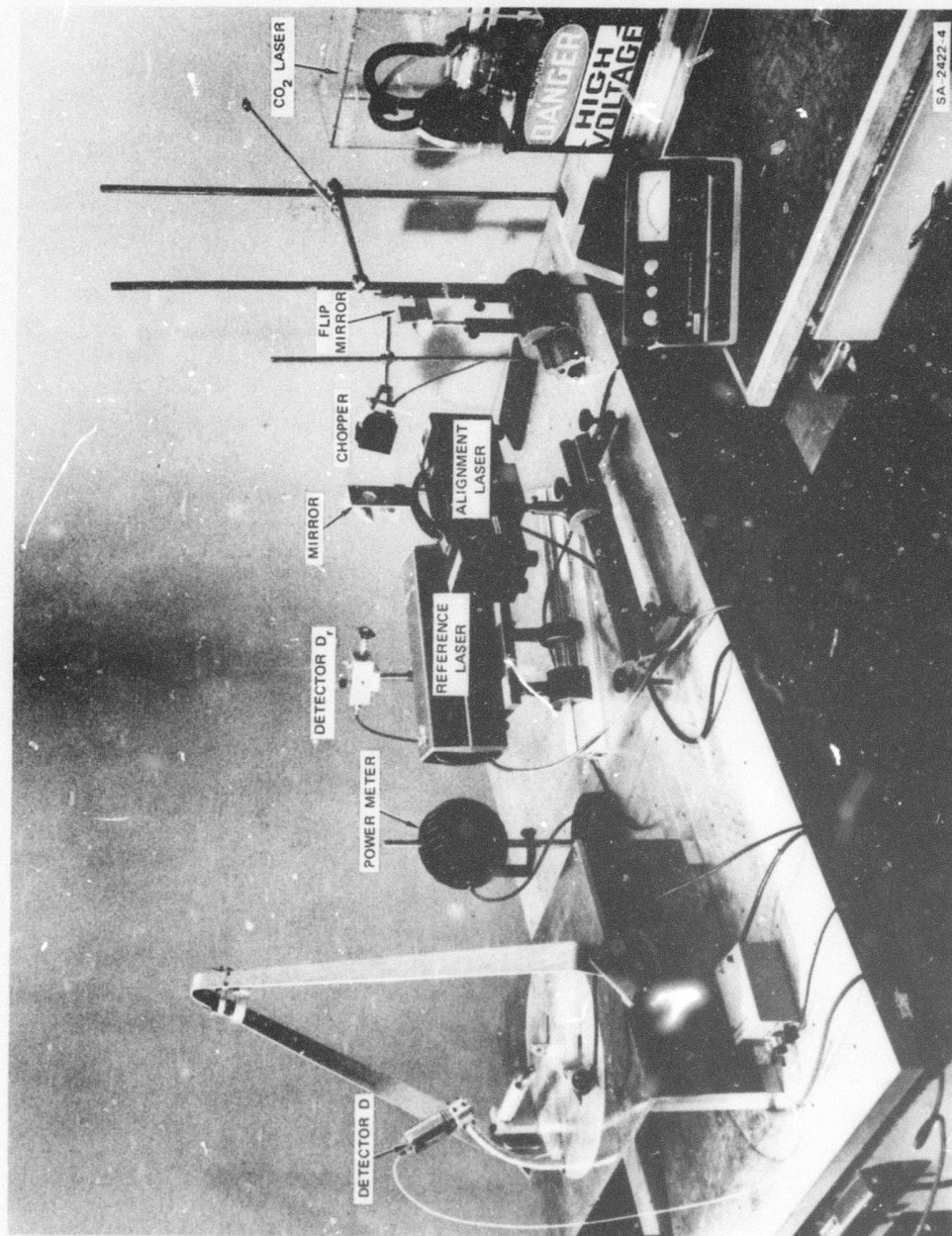


FIGURE 7 EXPERIMENTAL ARRANGEMENT

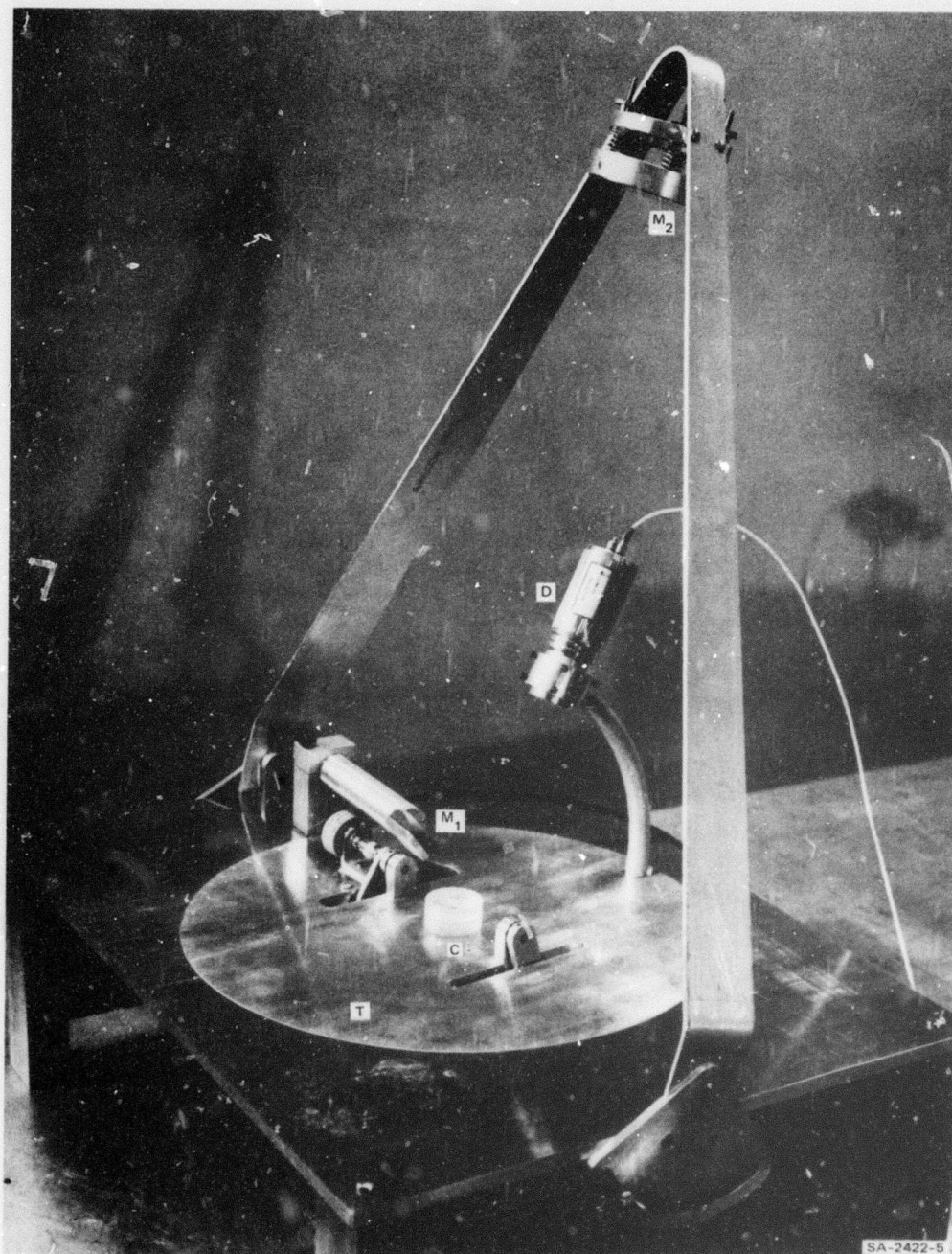


FIGURE 8 SCATTERING APPARATUS

for this detector consist of two diffraction-limited antireflection-coated IRTRAN II lenses. The outer lens has a focal length of 6 in and is located 6 in from the water surface; the inner lens has a focal length of 1 in and is located 1 in from the detector element. The aperture of this optical system subtends a solid angle Ω_0 of about 0.022 sr at the water surface. The spot size of the laser beam at the surface of the water is calculated to be 0.27 mm. The size of a speckle at the lens aperture is given by $(R\lambda/D) = 0.58$ cm and on the average about 18 speckles will be in the one-inch aperture at a given instant. The signal-to-noise ratio resulting from deviations from this average value is about 4. However, if the integration time is on the order of a few seconds as was the case during the experiments, the speckles change many times and the fluctuations in the number of speckles become very small. The experimental signal-to-noise ratio during these measurements was estimated to be about 20 when the diffusely scattered component was measured.

3. Calibration

The calibration of the apparatus was achieved in steps because of the limited dynamic range of the detection system. The CO_2 laser beam was first attenuated by a calibrated salt crystal attenuator and was then incident on a good quality specular gold mirror that was positioned in the scattering apparatus in place of the water surface. The optical collection system was placed in the specular direction so that it collected all of the specular radiation from the gold mirror. The transfer function for the entire apparatus was then calculated from the signal measured by the phase-sensitive detector, the measured CO_2 laser power, and the known attenuation of the calibrated salt crystal attenuator. The transfer function, measured in this way, accounts for all optical, electrooptical, and electronic attenuation or gain in the system.

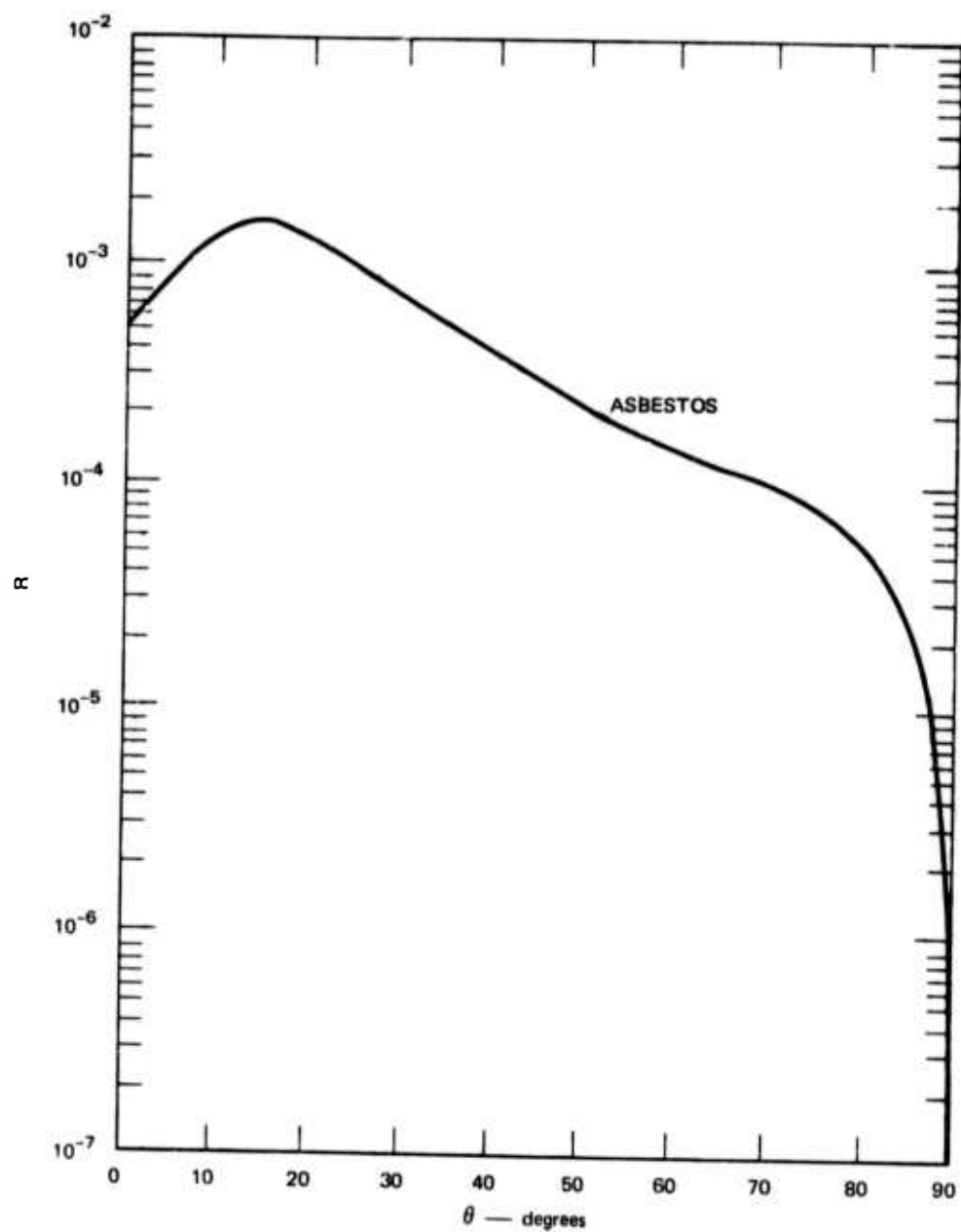
The salt crystal attenuator consisted of two polished NaCl flats oriented such that the unpolarized incident CO_2 laser beam was reflected twice at 45° . The component of the electric field that was Fresnel reflected in the perpendicular (\perp) sense on the first reflection was Fresnel reflected in the parallel (\parallel) sense

on the second reflection and vice versa. The power in the resulting unpolarized beam was then calculated from the known index of refraction of NaCl at $10.6 \mu\text{m}$. The attenuation was calculated to be 7.3×10^{-4} .

4. Results

Before measurements on seawater were actually made, several short experiments were made to determine the dynamic range, accuracy, and sensitivity of the apparatus. After the CO_2 laser beam was attenuated, the specular reflectance of distilled water was measured for $\beta = 15^\circ$ and $\beta = 45^\circ$, and it was found to agree closely with the calculated values when the known index of refraction for water at $10.6 \mu\text{m}$ was used. By measuring away from the specular direction, we found that we could easily distinguish between a good quality, clean, first surface mirror and a poorly polished or dusty mirror. This emphasized the importance of clean optics in the experiment and led us to carefully clean all the optics in the apparatus and to maintain them free from dust. In spite of this, it was found that significant percentage errors could result from specific geometric configurations of the measuring apparatus which involved shiny metallic surfaces in the field of view of the collecting optics. After using a series of baffles, tubes, and absorbing diffuse scattering material on metallic surfaces, we were satisfied that the measured signal was coming only from the illuminated spot on the water surface.

To demonstrate the dynamic range capability, we measured the diffuse scattering from a planar sheet of asbestos at several azimuthal angles. In Figure 9, one such measurement shows the scattering parameter $R(15^\circ, \theta, 90^\circ)$ as a function of elevation angle θ in the plane of incidence. It is worth noting that because the collecting optics subtended an angle of about 10° , part of the reason for the rapid falloff of signal beyond $\theta = 80^\circ$ is the obscuration of this aperture as part of the aperture goes below the horizontal plane of the asbestos. For this reason, measurements beyond $\theta = 80^\circ$ should be discounted.



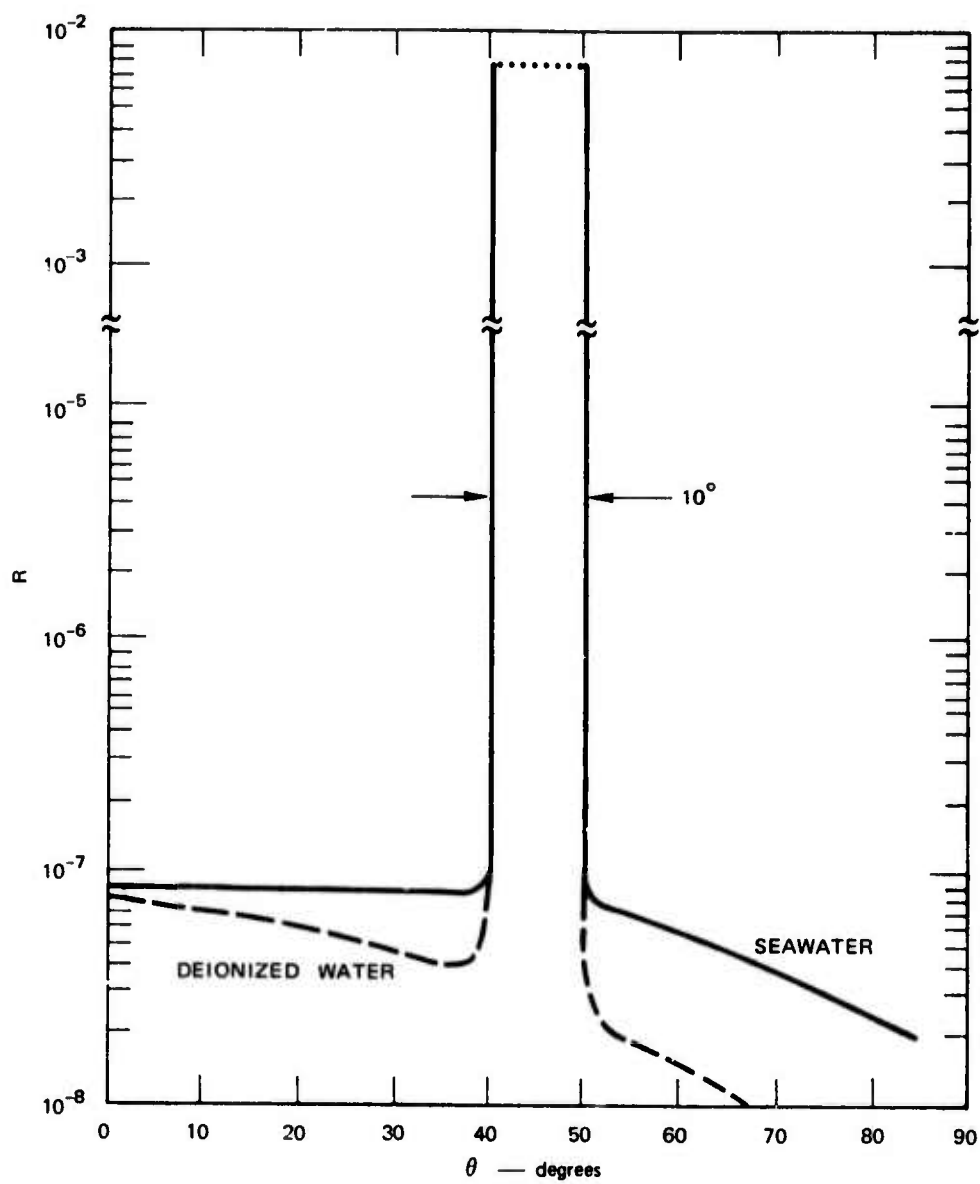
SA-2422-6

FIGURE 9 ANGULAR DEPENDENCE OF SCATTERING PARAMETER OF ASBESTOS
($\beta = 15^\circ$, $\phi = 90^\circ$)

Our results for water measurements are shown in Figure 10. For a reference, we chose 20 M Ω deionized water that was available from our clean room facility. Scattering from this water is indicated by the dashed curve in Figure 10. Also plotted in Figure 10 is a curve labeled seawater. This water was taken from San Francisco Bay, and, although care was taken to collect clean water free from sediment, the water was not filtered or processed in any other way after the sample was taken. The large flat-topped signal indicated between 40° and 50° would be the result of scanning through the Fresnel reflection located in the plane of incidence at 45°. However, because of the allowable power densities at the detector, it could not be scanned through the specular reflection without attenuating the laser beam. Thus, the value depicted is that calculated for deionized water and it is in agreement with a different experiment as described earlier. The discontinuity of one order of magnitude indicated on the R axis should be noted. The width of this pedestal is about 10° corresponding to the angle subtended by the collecting optics. It is clear from Figure 10 that a measurable difference exists between seawater and our reference deionized water, particularly at large angles.

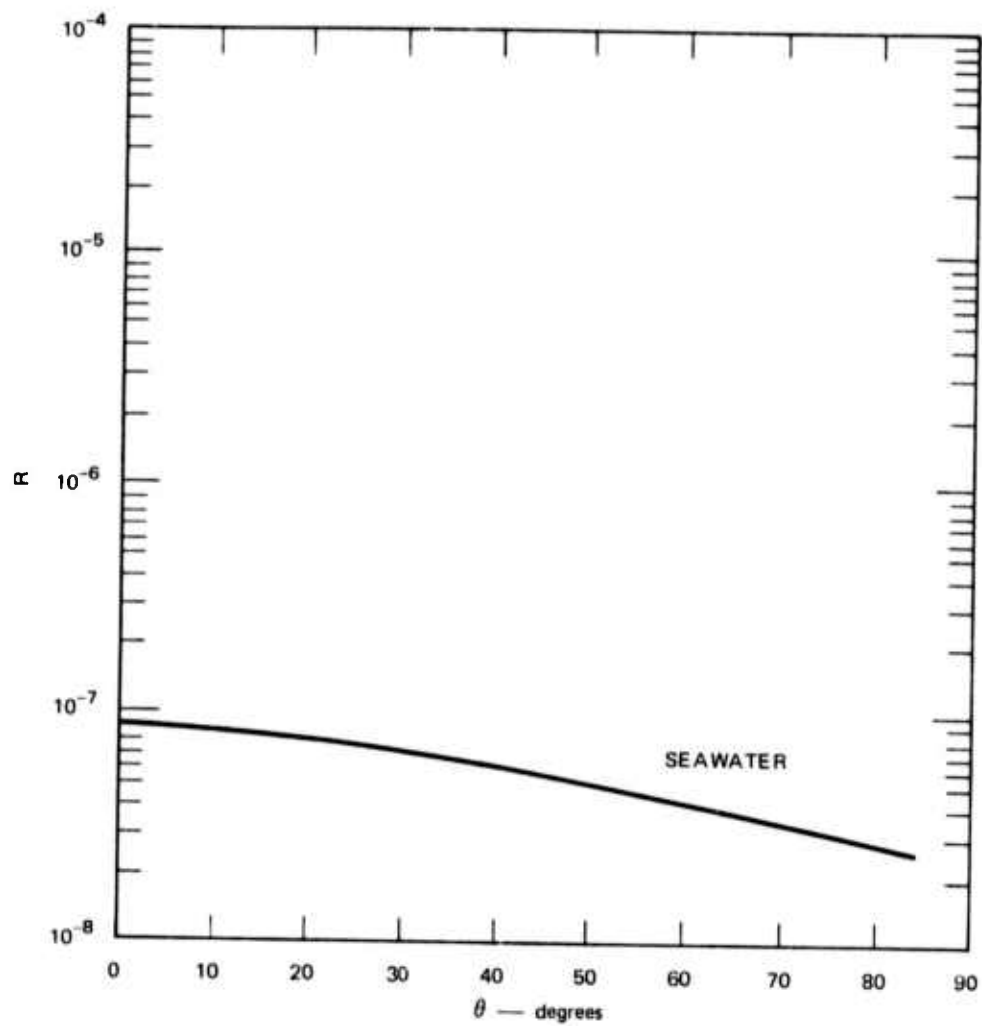
We also measured the scattering parameter for $\beta = 45^\circ$ for five other azimuthal angles distributed between $\varphi = 90^\circ$ and $\varphi = 260^\circ$. The result for $\varphi = 225^\circ$ is shown in Figure 11. Other results are not shown because no structure in R was observed, and the results are essentially identical to Figure 11.

The scattering parameter was also measured for $\beta = 18^\circ$. During the course of this measurement, we observed an effect that was strongly nonlinear in power. Changing the angle of incidence from 45° to 18° at the same power sufficiently increased the power density at the surface of the seawater such that a residue began to form when the laser beam was turned on, and the amount of scattered radiation increased markedly. Figure 12 shows the result for $\beta = 18^\circ$, $\varphi = 110^\circ$ at two different incident powers. These and similar results at other angles φ are somewhat less reliable than our results for higher values of β for two reasons. First, the residue that was formed at higher powers moved



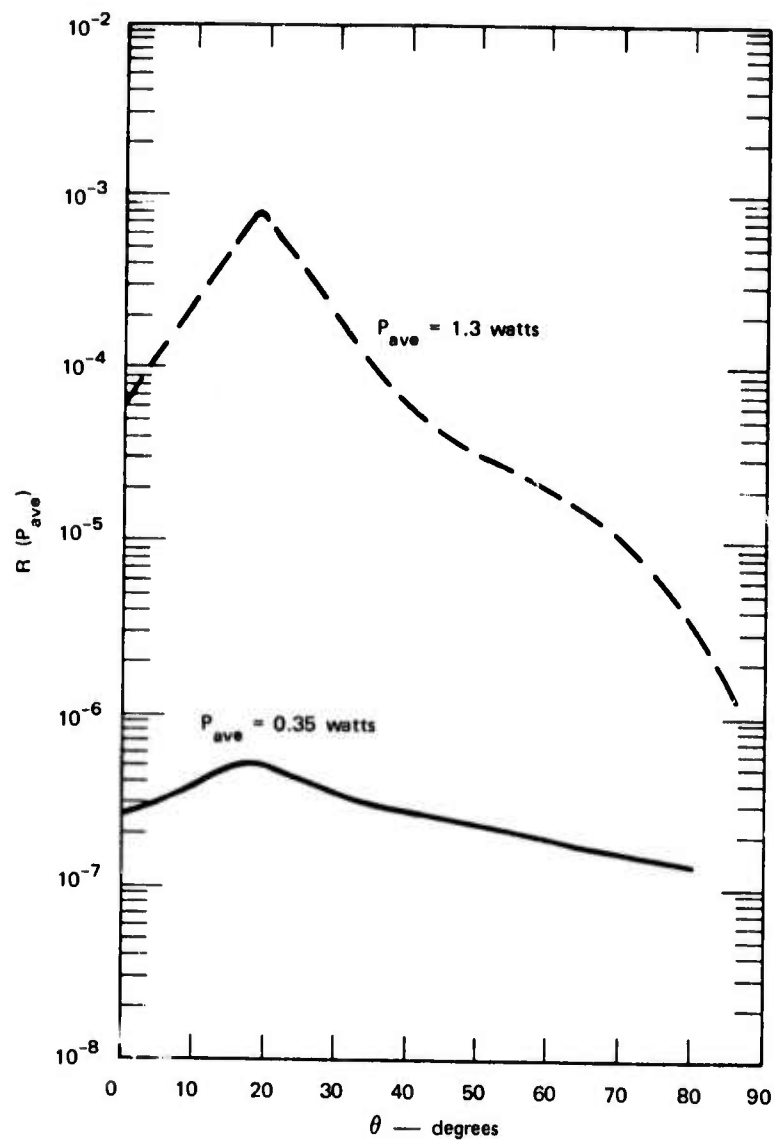
SA-2422-7

FIGURE 10 ANGULAR DEPENDENCE OF SCATTERING PARAMETER OF SEAWATER AND DEIONIZED WATER
 $(\beta = 45^\circ, \phi = 90^\circ)$



SA-2422-8

FIGURE 11 ANGULAR DEPENDENCE OF SCATTERING PARAMETER OF SEAWATER
 $(\beta = 45^\circ, \phi = 225^\circ)$



SA-2422-9

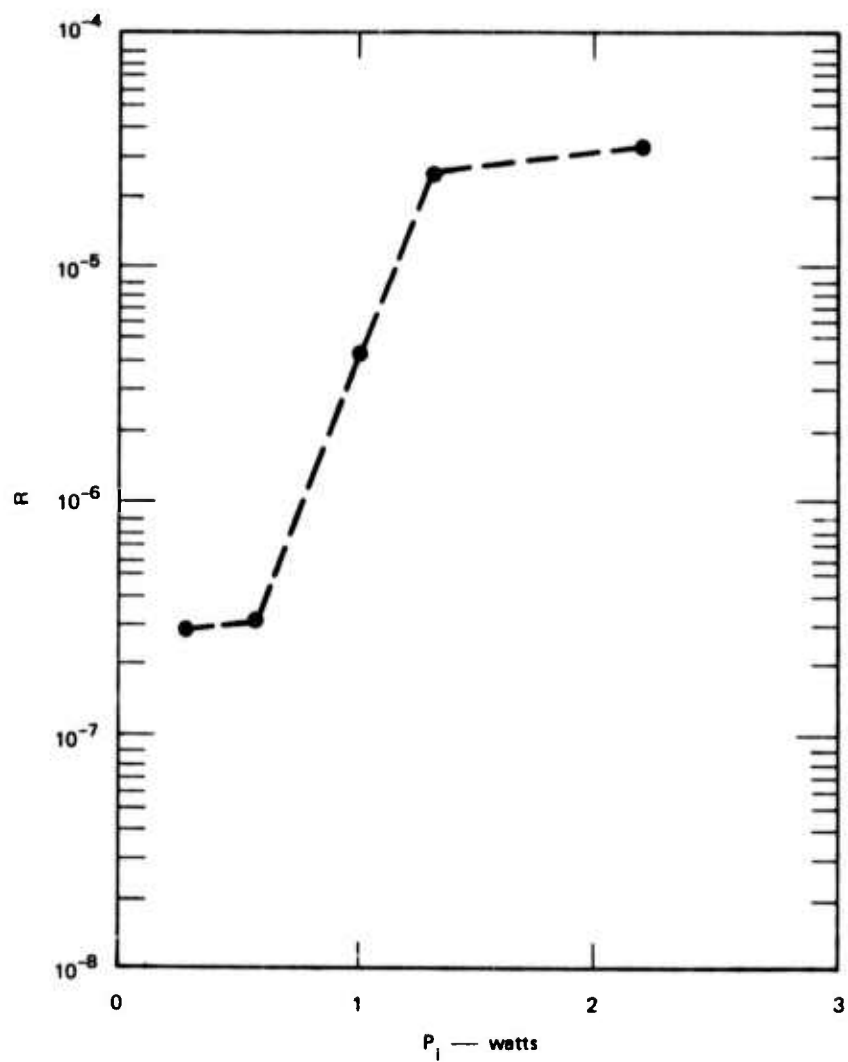
FIGURE 12 ANGULAR DEPENDENCE OF SCATTERING PARAMETER
OF SEAWATER AT TWO POWER LEVELS
($\beta = 18^\circ$, $\phi = 110^\circ$)

rather randomly on the surface because of the convection currents so that the measured signal fluctuated as a function of time. Second, when the power was reduced to ensure that no residue would be formed, the signal-to-noise ratio for the experiment dropped.

A brief investigation of the formation of the residue was made because a considerable enhancement of the scattered signal occurs after its formation, and it was thus of interest to see whether it could be reliably produced. Water from the San Francisco Bay and the Pacific Ocean, as well as tap water, distilled water, and artificial seawater were used. As the power density was increased to about 100 W cm^{-2} , a dimple was formed in all cases at the water surface at the focus of the laser beam. (For the experimental beam diam of about 0.27 mm, the averaged power density is about $1.7 \times 10^3 P_i \text{ W cm}^{-2}$.) The fractional scattered power is essentially independent of incident power at these levels. One could also observe the convection currents and at times a plume of steam generated by the local heating from the beam. The residue can be observed to form at about 1 kW cm^{-2} with an accompanying large increase in fractional scattered power. There appears to be a rather sharp power density threshold for this effect after which the fractional scattered power again becomes rather independent of power. This power dependence of R (18° , 45° , 90°) exhibits a sharp increase at about 1 kW cm^{-2} as shown in Figure 13.

The residue visibly formed only with San Francisco Bay water. Its formation was accompanied by audible violent ebullition or spitting, and the residue moved along with the convection currents. The scattering signal also fluctuated rather rapidly with time. Based on the assumption that this fluctuation was caused by the formed residue moving off the beam and a new bit of residue forming at the beam focus, the time constant for the formation of the residue was found to be on the order 40 ms.

No residue was observed to form on the other types of water even though violent spitting was audible in these cases at various power levels. Another interesting observation was that the violent action seemed to be triggered by surfactants. For example, if care was taken and a fresh sample of the water was



SA-2422-10

FIGURE 13 NON-LINEAR POWER DEPENDENCE OF SCATTERING
PARAMETER OF SEAWATER
($\beta = 18^\circ$, $\theta = 45^\circ$, $\phi = 90^\circ$)

placed in the cup without actually touching the cup or water, only the dimple and convection currents would be observed at a fairly high power level. However, when the water was touched with a finger or with a paper towel twisted (by hand), into a point, the violent spitting would immediately start.

The residue is surmised to be salt. However, only in the case of the Bay water, the scum or residue formed in a large enough quantity to allow collection on a slide. It is quite possible, of course, that small amounts of the residue formed with ocean water and artificial seawater; however, they did not agglomerate into a visible scum.

A preliminary analysis with a laser microprobe was inconclusive as to elemental composition. Thus, the nature or the mechanism of formation of the residue is not currently identified. Its potential for surfactant detection and enhancement of the scattered signal should be noted.

Thus, the scattering parameter R , Eq. (2.2), was found to have a value of 10^{-7} for the experimental geometry. This value was found to be relatively independent of the various angles β , θ , and φ in the ranges in which we were able to examine them. No evidence was found to indicate any peculiar features. Since the experimental system had a collection aperture of 0.0218 sr, the above value of R , leads to a value

$$\sigma_{\text{diffuse}} = \frac{R}{\Delta\Omega_0} = 4.58 \times 10^{-6} \text{ sr}^{-1} .$$

For purposes of comparison, the expected molecular scattering from the molecules in a layer of water 10 μm deep at the focal region of 0.27 mm diam was calculated using a similar geometry and assuming a molecular scattering cross section of $10^{-32} \text{ cm}^2 \text{ sr}^{-1} \text{ molecule}^{-1}$ at 10.6 μm . It was found that

$$\sigma_{\text{molecular}} \cong 4 \times 10^{-13} \text{ sr}^{-1} .$$

The detection system used would be inadequate to the task of seeing this signal. The observed diffuse scattering appears to result from phenomena other than molecular scattering; in all probability, particulate scattering.

C. PERFORMANCE EVALUATION OF THE LASER PROFILOMETER

1. General

The general concept of the profilometer is as follows: The laser beam will be amplitude-modulated (external to the laser cavity) at a chosen frequency and directed at the surface of the water by suitable optics. A receiver will collect and focus the backscatter radiation onto a detector after it passes through a cooled narrowband filter to reject unwanted background thermal radiation. The output of the detector will be amplified with low-noise, narrow-band amplifiers. The amplified output of the detector and a sample of the modulating voltage will be fed into a commercially available phase-measuring instrument that has a voltage output proportional to the phase difference between the two input signals. This voltage, which is related to the target range, can then be tape recorded and analyzed subsequently. In this scheme, the absolute distance to the target is not measurable; instead, only the changes in the distance to the target are measurable.

The proposed system is to be assembled from commercially available components with a minimum of development. In the following subsections, the various components of the system are examined to determine the requirements placed on them and to compare them with the state of the art. The factors limiting the performance of the system are detailed. The characteristics expected from two different designs are presented, and recommendations for their application are made.

2. The Laser

The choice of the CO₂ laser was based on reasons outlined earlier in this section. Briefly, the reasons were: (1) the small skin depth of 10.6 μm radiation

in water, (2) the high transmittance of the atmosphere at $10.6\text{ }\mu\text{m}$, (3) the high degree of development and reliability of commercially available CO_2 lasers, (4) the high power levels available in the CO_2 laser, and (5) the availability of fast and sensitive detectors and modulators at this wavelength. However, as will be seen later, the relatively long wavelength limits the useful range of the system; but shorter wavelength lasers of acceptably small skin depths, (say $\lambda = 2\text{--}5\text{ }\mu\text{m}$), adequate power, and reliability are still under active development.

To obtain the highest resolution feasible, the laser should operate single mode at TEM_{00} . Polarized output is needed for the operation of the external modulator. The amplitude stability of the laser will not be a factor in the system design as long as the frequency of these amplitude variations is well below the modulating frequency. For example, a 10-KHz variation would not degrade performance at a modulating frequency of 100 MHz. The wavelength stability is again not critical because over the emission range of a CO_2 laser, all the other components of the system and the atmosphere are expected to be nearly identical in behavior.

3. Modulator

Amplitude modulation of laser beams is accomplished with crystals in which birefringence may be induced by the application of an electric field. This birefringence changes the state of polarization of a polarized light beam on passing through the crystal. The emerging beam will be passed or attenuated by a fixed polarizing element placed in the beam, depending on the relative orientations of the original polarization of the beam and the polarizer. Thus, a VHF voltage is applied to the crystal, the output of the polarizer will be an amplitude-modulated polarized beam.

Electrooptic modulators based on these principles have been operated successfully at frequencies as high as 3 GHz at visible wavelengths, however, several practical difficulties arise in producing and efficiently coupling to the crystal the rather high voltages required, especially when a wide bandwidth is needed⁵. The modulation may be accomplished by positioning the crystal either

inside or outside the cavity. In the current case, external modulation is to be preferred because the reliability and performance of a commercial CO₂ laser package may be degraded by introducing other intracavity elements.

For operation in the 1-15 μm range and in particular at 10.6 μm , GaAs and CdTe are the available electrooptic materials with the necessary intrinsic frequency response^{6,7}. It will be seen later that in the current application, the modulator needs to operate at a single frequency in the neighborhood of 100 MHz with almost no bandwidth at all. A GaAs modulator that is capable of operation up to 3 MHz,⁶ is available commercially and operation at higher frequencies is possible with modification. A quotation of \$5500 for the modulator and \$3300 for a modified power supply capable of driving the modulator at 100 MHz was obtained in September 1971; more recently (December 1972), the prices quoted were \$5500 and \$7800 respectively. Such a turn of events makes the development of CdTe modulators a possible alternative because good quality CdTe crystals have become commercially available⁷. Considerable amount of work has already been done in the development of CdTe modulators.⁸ Furthermore, CdTe is claimed to have more attractive properties for modulator application. The half-wave voltage for CdTe is half that for GaAs and the absorption of CdTe is 2-10 times smaller than that of the best values reported for GaAs.⁹ The development of a power supply capable of producing the high voltages at the desired high frequencies is not a trivial problem, but it is manageable. Modulator technology is rapidly changing and must be reevaluated at the time the assembly of the system is begun.

The long-term stability of the modulating voltage (the amplitude and frequency are related to the modulation index and frequency of the modulated laser beam) is unimportant as long as it is within the bandwidth of the modulator package and if the modulating signal itself is used as the reference signal. The bandwidth of the modulator package must be smaller than the bandwidth of the receiver amplifiers. The short-term stability of the modulating voltage (just as the short-term amplitude stability of the laser) is determined by the measurement time of the phase-measuring system since drift in amplitude and frequency will be interpreted as phase changes. However, for short ranges or with suitable delays built into the reference signal, this effect will be unimportant. The depth

of modulation or modulation index is a consideration in the determination of receiver noise.

5. Transmitter and Receiver Optics

The function of the transmitting optics is to direct the laser beam onto the surface of the water. The receiving optics serve to image the laser-illuminated area on the water surface onto a detector. It is intuitively evident that the size of either the illuminated area or the image of the detector on the surface of the water, whichever is smaller, determines the horizontal resolution of the system. It can also be related to the vertical resolution. The size of the spot that can be illuminated by the transmitter is in the first instance limited by diffraction to a diameter on the order of a wavelength of the optical radiation. However, in practice, such tight focussing is not possible for realistic ranges and aperture sizes. Further, it is also undesirable because the tighter the focussing, the larger the divergence (or the rapidity with which the beam area enlarges with distance away from the focus) and the result is a smaller depth of focus (or the distance over which the beam stays confined to a small area). In the current application, with waves of changing height as the target, clearly the optimum as well as the practicable system requires a compromise between small spot size and adequate depth of focus. Similar considerations apply to receiver design also.

The size of the illuminated area on the surface with respect to the size of the facets of the capillary waves on the surface determines the probabilities of receiving a specular return from the surface as well as reflections (glints) from the sun (in daytime outdoor operation). These probabilities are also related to the depression angle of the illuminating beam, given the slope distributions to be found in the ocean.

Monostatic or bistatic placement of the transmitter and receiver are a further consideration in the design of the optical system. In a bistatic arrangement,

to ensure that the radiation from the illuminated spot falls on the detector when the waves are shifting the surface, it will be necessary either to track the spot with the receiver or to use a detector with a large area. Tracking adds to the complexity and the cost of the system. Increasing the area of the detector increases its noise-equivalent power. Further, such a design will allow background radiation from a large area on the sea surface to fall on the detector and to increase the probability of receiving sun glints, both of which degrade performance. In the bistatic case, there is also the possibility that the laser spot will be obscured from the receiver by passing waves. These problems evidently become worse with increasing the angle between the optic axes of the transmitter and the receiver. Thus, if a bistatic design is used, the separation between the transmitter and the receiver should be as small as possible.

The difficulties from tracking do not arise in a monostatic system. The small obscuration of the receiving aperture by the transmitting aperture is a minor drawback. More importantly, the laser beam is visible to the receiver during its entire path, and the receiving aperture will receive backscatter by the atmosphere over the entire range. Fortunately, this radiation will not be in focus at the detector plane on which the water surface is imaged and suitable aperturing can then eliminate a large part of this background. In fact, the obscuration from the transmitting aperture and the physical dimension of the detector accomplish a major part of this selection. The bistatic design has an advantage only in this respect. A monostatic design or a bistatic design with closely spaced transmitter and receiver is indicated. The following discussions assume such a design.

a. Gaussian Laser Beams

Let the surface of the target be described by $w(u, v)$ and let the laser of power P watts be directed at the target along the w -axis. Let the laser beam waist radius be ω_0 and be situated in the plane $w = 0$. Thus, in any plane perpendicular to the w -axis, the amplitude of the Gaussian beam is

given by

$$E(u, v, w) = \left(4 Z_0 P / \pi \omega^2 \right)^{1/2} \exp(-r^2/\omega^2) \quad (2.3)$$

$$r^2 = u^2 + v^2 \quad (2.4)$$

where

$$\omega(w) = \omega_0 \left[1 + \left(\lambda w / \pi \omega_0^2 \right)^2 \right]^{1/2} \quad (2.5)$$

The power density distribution is then given by

$$p(u, v, w) = (2P/\pi \omega^2) \exp(-2r^2/\omega^2) \quad (2.6)$$

The power density at $r = \omega$ is e^{-2} of the value on the axis. It can be shown that 86.5% of the incident power is within a diameter of $2\omega(w)$; this diameter will be hereafter referred to as the spot diameter.

The power incident on a surface element dS on the surface at (u, v, w) is $p \, dudv$ where $dudv$ is the projection of dS on the (u, v) plane. On the basis of the scattering parameter defined by Eq. (2.1), in Section II. B. 1, the laser power scattered by the surface element dS per unit solid angle will be $p(u, v, w) \sigma(\beta, \beta, -\pi/2) \, dudv$ for a monostatic arrangement as seen from Figure 14.

Let the receiver be arranged to image the laser-illuminated spot at w onto the detector. The solid angle over which the receiver at range R of aperture area A_r collects the scattered laser power is (A_r/R^2) . The detector output corresponding to the laser power received from the surface element dS will be $p(u, v, w) \sigma(\beta, \beta, -\pi/2) (A_r/R_s^2) \rho \, dudv$, where ρ is the responsivity

of the detector and R_s is the range from dS to the receiver. The total detector output will be (when the detector area coincides with the image of the illuminated spot)

$$\begin{aligned}
 i &= A_r \rho \int_{\text{spot}} \frac{p(u, v, w)}{R_s^2} \sigma \left(\beta, \beta, -\frac{\pi}{2} \right) du dv \\
 &\cong \frac{A_r \rho \sigma}{(R-w)^2} \int_0^{\omega(w)} p(r, w) 2\pi r dr \\
 &= \frac{0.87 A_r \rho \sigma P}{(R-w)^2} \quad (2.7)
 \end{aligned}$$

since

$$R_s^2 = (R-w)^2 + r^2 \quad (2.8)$$

Here the assumptions are implicit that the depth of focus is sufficient to accommodate Δw , the surface height changes within the spot and that R and $R_s \gg \Delta w$ and ω . In the approximations indicated, the angular dependence of the scattering parameter is ignored (supported by experimental observations described earlier) and the beam spreading near the waist or the w -dependence of $p(u, v, w)$ is neglected. Background and noise contributions have been omitted. It should be noted that strictly the size of the detector should be changed as w changes to collect the radiation from the spot. In the subsequent discussion, the factor 0.87 will be replaced by unity.

If the laser beam of power P is modulated at frequency ν with a modulation depth M , the laser power at the transmitter is described by

$$P_{mod} = \frac{P}{2} [2 - M + M \sin 2\pi\nu t] \quad (2.9)$$

The time varying part of the detector response to the scattered laser power from the surface element dS at (u, v, w) will be

$$di = p(u, v, w) \frac{M}{2} \rho \sigma \left(A_r / R_s^2 \right) \sin \left[2\pi\nu \left\{ t - (2R_s/c) \right\} \right] dudv \quad (2.10)$$

where c is the velocity of light. A plane incident wavefront is assumed. Although this is strictly true only at the beam waist for a Gaussian beam, it is a very good approximation near the beam waist. Further, if an imaging system is used with a small detector, the optical path from dS to the detector over the entire receiving aperture is the same; i. e., no phase differences arise. The detector output due to the entire laser spot will be

$$i \approx \frac{MA_r \rho \sigma}{2(R-w)^2} \int_{\text{spot}} p(u, v, w) \sin \left[2\pi\nu \left\{ t - (2R_s/c) \right\} \right] dudv \quad (2.11)$$

Assumptions similar to those leading to Eq. (2.7) are implicit in arriving at this expression. To evaluate the detector output, an explicit expression for $w = w(u, v)$ is needed. We will consider several special cases to clarify some points and to understand the behavior of the total system.

b. Maximum Wave Heights

If the surface were a plane $w = k$, then

$$p = C \exp (-2r^2/\omega^2) \quad (2.12)$$

and

$$R_s = (R-k) \left[1 + \left\{ r/(R-k) \right\}^2 \right]^{\frac{1}{2}} \quad (2.13)$$

If

$$R-k \gg \omega, \quad (2.14)$$

then,

$$R_s \cong R-k. \quad (2.15)$$

Thus,

$$\begin{aligned} i &\approx \frac{MA_r \rho \sigma}{2(R-k)^2} \int_0^\omega p(r, k) \sin \left[2\pi \nu \left\{ t - \frac{2(R-k)}{c} \right\} \right] 2\pi r dr \\ &= \frac{MA_r \rho \sigma P}{2(R-k)^2} \sin 2\pi \nu \left\{ t - \frac{2(R-k)}{c} \right\}. \end{aligned} \quad (2.16)$$

If the phase of this signal is compared with the laser modulating signal, it is seen that the phase difference is $\frac{4\pi\nu}{c} (R-k)$. Because phase differences larger than 2π are redundant, the range itself cannot be unambiguously determined. However, if the target plane moved to $w = k + \Delta$, the accompanying change in the phase difference will be

$$\delta \phi = (4 \pi \nu / c) \Delta . \quad (2.17)$$

If we can determine the phase unambiguously only over 2π radians (or 360 degrees), then the maximum excursion of the target Δ_{\max} , is related to the modulation frequency by

$$2\Delta_{\max} \leq (c/\nu) . \quad (2.18)$$

However, this condition can be relaxed since the phase can be monitored continuously, and the target does not move abruptly causing phase changes of exactly 2π or multiples thereof. Thus, we may say

$$2\Delta_{\max} \leq n c / \nu \quad (2.19)$$

where n is a small integer. It should be noted that the linear relation between target excursion and change in phase of the return given in Eq. (2.17) is based on the condition that

$$\frac{2\pi\nu\omega}{c} \ll 1 \quad (2.20)$$

in addition to the condition in Eq. (2.14). Combined with the relation in Eq. (2.19),

$$n\pi\omega \ll \Delta_{\max} \quad (2.21)$$

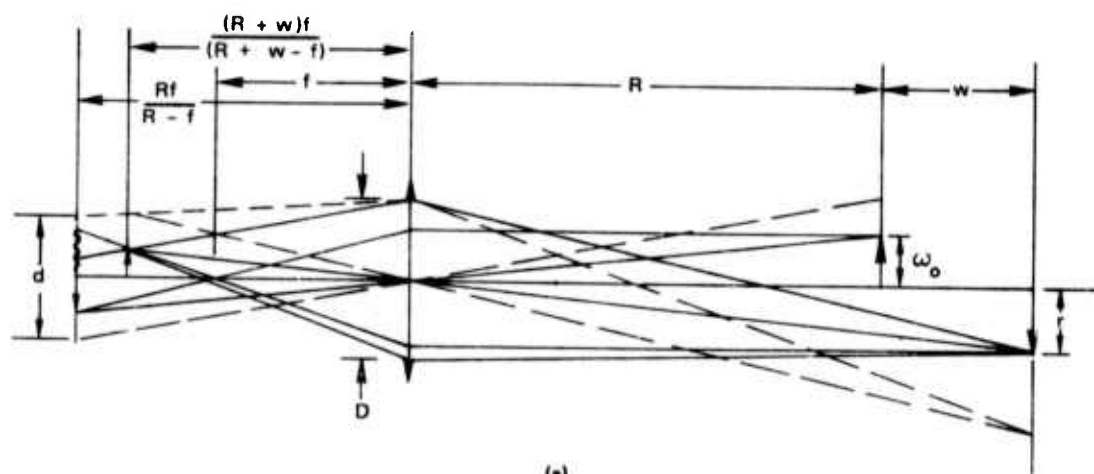
is obtained. In the current application, the value of Δ_{\max} is determined in the first instance by the height of the gravity waves. If we assume that 3-m waves will be encountered and that $n = 2$ (i.e., a total phase excursion of 720° is allowed), then the modulating frequency can be 100 MHz.

The maximum allowable wave heights also are influenced by other considerations. The laser-illuminated spot on the surface of the water will move

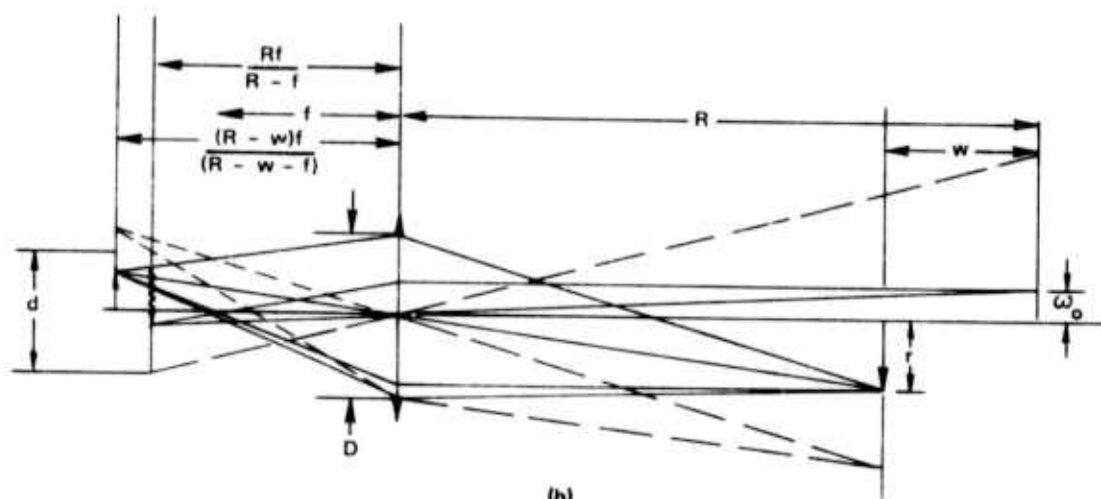
up and down (in two dimensions for the general case of oblique incidence) with the waves. If the transmitting and receiving optical systems are simple and do not track the movement of the surface, the divergence of the Gaussian beam away from the waist leads to a larger spot on the water and a larger image. At the detector plane, the image will be out of focus and will result in a blurred image much larger than a detector matched to the waist radius ω_0 . Further, the peak (axial) intensity decreases as both ω and the area of the spot increase, as indicated by Eq. (2.6). All these factors will decrease the detector output. The limitations imposed on the wave-heights by these considerations are examined in the following subsections.

1. Depth of Field of the Receiver

Let the receiver of focal length f and aperture diameter D_r be located at a distance R from the position of the beam waist of radius ω_0 . The detector at the image plane is of diameter d larger than the image of the beam waist. Figure 15 shows that as the waves change in height, all the radiation collected by the receiver may still be intercepted by the detector; but each point on the source is spread into an ellipse of confusion. As $|w|$ increases, eventually some of the radiation is no longer intercepted by the detector. Even in the geometrical optics regime (ignoring diffraction effects), no unique or totally satisfactory method exists for defining a maximum allowable value of w (especially when a Gaussian spot is the source). For our purposes, we shall limit the range of w such that at w_{\max} , the ellipse of confusion corresponding to the point $r = x\omega$ just begins to fall outside the detector. In other words, at w_{\max} , the detector intercepts all the radiation collected by the aperture from within a circular area of radius $x\omega$ ($x < 1$), and $(1 - e^{-2x^2})$ of the laser power is incident on this area. Thus, having the detector larger than the image of the beam waist and allowing x to take values less than unity implies that the signal amplitude will change as the wave height changes. This range of w -values will then determine the receiver's depth of field or the maximum allowable wave heights.



(a)



(b)

SA-2422-20

FIGURE 15 RECEIVER OPTICS

The maximum values of w can be shown to be given by

$$w_+ = 2\omega_o R \frac{N (D_r - 2\omega_o N) - x \left[(D_t^2/2) (N^2 - x^2) + (D_r - 2\omega_o N)^2 \right]^{\frac{1}{2}}}{(D_r - 2\omega_o N)^2 - x^2 (D_t^2/2)} \quad (2.22)$$

from Figure 15(a) and

$$w_- = 2\omega_o R \frac{N (D_r + 2\omega_o N) - x \left[(D_t^2/2) (N^2 - x^2) + (D_r + 2\omega_o N)^2 \right]^{\frac{1}{2}}}{(D_r + 2\omega_o N)^2 - x^2 (D_t^2/2)} \quad (2.23)$$

from Figure 15(b), where

$$N = d (R - f) / 2\omega_o f \quad (2.24)$$

and

$$D_t = \sqrt{2} (2R\lambda / \pi\omega_o) \quad (2.25)$$

It will be seen that D_t is equal to the transmitting aperture or $\sqrt{2}$ times the diameter of the Gaussian beam at the receiver. The significance of N is seen when it is noted that $2\omega_o f / (R - f)$ is the diameter of the image of the beam waist (of diameter $2\omega_o$) at range R . The diameter of the detector d is then N times larger than this image. Thus, when the circle of confusion related to the image of the laser illuminated spot ($x = 1$) just fills the detector, it is also N times larger than the image of the beam waist. Then, $(w_+ + w_-) = W$ is the depth of field of the receiver or the maximum allowable changes in wave height. If $2\omega_o N$ can be neglected compared with the diameters of the receiving and transmitting apertures,

$$w_+ \cong w_- \cong w_{\max} \quad (2.26)$$

and

$$W = (w_+ + w_-) \cong 4\omega_0 R \frac{ND_r - x \left[(D_t^2/2) (N^2 - x^2) + D_r^2 \right]}{D_r^2 - x^2 \left(D_t^2/2 \right)}^{\frac{1}{2}} \quad (2.27)$$

It should be emphasized that Eq. (2.27) gives a value for the maximum wave height for the assumed criterion. A less strict criterion may be sufficient, thus allowing larger wave heights.

In Figures 16-18, the depth of field at 10.6 μm is plotted as a function of receiving aperture for $x = 1$ and several values of the beam waist, the range, and N . The dependence of the depth of field on the several parameters is seen from these curves. It should be noted that increasing the size of the beam waist at constant N implies enlargement of the detector area. A comparison of Figures 16 and 17 with Figure 19 -- where the optical wavelength is 2 μm -- shows the effect of the wavelength of the radiation. The increase in the depth of field on reducing the wavelength by a factor of five is seen to be approximately equivalent to that on increasing the beam waist by a factor of two.

2. Depth of Focus of the Transmitter and Horizontal Resolution

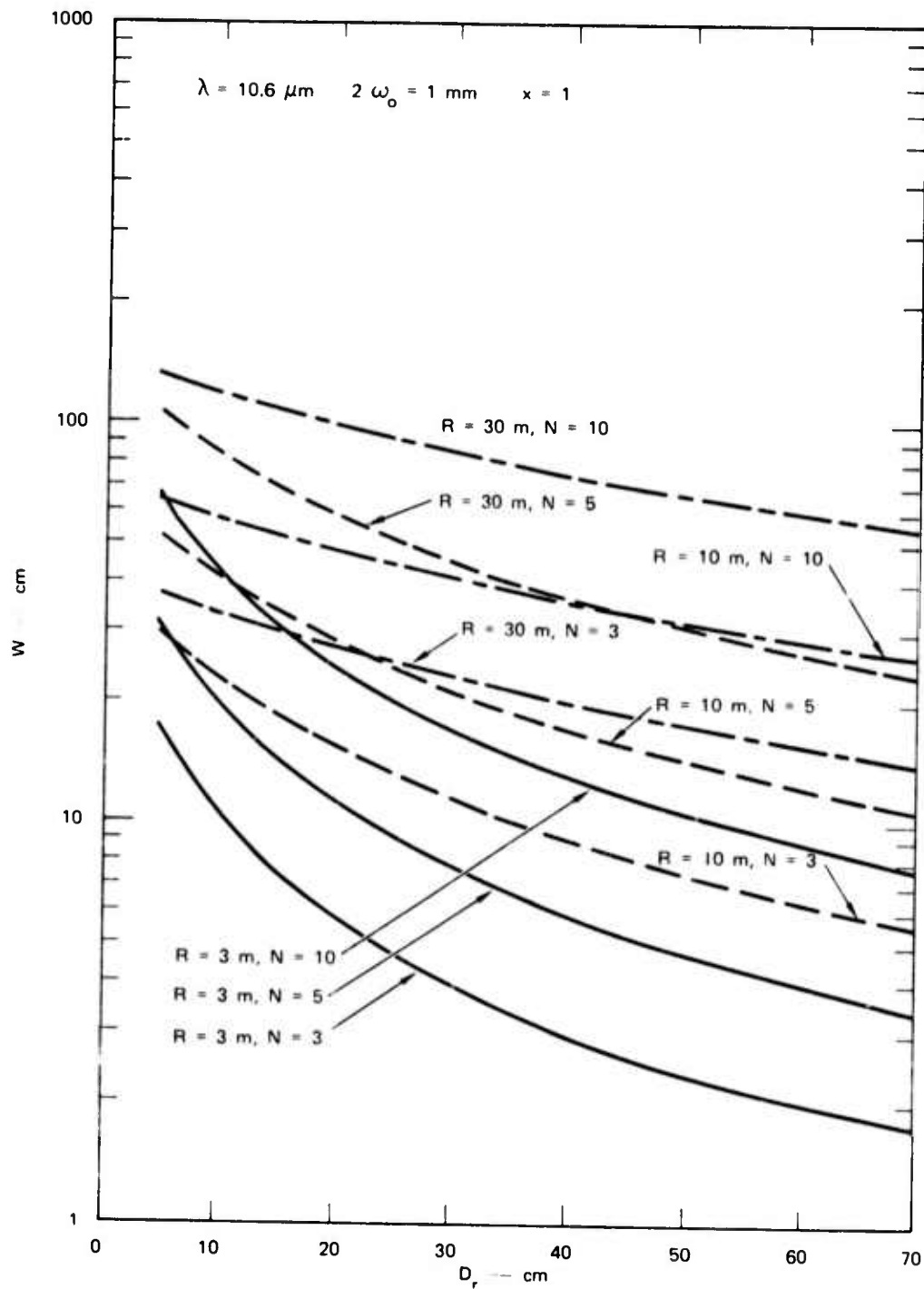
For large w ($w \gg \omega_0$), Eq. (2.5) may be approximated by

$$\omega(w) = \lambda w / \pi \omega_0, \quad (2.28)$$

and for $w = R$,

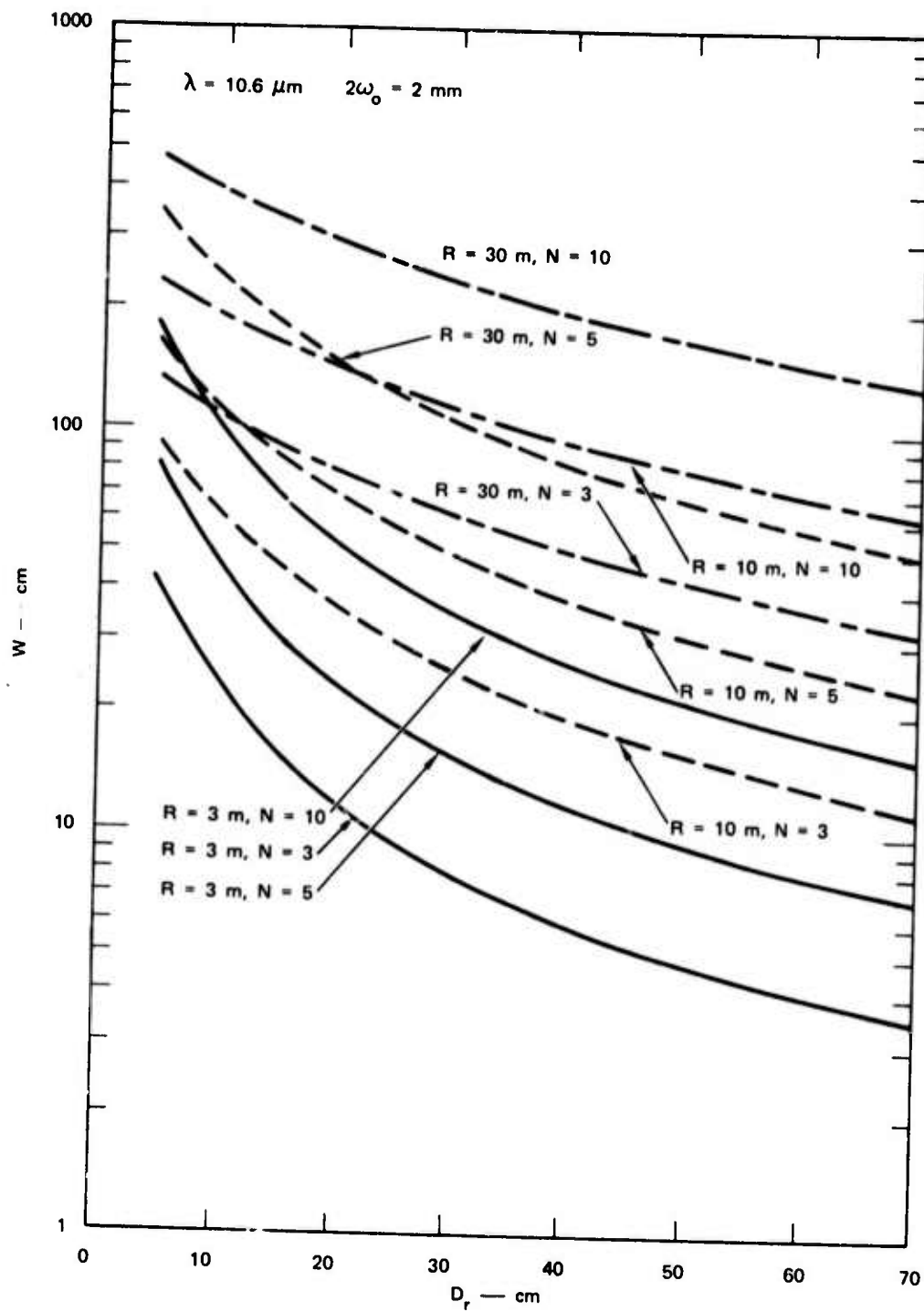
$$\omega(R) = \lambda R / \pi \omega_0. \quad (2.29)$$

In other words, the Gaussian beam will have an e^{-2} diameter of $2\omega(R)$ at R . Since 98 percent of the power in a Gaussian beam is within a radius of $\sqrt{2}\omega$,



SA-2422-21

FIGURE 16 DEPENDENCE OF DEPTH OF FIELD OF RECEIVER ON
 APERTURE FOR SPOT SIZE OF 1 mm FOR 10.6 μm
 RADIATION



SA-2422-22

FIGURE 17 DEPENDENCE OF DEPTH OF FIELD OF RECEIVER ON
 APERTURE FOR SPOT SIZE OF 2 mm FOR 10.6 μm
 RADIATION

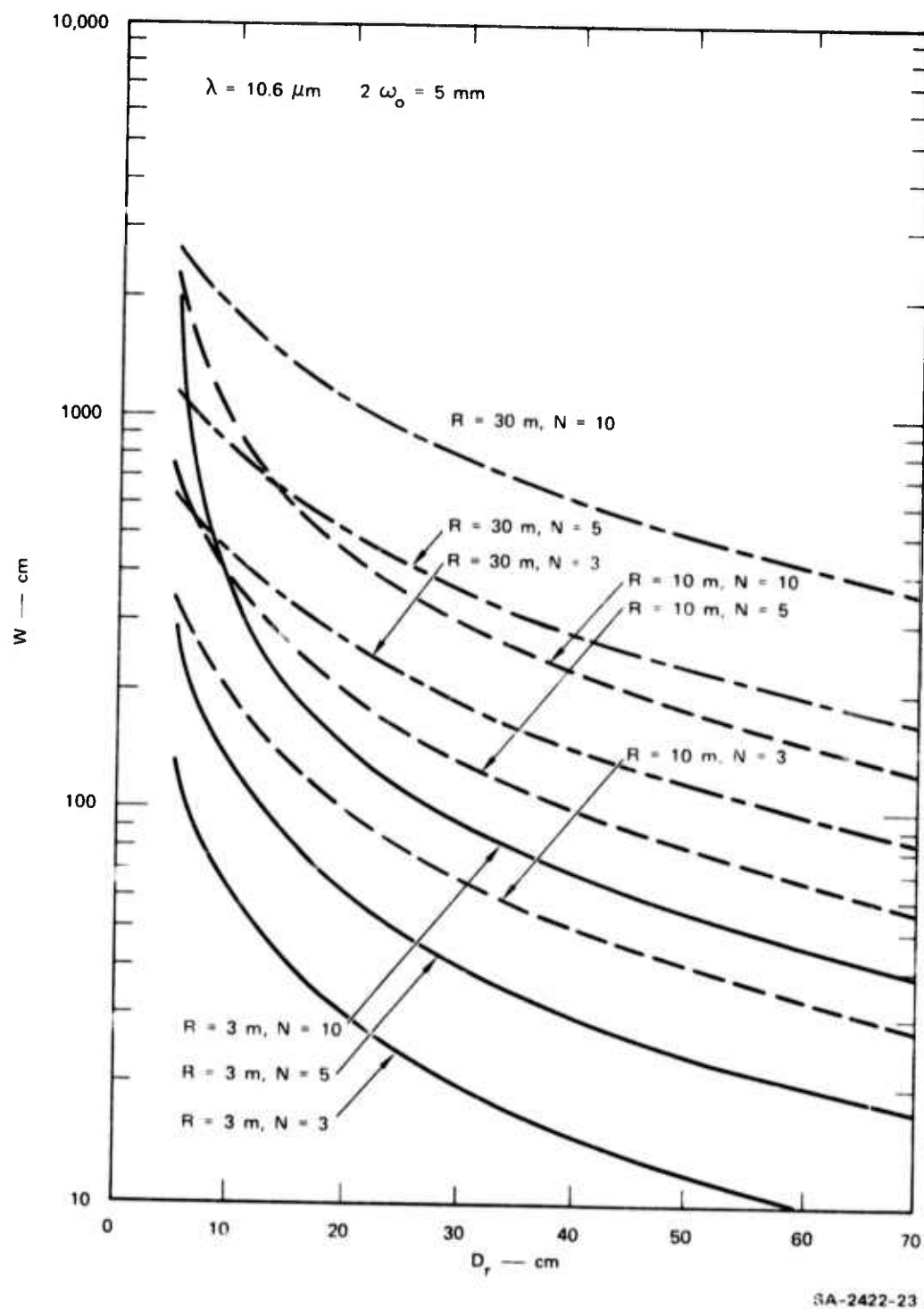
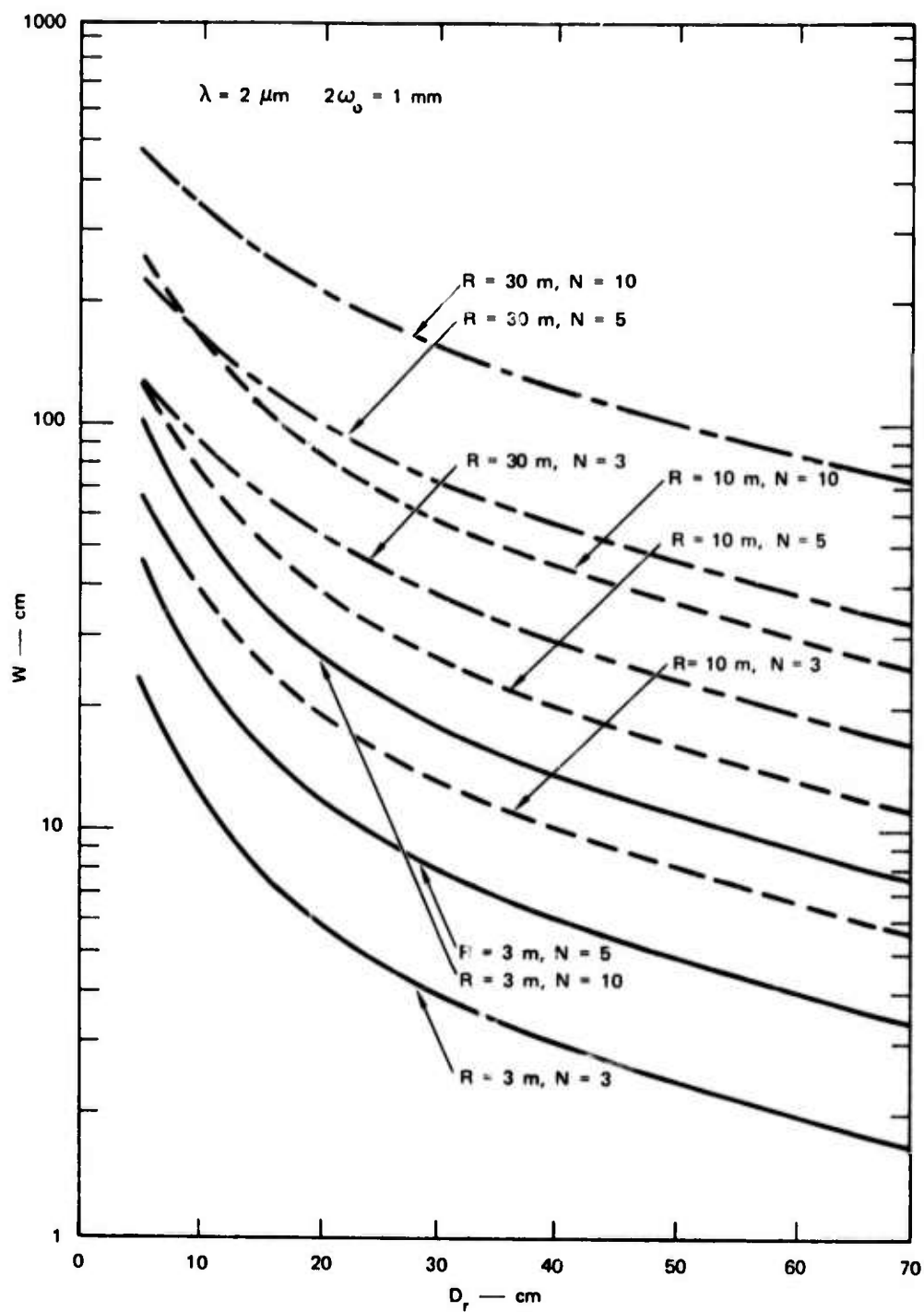


FIGURE 18 DEPENDENCE OF DEPTH OF FIELD OF RECEIVER ON APERTURE FOR SPOT SIZE OF 5 mm FOR $10.6 \mu\text{m}$ RADIATION



SA-2422-24

FIGURE 19 DEPENDENCE OF DEPTH OF FIELD OF RECEIVER ON
 APERTURE FOR SPOT SIZE OF 1 mm FOR $2 \mu\text{m}$
 RADIATION

a transmitting aperture of diameter $D_t = \sqrt{2} \omega$ will produce at range R a Gaussian beam waist of e^{-2} radius ω_0 . Thus,

$$D_t = 2 \sqrt{2} \lambda R / \pi \omega_0. \quad (2.30)$$

In Figure 20, the transmitting apertures needed for producing various sizes of beam waist at several ranges are plotted for $10.6 \mu\text{m}$. The same curves also may be used for other wavelengths because λ and R have an inverse relationship in Eqs. (2.29) and (2.5). Figure 20 is based on Eq. (2.5) which is more exact than Eq. (2.30).

From the earlier discussion of the receiver, it is evident that for the monostatic design considered, the depth of focus of the transmitter is identical with the depth of field of the receiver. That is, if we define the former as the distance over which all the radiation from the laser-illuminated spot (e^{-2x^2} diam) collected by the receiving aperture D_r is still incident on the detector (neglecting diffraction).

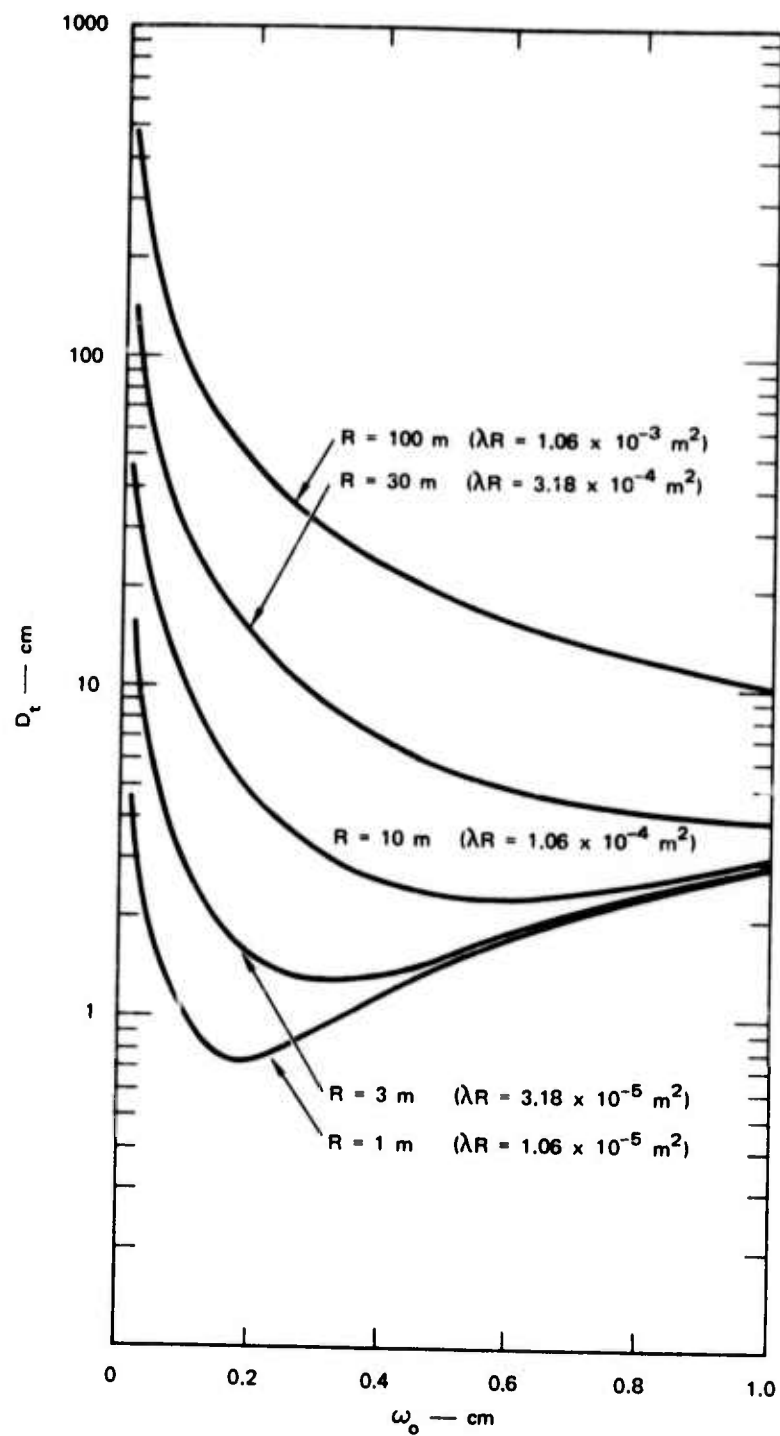
The spot diameter varies with the wave height according to Eq. (2.28) and as shown in Figure 21. The figure shows that the divergence of the beam increases as the waist size decreases. Though Figure 21 is plotted for $10.6 \mu\text{m}$ radiation, the same curves may be used for other wavelengths by changing the x-axis scale. Shorter wavelengths therefore result in less beam divergence, or larger depth of focus, or smaller transmitting aperture.

The maximum spot diameter over the depth of focus determines the worst-case horizontal resolution of the system. Since $w_+ > w_-$, the largest spot size occurs at w_+ away from the waist. Let us assume that $2m \omega_0$ is this maximum spot size. From Eqs. (2.5) and (2.27), the factor m shown to be related to N and the apertures by

$$m \cong (1 - kx^2)^{-1} \left[(1 - kx^2)^2 + k \left\{ N - x \left[1 + k(N^2 - x^2) \right] \right\}^2 \right]^{\frac{1}{2}} \quad (2.31)$$

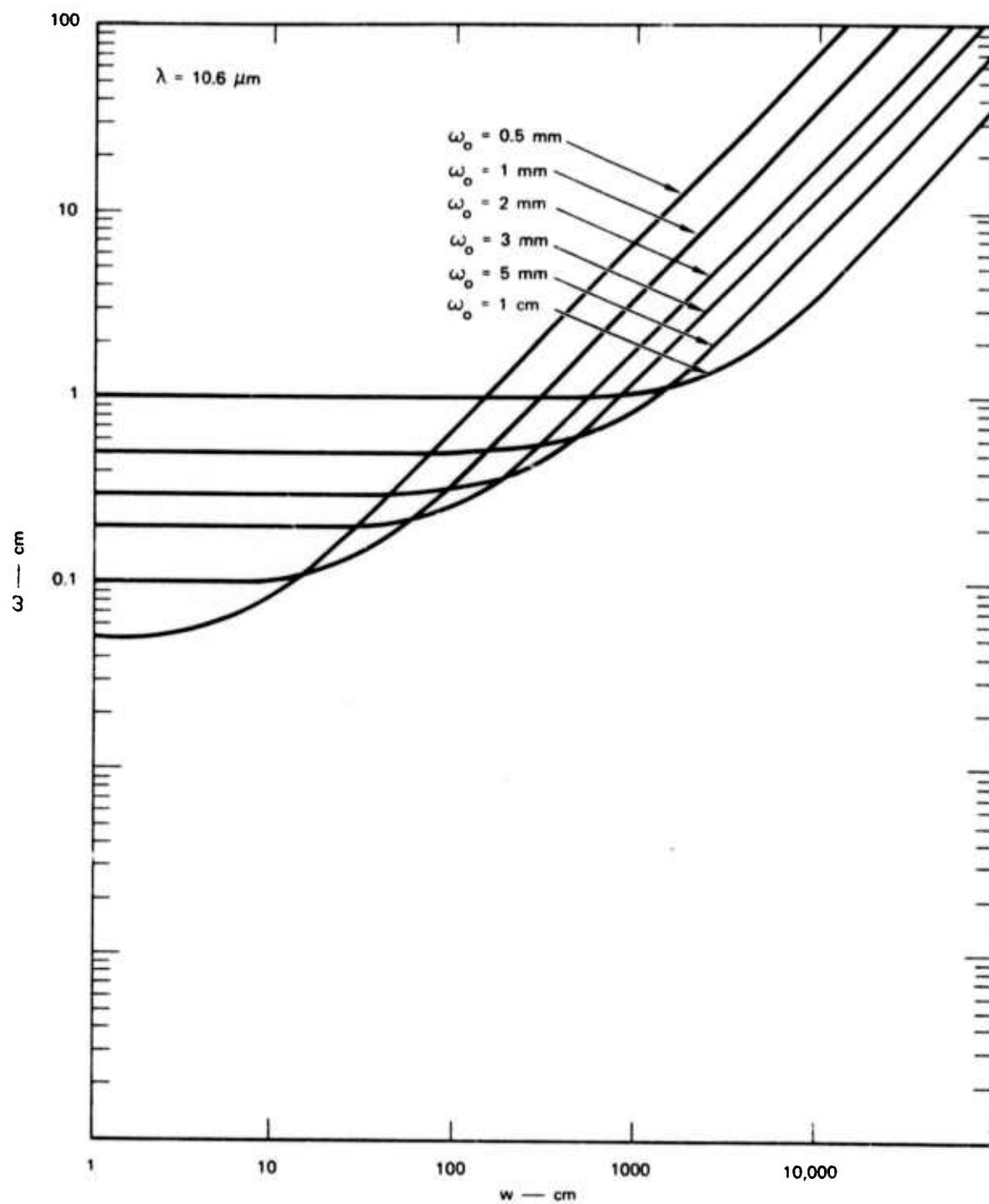
where

$$k = D_t^2 / 2D_r^2. \quad (2.32)$$



SA-2422-25

FIGURE 20 DEPENDENCE OF TRANSMITTING APERTURE ON SIZE OF BEAM WAIST FOR DIFFERENT RANGES OR OPTICAL WAVELENGTHS



SA-2422-26

FIGURE 21 DEPENDENCE OF GAUSSIAN BEAM ($1/e^2$) RADIUS ON DISTANCE FROM THE BEAM WAIST

It will be seen later that the number of speckles the receiver intercepts is approximately $(1/k)$ and that to avoid large fluctuations in signal, $(1/k)$ should be larger than 10. From Eq. (2.31) for $x = 1$ and $k = 0.1$, m has values of 1.15, 1.49 and 2.56 for N values of 3, 5, and 10 respectively; for $k = 0.03$, m has values of 1.06, 1.20 and 1.74 respectively for the same N values. It is thus seen that the horizontal resolution is not degraded if the aperture ratios and the detector size (N) are in the above region.

c. Minimum Detectable Wave Heights or Height Resolution

The smallest excursion of a target Δ_{\min} that can be measured is determined by the smallest phase difference that can be reliably measured, i.e., by the phase resolution of the phase meter. If this resolution is ψ rad, then from Eq. (2.17)

$$\Delta_{\min} = \psi / 4\pi\nu \quad . \quad (2.33)$$

Combining Eqs. (2.33) and (2.19), we get

$$\Delta_{\min} \geq (\Delta_{\max}/n) (\psi/2\pi) \quad . \quad (2.34)$$

The value of Δ_{\min} is determined by the available phase resolution and the modulating frequency or equivalently by (Δ_{\max}/n) . For a modulating frequency of 100 MHz and a phase resolution of 0.1° , $\Delta_{\min} = 0.4$ mm.

However, the above result and Eq. (2.17) assume that the target is a plane normal to the beam and that the returns originate at the surface. Further, in deriving Eq. (2.10), the assumption was made that the receiver system imaged the laser spot on the detector; thus, the optical path lengths are the same for rays proceeding along different paths. In the application to wave surfaces, none of these assumptions is strictly true. The target is neither planar nor normal to the beam in general. In addition, the scattered radiation originates from a surface layer of finite thickness. Finally, when realistic wave heights are accommodated, imaging of the laser spot on the detector is no longer possible without tracking the wave surface. Each of these factors introduces a small systematic error in the phase of the signal. We examine them in the following paragraphs.

The penetration of laser radiation into the water causes scattering in the bulk of the water. If a signal $A \sin 2\pi\nu t$ is incident on the surface, the return from a depth w will be [using Eq. (2.16)]

$$d i(w) = B \sin 2\pi\nu \left\{ t - \frac{2(R+w)}{c} \right\} e^{-2\alpha w} dw \quad (2.35)$$

where B is a constant and α is the attenuation of water for the laser radiation. The output of the detector would be

$$\begin{aligned} i &= B \int_0^\infty e^{-2\alpha w} \sin 2\pi\nu \left\{ t - \frac{2}{c}(R+w) \right\} dw \\ &= \sqrt{4\alpha^2 + (4\pi\nu/c)^2} B \sin \left[2\pi\nu \left\{ t - \frac{2R}{c} \right\} - \delta \right] \end{aligned} \quad (2.36)$$

where

$$\delta = \arcsin \left\{ 4\pi\nu \left[4\alpha^2 c^2 + 16\pi^2 \nu^2 \right]^{-1/2} \right\} . \quad (2.37)$$

Thus, the phase error introduced is δ which depends on the attenuation length α and the modulation frequency. If this error is to be below the resolution of the phase measurement, then $\psi > \delta$ or

$$\alpha > 2\pi\nu/c\psi . \quad (2.38)$$

For $\psi = 0.1^\circ$, and $\nu = 100$ MHz, $\alpha > 12 \text{ cm}^{-1}$. The attenuation length for $10.6 \mu\text{m}$ is on the order of 10^3 cm^{-1} . Thus, essentially no phase error results in this case.

Simple analytical expressions cannot be obtained for the effects of the slope and the curvature of the surface in the general case. We illustrate the essential point by examining the phase of the detector output when a square illuminating beam of uniform power density ρ and area $(2\omega)^2$ is incident along

the w-axis on a planar and a symmetrical triangular target of given slopes.
Let the surface be described by

$$w = u \tan \theta \quad (2.39)$$

for the planar target and

$$w = \begin{cases} u \tan \theta & u > 0 \\ -u \tan \theta & u < 0 \end{cases} \quad (2.40)$$

for the triangular target. With the use of Eq. (2.16), the detector output for the inclined planar target will be

$$i = B' \operatorname{sinc} \left(\frac{4\pi\nu\omega}{c} \tan \theta \right) \sin 2\pi\nu \left(t - \frac{2R}{c} \right). \quad (2.41)$$

By taking the range of the target at the beam center as the correct range, we realize that no phase error results. Interestingly, the amplitude depends on the slope of the target. It may thus be useful to monitor the amplitude of the signal and the phase to determine the slope of the surface. However, Eq. (2.16) has to be evaluated for two-dimensional surfaces for realistic cases before the possibility of slope determination by amplitude measurement can be ascertained.

For the target with a triangular depression at the center, Eqs. (2.16) and (2.40) lead to the detector output

$$i = B'' \operatorname{sinc} \left(\frac{2\pi\nu\omega}{c} \tan \theta \right) \sin 2\pi\nu \left\{ t - \frac{2R}{c} + \frac{\omega \tan \theta}{c} \right\}. \quad (2.42)$$

If, once again, the range of the target at the beam center is taken as the correct value, the phase of the detector output leads to an error of $(2\pi\nu\omega \tan \theta/c)$. If this error is to be smaller than the phase measurement error ψ , then

$$\nu\omega < c\psi/2\pi \tan \theta. \quad (2.43)$$

If we assume that $\psi = 0.1^\circ$ and that the maximum slopes encountered on the surface of the water are 30° , then

$$\nu \omega < 1.4 \times 10^7 \text{ cm s}^{-1} . \quad (2.44)$$

If $\nu = 10^8$ Hz, then $\omega = 1.4$ mm, or the maximum spot diameter is about 3 mm. Thus, using 100 MHz modulation is compatible with the feasible spot sizes and probable slopes. It should be noted that the Gaussian intensity distribution of the laser beam weights the phase distribution in favor of the beam center and the condition on ω may be somewhat relaxed.

In general, it is seen that the planar portions of the surface do not give rise to a phase error, but rather a curvature within the beam leads to a phase error that imposes limitations on the modulating frequency or the beam diameter. It is also obvious that the system will be insensitive to large changes in the height of waves with wavelengths shorter than the beam diameter. However, such large changes imply very steep wave slopes that are improbable.

The height resolution limits the spatial frequency of the waves to which the system responds if a maximum slope is assumed. Consider sinusoidal waves described by $A \sin(2\pi u/L)$. The peak-to-peak amplitude is $2A$, and the maximum slope is $(2\pi A/L)$. If $\tan \theta$ is the maximum slope, then the maximum wave height of waves of this frequency is $(L \tan \theta / \pi)$. This corresponds to a phase difference of $(4\nu L \tan \theta / c)$. If this is less than the phase resolution, the waves are not detected. In other words, the system detects waves of wavelength longer than

$$L \geq (c \psi / 4 \nu \tan \theta) . \quad (2.45)$$

For $\nu = 10^8$, $\psi = 0.1^\circ$, $\theta = 30^\circ$, and $L = 2.3$ mm which is on the same order as the beam width.

The effect of the noncoincidence of the image plane and the detector plane caused by wave-height changes can be estimated with reference to Figure 15(c). It is seen that when the target is a distance w from the beam waist, the image is formed at a distance $(R + w) f / (R + w - f)$ from the lens. The detector is situated at a distance $Rf / (R - f)$. Consider the rays originating from the $(1/e^2)$ point on the beam. They become focused at the position of the image and continue on to the detector. At the image plane, the path differences are zero. Beyond the image plane, the maximum path difference exists between the ray that is normal to the detector and the outermost ray that barely falls on the detector. The distance traveled by the ray normal to the detector is

$$wf^2 / (R - f) (R + w - f) . \quad (2.46)$$

The distance traveled by the outermost ray is

$$wf \left[(D_r + d)^2 (R - f)^2 + (2 Rf)^2 \right]^{1/2} / 2 R (R - f) (R + w - f) . \quad (2.47)$$

The path difference is

$$\left[wf / (R - f) (R + w - f) \right] \left[\sqrt{ \left| (D_r + d)^2 (R - f)^2 / 4 R^2 \right| + f^2 } - f \right] . \quad (2.48)$$

When $R \gg w$ and f and $D_r \gg d$, the path difference is approximately

$$wf^2 / \left[(R - f) (R + w - f) 8 \mathcal{F}^2 \right] \cong (w/2\pi) \Omega_r \quad (2.49)$$

where \mathcal{F} is the f number and Ω_r is the receiving aperture in sr.

This path difference will cause a phase change in the detector output. However, on integrating over not only the point but also the entire spot appropriately weighted by the Gaussian intensity distribution, the phase change of the output will be less than the phase difference corresponding to the maximum path difference calculated above. The latter will then represent an upper bound on the phase error from this source. From Eq. (2.17) this upper bound is

$$(4\pi\nu/c) (w/2\pi) \Omega_r = (2\nu w \Omega_r/c) . \quad (2.50)$$

If this error is less than ψ -- the resolution of the phase measurement -- no error results, i.e.,

$$\psi < 2\nu w \Omega_r/c . \quad (2.51)$$

For $\nu = 10^8$ Hz, $w = 20$ cm, $\Omega_r = 10^{-3}$, the upper bound is $8 \times 10^{-3}^\circ$, while the phase resolution is 0.1° . Thus, this source of phase error need not cause concern.

d. Speckle Considerations

Since a coherent optical source is used to illuminate the diffuse scatterer, a speckle pattern will be expected to exist at the receiver.¹⁰ Since the water surface will be moving, the speckle pattern will not be stationary in time and will lead to fluctuations in the total incident power and in the detector output. The extent of the fluctuations may be estimated by calculating the number of speckles present in the receiving aperture. When a target of $2\omega_0$ diam is illuminated with a coherent source, the size of a speckle in the aperture plane at range R is approximately $(R\lambda/2\omega_0)$.

When compared with Eq. (2.30), this is equal to the size of the transmitting aperture at range R. The number of speckles intercepted by the receiver aperture is

$$M_s = 4\omega_0^2 D_r^2 / R^2 \lambda^2 \approx 2D_r^2 / D_t^2. \quad (2.52)$$

The fluctuations in the number of speckles will be $\sqrt{M_s} = \sqrt{2} D_r / D_t$. Since the water surface moves rather slowly, the effect of the speckle will be to introduce amplitude changes at this slow rate -- perhaps 1 KHz. When compared with the laser modulating frequency at about 100 MHz, the phase measurement will not be degraded because the speckles mainly influence the dynamic range of the detector output. This dynamic range will be within ± 3 dB if the number of speckles in the receiver aperture is on the order of ten. This implies that at the same range the receiving aperture diameter is at least three times that of the transmitting aperture to avoid very large fluctuations in detector output.

e. Background Sources

Along with the laser radiation scattered by the water surface, radiation from several other sources is also incident on the receiver. These sources are the:

- Thermal radiation from the objects in the field of view of the detector

- General background solar radiance reflected by the water surface
- Occasional "glints" or specular reflections of the sun or the laser by an appropriately oriented wave facet
- Backscattering of the laser beam by the atmospheric constituents such as the air molecules, aerosols, salt crystals, and spray.

The sources that are not modulated can be rejected by appropriate electrical filtering. However, they constitute the DC level of the detector current, increases in which increase the shot noise and degrade the detection capability of the detector. Although the atmospheric scattering is modulated, it occurs over a long path length and also contributes to the DC level. These factors are considered in the following paragraphs.

Thermal Radiation -- The peak emission of a blackbody at room temperature occurs at a wavelength of approximately $10\text{ }\mu\text{m}$ at the rate of $3.13 \times 10^{-3}\text{ W cm}^{-2}\text{ }\mu\text{m}^{-1}$.¹¹ The total emission over all wavelengths occurs at the rate of $4.6 \times 10^{-2}\text{ W cm}^{-2}$. For equilibrium, radiation from its surroundings at 300°K must fall on the blackbody at the same rates. The detector is surrounded by objects at 300°K and is thus receiving radiation at all times from all objects in its field of view. A detector with a field of view of 30° will then receive $6.7 \times 10^{-5}\text{ W cm}^{-2}\text{ }\mu\text{m}^{-1}$ at $10\text{ }\mu\text{m}$ or a total of $9.8 \times 10^{-4}\text{ W cm}^{-2}$, since blackbodies are Lambertian sources. The detector response falls off at higher wavelengths, say $15\text{ }\mu\text{m}$, and 56 percent of the energy radiated by a blackbody at 300°K is below $15\text{ }\mu\text{m}$. Hence, only $5.5 \times 10^{-4}\text{ W cm}^{-2}$ generates a background (DC) signal level (assuming flat response until $15\text{ }\mu\text{m}$). If, however, a cooled filter of bandwidth $0.5\text{ }\mu\text{m}$ centered about $10.6\text{ }\mu\text{m}$ were placed in the optical train, only $3.35 \times 10^{-5}\text{ W cm}^{-2}$ would contribute to the background. Because the size of a typical detector is on the order of 0.25 mm^2 , the thermal radiation contributing to the DC level, incident through a 30° field of view, is $1.34 \times 10^{-6}\text{ W}$ or $8.4 \times 10^{-8}\text{ W}$ with a cooled filter. The value of the detection parameter of the detector is based on use with a 30° field of view in a 300°K background. The

above value of background power is thus useful for comparison of other sources of DC signal in the detector.

Solar Irradiance and Sky Radiance -- As seen from Figure 15, the detector receives radiation from a region on the surface of the water which is approximately as large as the image of the detector. Thus, the dimension of this region is N times the waist diameter for which the optical system is designed. Since N is a small number [Refer to Eq. (2.24)] and beam waists are on the order of mm, an area on the order of a square cm on the surface should be considered.

The spectral irradiance of the sun at the surface of the sea at $10.6 \mu\text{m}$ is $2.5 \times 10^{-5} \text{ W cm}^{-2} \mu\text{m}^{-1}$.¹² A diffusely scattered component will always be incident on the receiver regardless of the position of the sun. Using the scattering parameter measured experimentally, ($\sigma = 4.6 \times 10^{-6} \text{ sr}^{-1}$) in Eq. (2.1), we calculate that $1.15 \times 10^{-12} \text{ W } \mu\text{m}^{-1}$ will be incident on the detector per cm^2 of the surface for a receiving aperture of 10^{-2} sr . Thus, the solar background is seen to be completely negligible compared with the thermal background if a filter of $0.5 \mu\text{m}$ bandwidth is used. In fact, the combination of atmospheric attenuation and the reduction in the response of the detector at shorter wavelengths may be sufficient filtering from this consideration.

The sky presents a background radiation from scattering and emission by atmospheric particles. In the $10 \mu\text{m}$ region, this radiation behaves very much like a 300°K blackbody and has a value of $2 \times 10^{-4} \text{ W cm}^{-2} \mu\text{m}^{-1} \text{ sr}^{-1}$.¹³ The surface of the water will reflect about 1 percent of this radiation into the receiving aperture of 10^{-2} sr . Thus, the sky radiance incident on the detector is $2 \times 10^{-8} \text{ W } \mu\text{m}^{-1}$ per cm^2 of the surface or $10^{-8} \text{ W per cm}^2$ if a $0.5 \mu\text{m}$ bandwidth filter is used. This level is again negligible compared with the thermal background.

Sun Glints and Specular Laser Returns -- Direct reflection of the sun by an appropriately oriented facet into the receiver will happen occasionally. For a reflectivity of 1 percent at $10.6 \mu\text{m}$, a facet of 1 cm^2 in area

will reflect 1.25×10^{-7} W into the detector through a $0.5 \mu\text{m}$ filter. This is not a high signal level and occurs only occasionally. The filter assumes far more importance in this case.

Potentially more serious is that at times the surface will be in the proper orientation to specularly reflect the laser energy into the receiver. With a reflectivity of 1 percent high power densities could result at the detector if the reflection were imaged on the detector.

The probability of getting a specular return may be minimized by tilting the laser beam to an incidence angle greater than 30° since most of the wave slopes are below 30° . Nevertheless, to have a detector that can handle both the high-power densities for short periods and the dynamic range without performance deterioration is desirable. It is reported that HgCdTe detectors can withstand a single shot energy density of about 0.5 KJ cm^{-2} without damaging the detector.¹⁴ For short durations, very high-power densities can thus be tolerated. If a laser of power 10 W is reflected by water and is imaged on a detector with a spot size of about 0.2 mm, the power density will be 25 KW cm^{-2} . Short (ms) exposures at this level have a small energy density compared with the above value and should not cause problems.

Atmospheric Backscatter-- As mentioned earlier in this section, molecular scattering by molecules of water in the skin depth does not account for the measured diffuse scattering from the water because molecular scattering based on an assumed Rayleigh cross-section of $10^{-32} \text{ cm}^2 \text{ molecule}^{-1} \text{ sr}^{-1}$ at $10.6 \mu\text{m}$ is seven decades below the measured scattering. Since the density of air is three decades smaller than that of water, 1 cm of air has the same number of molecules as $10 \mu\text{m}$ of water (per unit cross-section). Thus, a long path in air is necessary to obtain an appreciable contribution to the receiver input from air scattering. Most of this scatter will be very much out of focus at the detector. Because of the physical size of the detector, the backscatter essentially from a fraction (near the surface) of the total path length will be incident on the detector. In addition, when the laser beam is amplitude-modulated, the low level return from a long path will have the phase

information smeared, and the corresponding detector output will be an averaged small DC value. For these reasons, therefore, air scattering is not expected to be a serious problem.

The backscatter from aerosols can be appreciable. However, if the aerosol has a continuous distribution, its effect on the phase-ranging system will be to increase the DC level as before. If the aerosol is localized, phase confusion could result. However, no quantitative estimates can be made without knowledge of the scattering efficiency or density of scatterers.

5. Detector

For operation in the 10.6 μm region, several detector materials have been developed. For the projected application, the frequency response of the detector must extend to 100-200 MHz because modulation of the laser radiation at 100 MHz is contemplated. Photoconductive doped-germanium detectors, pyroelectric detectors, and photovoltaic HgCdTe detectors all have desirable characteristics. Of these, HgCdTe has the highest responsivity, has been under active development for communication receivers,¹⁵ and appears to be the best choice for the current application to phase-ranging.

Operated in the photovoltaic mode at liquid nitrogen temperatures, HgCdTe has frequency response in the GHz range and high responsivity. It is also now available commercially with detector areas on the order of 0.25 mm² and detectivities in the range $3 \times 10^9 < D^* (10.6 \mu\text{m}, 1800 \text{ Hz}, 1 \text{ Hz}) < 10^{10} \text{ cm Hz}^{1/2} \text{ W}^{-1}$ for a 30° field-of-view of the background at 300°K. Quantum efficiencies claimed are on the order of 10 percent. As already noted, the material reportedly has a high threshold for damage by high-power densities.¹⁴

The expected performance of the detector may be estimated as follows. The signal-to-noise ratio (S/N) of an IR detector is related to the incident power ΔP and the noise-equivalent power (NEP) of the detector as given by

$$(S/N) = \Delta P / \text{NEP} \quad (2.53)$$

The noise-equivalent power of the detector is related to its detectivity parameter D^* , its area A_d and the (electronic) bandwidth Δf centered at the modulating frequency, used in subsequent processing, by

$$NEP = (A_d \Delta f)^{1/2} / D^* \quad (2.54)$$

or

$$(S/N) = \Delta P D^* / (A_d \Delta f)^{1/2}. \quad (2.55)$$

It should be emphasized that the quantities (S/N) and ΔP refer to the values at the modulating frequency.

The general equation (2.55) above may be applied to the current case as follows. Let the laser of power P be modulated with index M and the radiation scattered by the water be collected with a receiver of aperture A_r at a distance R from the water surface. For a diffuse backscattering parameter σ (defined earlier and measured experimentally), the average modulated power incident on the detector is, from Eq. (2.16),

$$\Delta P = M [1 - \exp(-2x^2)] P \sigma A_r / 2R^2. \quad (2.56)$$

The assumption is implicit here that the transmission losses through optics and such are the same as those encountered in the experiment. The unmodulated power incident on the detector is

$$P_{DC} = (1-M) [1 - \exp(-2x^2)] P \sigma A_r / R^2. \quad (2.57)$$

This unmodulated radiation does not contribute to the signal but is equivalent to an additional source of background photons and contributes to the noise by degrading D^* since it can be shown that D^* varies as $Q_B^{-1/2}$ in background-limited operation, where Q_B is the background photon flux.¹⁶

It will be recalled that the thermal background power at 300° K, with a 30° field-of-view is $5.5 \times 10^{-4} \text{ W cm}^{-2}$ without a filter and $3.35 \times 10^{-5} \text{ W cm}^{-2}$ with a cooled filter of 0.5 μm bandwidth. Since an additional source of background photons is present, the D^* value should be modified by a factor K given by

$$K = \left\{ \frac{5.5 \times 10^{-4} A_d}{5.5 \times 10^{-4} A_d + [(1-M) [1-\exp(-2x^2)] P \sigma A_r / R^2]} \right\}^{1/2} \quad (2.58a)$$

for operation without a filter and

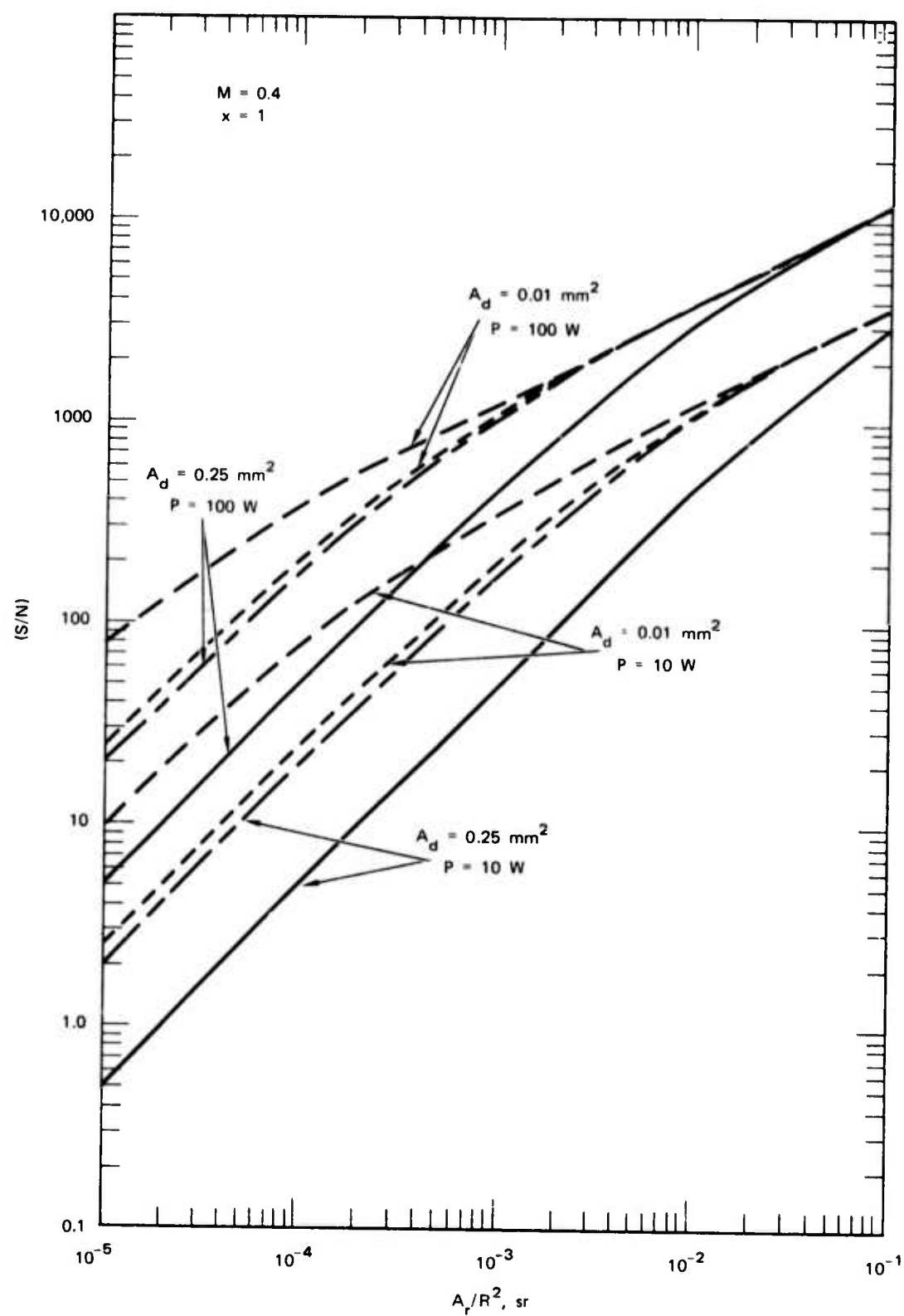
$$K_f = \left\{ \frac{5.5 \times 10^{-4} A_d}{3.35 \times 10^{-5} A_d + [(1-M) [1-\exp(-2x^2)] P \sigma A_r / R^2]} \right\}^{1/2} \quad (2.58b)$$

for operation with a cooled filter of 0.5 μm bandwidth. The advantage of using a cooled filter is evident. The high-frequency response of HgCdTe detectors has been measured and remains essentially flat up to 300-400 MHz, especially when back-bias is used.¹⁵ Thus, operation at about 100 MHz will not be impaired. In other words, D^* will not be degraded from lack of frequency response. Hence Eq. (2.55) may now be written with Eqs. (2.56) and (2.58) as

$$(S/N) = M [1-\exp(-2x^2)] P \sigma A_r D^* K / 2R^2 (A_d \Delta f)^{1/2} \quad (2.59)$$

In Figure 22, the S/N ratio is plotted as a function of the receiver's collection angle. Two laser power levels are shown with a modulation index of 0.4 and two detector sizes. Operation with a cooled filter of 0.5 μm bandwidth at 10.6 μm is also shown. Figure 22 shows that S/N ratios of 100 or more are possible with reasonable laser powers and collection apertures. The advantage of using a cooled filter is once again seen from the figure.

The foregoing analysis considered only direct detection of the laser energy. The NEP in heterodyne detection is considerably lower than in the case of direct detection.¹⁵ Hence, large increases in the S/N ratio can be expected if heterodyne detection is used. This advantage is much less significant at shorter optical wavelengths.



SA-2422-27

FIGURE 22 SIGNAL-TO-NOISE PERFORMANCE OF IR RECEIVER WITH DIFFERENT POWER LEVELS AND DETECTOR SIZES

6. Phase Measurement

The phase difference between the amplified output of the detector and a reference signal corresponding to the modulating signal, which is related to the target range, will be measured by a commercial phase meter (Hewlett-Packard Model 8405A Vector Voltmeter). This instrument is ideally suited for the proposed phase-ranging technique. The major performance specifications of the instrument are as follows: (1) phase resolution of 0.1° in the phase measurement, (2) 90-100 dB dynamic range for the input signals, (3) frequency range of 1-1000 MHz, (4) automatic tuning to follow signals drifting by as much as 15 MHz/s, and (5) possibility of phase measurement performed at a 20 kHz rate.

The movements of the waves are such that the surface is locally stationary for at least a time on the order of 1 m s. Then the 20 kHz measurement rate means that approximately twenty phase measurements are made at the identical range during this period. The S/N of the detector output may be interpreted in the context of phase measurement as equivalent to a vector of length S oriented along a given direction with a vector of length N, whose orientation is random for each measurement, attached to the end of S. The resultant vector is the phasor whose phase difference with respect to a reference phasor is determined by the phase measurement. As n, the number of measurements increases, the resultant of the noise vectors of random orientation will have a length N/\sqrt{n} , until the error in phase given by $N/(\sqrt{n} S)$ becomes comparable to the error in the phase measurement itself. When this limit is reached

$$(N/S\sqrt{n}) \leq \psi \quad (2.60)$$

where ψ is the phase resolution of the measurement in radians. Hence, when n is 20, and $\psi = 0.1^\circ$ of 1.75×10^{-3} radians, $(S/N) \geq (\sqrt{n} \psi)^{-1} = 128$. Thus, for the performance of the phase meter to limit the resolution of the system, a S/N ratio higher than 128 in the detector output is needed. As seen from Figure 22, such S/N ratios are attainable from practical optical systems.

After detailed examination of the instrument operation and consultation with the manufacturer of the voltmeter, the instrument output corresponding to the phase difference was found to have a slow response -- on the order of 30 Hz because of a slow phase-comparison circuit. In effect, the measurements made at a 20 KHz rate are averaged over 30 ms. Thus, if the instrument is used without modification, the response of the total system would be such that wave surface movement faster than 30 ms cannot be faithfully followed by the profilometer. Higher S/N performance would also be expected from the receiver.

The sampling and the IF parts of the instrument do not limit the speed of measurement. Thus, in principle, the possibility exists of modifying or replacing the phase measuring circuit alone so as to increase the frequency response or decrease the measurement time. Several techniques that use the 20 KHz-IF outputs to perform the phase measurement at a faster rate were discussed with the manufacturer. Although they appear promising, their effect on the other desirable qualities of the instrument -- such as the resolution and the dynamic range -- have not been fully investigated and satisfactorily resolved at this time, but they merit further effort.

7. Design Logic for the Profilometer System

From the foregoing discussions, the critical part of the system design is seen to lie in the choice of the optical components. The laser source, the modulation, the detector, and the phase measurement are less demanding and allow considerable freedom of choice. Thus, the optical design should be attempted first.

The intended application of the profilometer provides expected or desirable values of the range, the horizontal (or lateral) resolution, and the maximum wave heights. These determine to a large degree the other parameters of the system. The desired resolution $2m\omega_0$ determines the beam waist radius ω_0 for $m \approx 1$. The transmitting aperture needed at the desired range may now be determined from Figure 20 or Eqs. (2.5) and (2.30). From speckle

considerations the receiving aperture area should be at least 10 times the area of the transmitting aperture. This determines the smallest collection angle. It may have to be enlarged to obtain a S/N ratio adequate for the phase measurement (≈ 130). Figure 22 and Eq. (2.22) enable the choice of the aperture as well as the laser power P , the detector area A_d , and the need for a filter. The smallest aperture compatible with the other factors is chosen because the depth of field is inversely related to the aperture diameter. The focal length f of the receiver system may now be determined by using an f-number of 1.5 - 2 compatible with a 30° field-of-view. From the range R , the focal length f , and the waist diameter $2\omega_0$, the size of the image may now be calculated. From the previously determined value of A_d , the value of N is now available. On the assumption that $x = 1.0$, the depth of field W may now be determined from Figures 17-19 or Eq. (2.27). A more exact value for m may also be obtained now from Eq. (2.31) or Figure 21. These values of W and m lead to the maximum tolerable wave height and the lateral resolution. Comparison of these values with the design goals evaluates the success of the design. Iterative changes of various parameters are possible to obtain more optimum choice. Relaxation of the design goals may also have to be made. A choice of a value for x less than unity will lead to larger depth of field at the expense of S/N ratio. Availability of detectors of larger size will also increase the depth of field. In Table 1, the characteristics of two designs for different ranges, derived according to the above principles, are listed.

D. DISCUSSION AND RECOMMENDATIONS

The laser profilometer system based on $10.6 \mu\text{m}$ (CO_2) lasers has been evaluated following laboratory measurements of the diffusely backscattered laser radiation. The concept and the various components needed to assemble the system have been examined in detail. It was found that a laser profilometer can be assembled mainly from commercially available components. Two specific designs are recommended with the following specifications; (1) a height resolution of 1 mm and a lateral resolution of 2 mm at a range of 3 m and (2) a height resolution of 2 mm and a lateral resolution of 5 mm at a range of 10 m. The former will be applicable in a wind-wave tank and the latter can be

TABLE 1
CHARACTERISTICS OF PROFILOMETER DESIGNS FOR TWO RANGES

Characteristics	Symbol	Unit	Values	
Desired range	R	m	3.0	10.0
Desired lateral resolution	$2m\omega_o$	mm	2.0	5.0
Beam waist radius	ω_o	mm	1.0	2.5
Transmitting aperture	D_t	cm	2.9	3.9
Minimum receiving aperture		cm	9.0	12.0
Minimum collection angle		sr	7×10^{-4}	1.1×10^{-4}
Chosen collection angle		sr	1×10^{-3}	3.5×10^{-4}
Chosen laser power	P	W	10	100
Chosen detector size	A_d	mm ²	0.25	0.25
Chosen receiving aperture	D_r	cm	10.7	21.0
Expected S/N ratio	(S/N)		180	170
Filter needed			yes	no
f-Number	\mathcal{F}		2	2
Focal length	f	cm	21.4	42.0
Size of image of beam waist	I_o	mm	0.15	0.215
N	N		3.3	2.3
x	x		1.0	1.0
Depth of field	W	cm	24.6	62.4
Modified lateral resolution	$2m\omega_o$	mm	2.2	5.0
Modulation frequency	ν	MHz	100	100
Height resolution		mm	~1.0	~2.0

used from a tower in the ocean for measurement of wave heights to great accuracy and at high data rates. It is recommended that the technique be implemented at first in a wave tank, which is instrumented for comparison with wave-staff measurements, and subsequently from a tower.

The method is both an active technique and a remote noncontacting technique. Thus, the availability of the sun or daylight does not limit as some other techniques do. In addition, the presence of surfactants or capillarity will have no effect on the measurement. Because of its remote nature, mechanical isolation can be achieved in an environment when several other interfering measurements are being made concurrently.

An interesting and intriguing use of the profilometer off a tower would be to sense small changes in mean height of the surface of the ocean accompanying the passage of internal waves. However, this application will depend heavily on the long-term stability (absence of long-term drift) of the total system. It is infeasible to evaluate the stability of the profilometer over a few hours (comparable to the period of internal waves) before the various subsystems are assembled into an interacting unit.

Extension of the technique to a scanning mode and to longer ranges is desirable. Operation of the profilometer in a scanning mode, generating wave-height data long a line instead of a point, would greatly increase the potential of the instrument. This would require much greater data rates than are at present contemplated. The most important limitation is the time required to produce phase information of adequate S/N from a spot diameter. With the current concept entailing direct detection of the scattered laser power and the use of a commercial phase-detecting instrument, the feasibility of scanning is marginal. With the higher S/N ratio available with heterodyne detection and faster techniques of phase detection, line-scanning becomes attractive.

To extend the range of the profilometer, the central design problem is to achieve as small a waist size and as large a depth of field as possible. At a given range, the waist size demands a large aperture and the depth of field requires a small aperture.

For a given wavelength, the smallest aperture is determined by S/N ratio or speckle size. If heterodyne detection were used at $10.6\text{ }\mu\text{m}$, the S/N would be improved by several decades, but the major advantage would be in the reduction of laser power, the receiving aperture being limited by speckle size. Improvement in the resolution and transmitting and receiving apertures would result if shorter optical wavelengths were used. In the $2\text{--}5\text{ }\mu\text{m}$ range, the skin depths in water are acceptably small and the transmittance of the atmosphere is sufficiently large. The required modulation of the laser may be achieved with the same electrooptic materials with lower peak voltages. Heterodyne detection becomes less advantageous at shorter wavelengths. With the direct detection, background level will increase for two reasons: the Rayleigh scattering cross-section increases as λ^{-4} , and the solar irradiance at $3\text{ }\mu\text{m}$ is approximately two decades higher than at $10\text{ }\mu\text{m}$. These are somewhat compensated by the smaller thermal radiation. More importantly, lasers in the $2\text{--}5\text{ }\mu\text{m}$ range of adequate powers ($1\text{--}10\text{ W}$) and reliability are still under active development at this time. Detectors sensitive to $2\text{--}5\text{ }\mu\text{m}$ with frequency response in the $100\text{--}400\text{ MHz}$ range are also under development. The possibility of using shorter wavelengths becomes attractive when the latter two components meet the requirements.

These extensions of the capabilities of the profilometer are expected to be examined in our continuing work.

III THEORY OF SPECKLE PATTERNS

A. SUMMARY OF RESULTS

As mentioned in the Introduction, this study was motivated by an interest in remote optical methods for determining statistical characteristics of ocean waves. At the outset, considerable disagreement was evident in the literature concerning the theoretical predictions of coherence effects caused when temporally coherent light is scattered by a diffuse surface. Notes on discussions between principals early in the project period on the apparent conflicts in the theories appear as Appendix A. A significant effort was thus expended on strengthening and extending the general theory and reconciling apparent discrepancies. The specific application of this general theory to ocean surfaces has begun but has not yet been fully developed. Work on this application is continuing and the results are expected to be included in a subsequent report.

After reviewing the major contributions relevant to our present work,^{10, 17-19}, we conclude that, aside from the minor points, all of the theoretical predictions are correct. The apparent discrepancies have resulted from improper interpretation of results rather than from improper development of the theory as described in Appendix B. Specifically, we conclude that the work of Goldfischer¹⁸, whose model of the scattering surface carries with it the implication that the spatial coherence of the field at the scattering surface behaves like a δ -function, is correct for the model used and is entirely consistent with the early work of Goodman¹⁷. Goodman extended¹⁶ his own theory to account for finite spatial coherence of the fields at the scattering surface, which laid the groundwork for relating surface characteristics to measurements in the receiver plane. Crane's claim that the power spectral density in the receiver plane contains information about surface roughness is correct, but his specific result¹⁹ (Eq. 39) cannot be applied to truly rough surfaces where the rms

surface roughness σ is greater than the wavelength λ .⁸ Goodman's extension of Crane's general approach (see Appendix B) can be applied to truly rough surfaces and is consistent with previous results.

The general speckle theory is extended in this report to include effects related to the practical matter of using finite apertures to make measurements. Specifically, the aperture required to extract information about surface characteristics from a measurement of power spectral density must be large enough to resolve the fine details of the surface. Under certain conditions stated in the text, the ensemble average intensity distribution in one plane is related through a Fourier transform to the ensemble average spatial coherence in the other plane. This means that a measurement of the spatial coherence in the receiver plane can yield information only about the distribution of average intensity in the target plane. Moreover, a measurement of average intensity in the receiver plane, in principle, can yield information about surface characteristics. However, as a practical matter, it appears that a wide class of different surfaces whose surface height autocorrelation functions behave similarly near zero displacement may yield almost identical average intensity distributions in the receiver plane. This matter is the subject of continuing investigation. Furthermore, since the average intensity distribution is not sensitive to temporal coherence, in principle, a nontemporally coherent light source, such as filtered white light, could be used to reveal the same information as laser light.

An expression is derived in the text which relates surface spatial coherence (and therefore receiver intensity distribution) to rms surface roughness σ and surface height autocorrelation function ρ for the case where the surface height distribution is Gaussian. This condition is approximately satisfied for ocean waves.²⁰ These surface characteristics are in turn related to the power spectral density of the wave heights. The effect of perturbations in a sample one-dimensional wave height power spectral density were superficially investigated, but no firm conclusions were reached. The physical significance of wave height, slope, and curvature power spectral densities and the effect of perturbations in more realistic two-dimensional spectra are the subjects of continuing investigation.

Figure 23 is included here as a convenient summary of relationships which exist between physical quantities (indicated in boxes) in the mean target plane (subscript τ) and those in the receiver plane (subscript ρ). Deterministic quantities are found within the dashed rectangle; everything outside the dashed rectangle, with the exception of normalization constants, are ensemble average quantities. Note that all quantities above the broken line belong to the mean target plane and all quantities below this line belong to the receiver plane. Circles are used to indicate operations.

B. GENERAL THEORY

1. Two Equivalent Forms of the Huygens-Fresnel Principle

The Huygens-Fresnel principle can be cast in two different forms. One form, used by Goodman¹⁰, relates the field in the speckle pattern to the field at a reference plane immediately in front of the scattering surface. The other form, used by Crane¹⁹, relates the field in the speckle pattern to the field at the scattering surface itself. These two forms are stated below, and the relationship between the field at the reference plane and the field at the scattering surface is developed.

Figure 24 shows the geometry and coordinate systems that are used. The (u, v) plane (the v axis, not shown in the figure, is directed into the page) is taken to be the median plane of the scattering surface while the (x, y) plane (the y axis, not shown in the figure, is directed into the page) is parallel to the (u, v) plane at a distance h . The speckle pattern exists in this (x, y) plane.

The speckle pattern field $E(x, y)$ can be related to the field $E_s(u, v)$ on the scattering surface by the Huygens-Fresnel principle:

$$E(x, y) = \frac{1}{j\lambda} \iint_{-\infty}^{\infty} \frac{E_s(u, v) e^{jkR} \cos \varphi \cos [\vec{z}_0, \vec{n}(u, v)] dS}{R} \quad (3.1)$$

with

$$R = |\vec{r}_0 - \vec{r}| \quad (3.2)$$

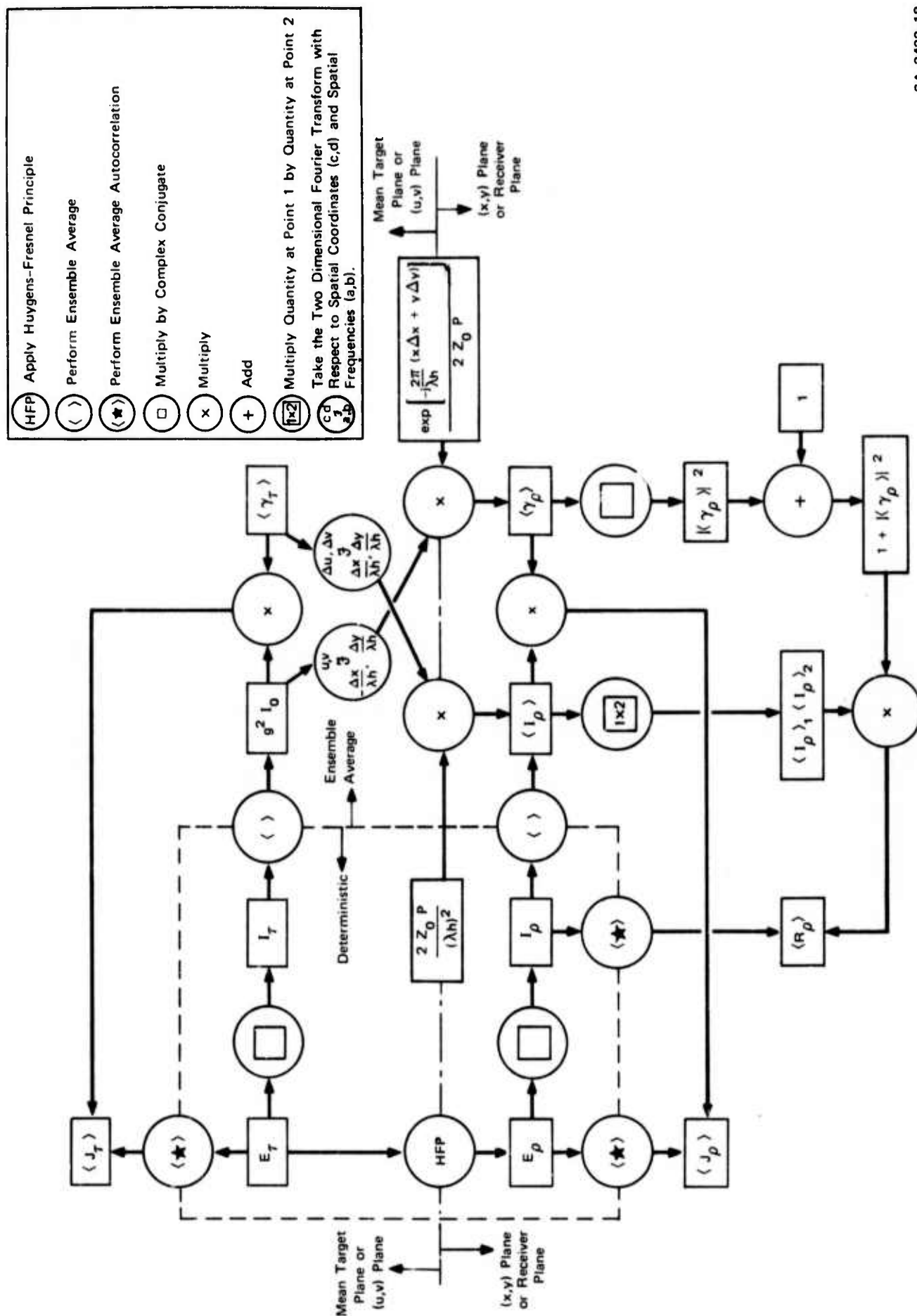
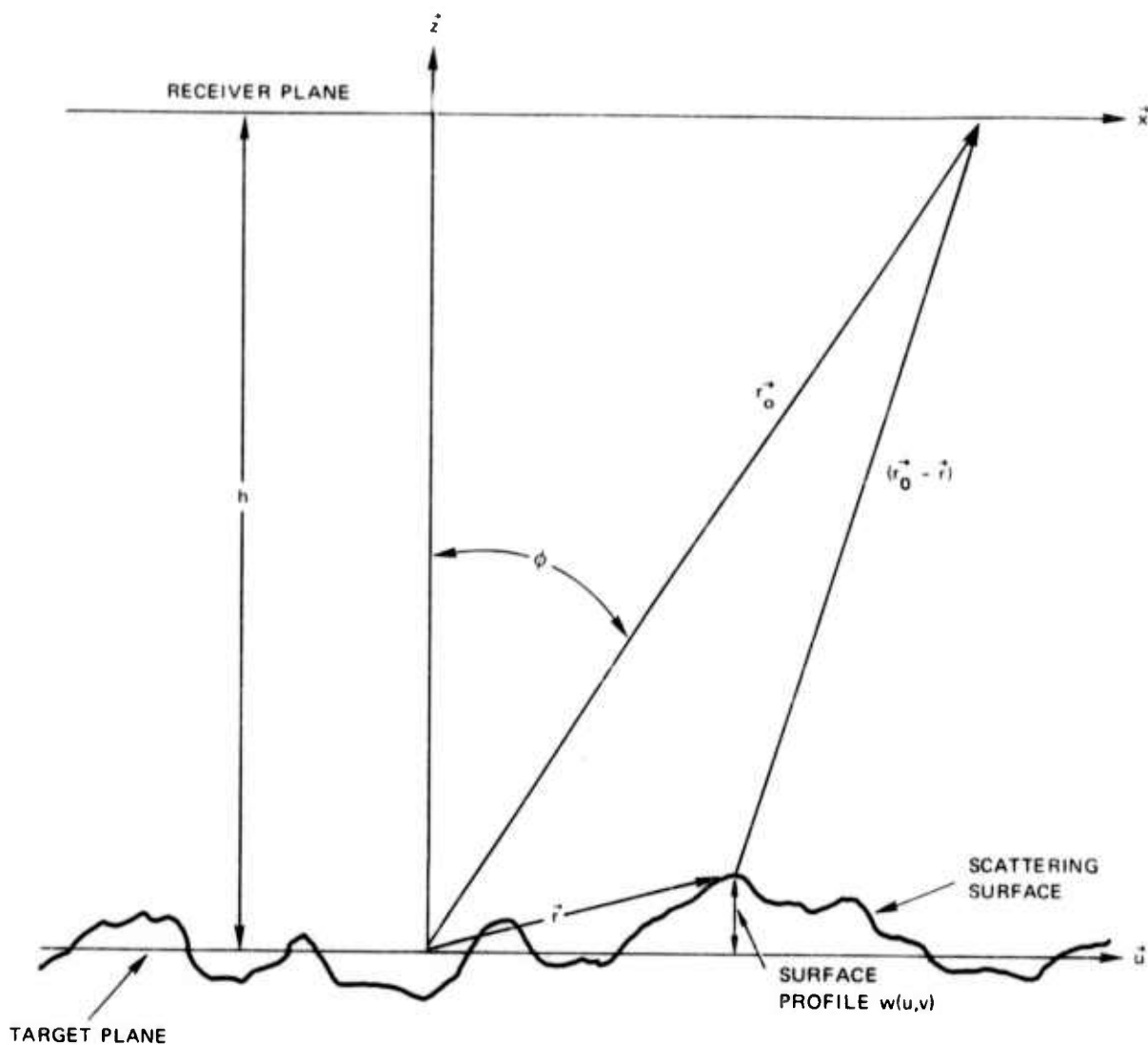


FIGURE 23 SUMMARY OF RELATIONSHIPS BETWEEN PHYSICAL QUANTITIES IN THE TARGET AND RECEIVER PLANE

SA-2422-18



SA-2422-11

FIGURE 24 GEOMETRY AND COORDINATE SYSTEMS USED IN THE HUYGENS-FRESNEL PRINCIPLE

Here, \hat{z}_0 is taken to be a unit vector in the z direction, and $\hat{n}(u, v)$ is taken to be a unit vector directed normal to the surface. The symbol dS is used for the elemental area in the (u, v) plane, k has the value $2\pi/\lambda$, and λ is the wavelength of the reflected radiation. Refer to Figure 24 for the definition of \hat{r}_0 , \hat{r} , $w(u, v)$, and ϕ .

Alternatively, the Huygens-Fresnel principle may be used, as Goodman¹⁰ did, to cast the problem in a slightly different form. In this form, the field in the receiver plane $E(x, y)$ is not related to the field $E_s(u, v)$ on the scattering surface but rather to the field $E_p(u, v)$ in a reference plane near the scattering surface. Here the surface median plane, i.e., the (u, v) plane is, chosen for the reference plane.

$$E(x, y) = \frac{1}{j\lambda} \iint_{-\infty}^{\infty} \frac{E_p(u, v) e^{jkR'} \cos \varphi}{R'} dS \quad (3.3)$$

with

$$R' = |\vec{r}_0 - \vec{r}'|, \quad (3.4)$$

and \vec{r}' lies entirely in the (u, v) plane; that is, \vec{r}' is the value of \vec{r} for $w(u, v) = 0$.

Since Eqs. (3.1) and (3.3) are alternative valid expressions for the field $E(x, y)$, they may be combined to obtain a relationship between the fields $E_p(u, v)$ and $E_s(u, v)$.

$$E_p(u, v) = \left(\frac{R'}{R}\right) e^{jk(R-R')} \cos \left[\vec{z}_0, \vec{n}(u, v) \right] E_s(u, v). \quad (3.5)$$

While the relationship expressed by Eq. (3.5) is valid when used in the Huygens-Fresnel principle to calculate quantities of interest in the receiver plane, it clearly fails to describe accurately the propagation of the fields from the surface to the reference (u, v) plane. Thus, the relationship should not be used when the ultimate quantity of interest is in the (u, v) plane. On the other hand, the relationship may be used to calculate a quantity in the (u, v) plane as an intermediate step toward an expression for a physical quantity in the (x, y) or receiver plane.

Let us next obtain expressions for the field on the surface and the average intensity in the (u, v) plane in terms of an incident wave E_i . For a plane uniform incident wave whose direction of propagation makes an angle β with the z axis and is perpendicular to the v axis

$$E_i(u, z) = E_0 e^{-jk[z \cos \beta + u \sin \beta]}, \quad (3.6)$$

and the field $E_s(u, v)$ on the reflecting surface after reflection is given by

$$E_s(u, v) = \eta(u, v) E_0 e^{-jk[w(u, v) \cos \beta + u \sin \beta]} \quad (3.7)$$

where E_0 is the amplitude of the incident wave and

$$\eta(u, v) = |\eta(u, v)| e^{-j\pi} = -|\eta(u, v)| \quad (3.8)$$

is the Fresnel amplitude reflectance of the reflecting surface. By the use of Eqs. (3.5) and (3.7), the average intensity can be written as

$$\langle I_p(u, v) \rangle \triangleq \langle E_p(u, v) E_p^*(u, v) \rangle = \langle |\eta(u, v)|^2 E_0^2 \cos^2 [\vec{z}_0, \vec{n}(u, v)] \rangle \quad (3.9)$$

where the approximation $(R'/R) \approx 1$ is made. For small incident angle β and small surface slopes, Eq. (3.9) becomes

$$\langle I_p(u, v) \rangle \approx |\eta_\beta|^2 E_0^2 \triangleq I_0. \quad (3.10)$$

Here, η_β is taken to be the Fresnel amplitude reflectance for the angle β .

2. Ensemble Definitions and Relationships

The Huygens-Fresnel principle in its form in Eq. (3.3) will be used to write formal expressions for several quantities of interest. In general, because of mathematical complexity, a computer is required to evaluate these expressions. However, later approximations to these expressions will be made which, in some cases, will lead to integrals that can be performed analytically. In the following, the subscript ρ will be used to denote quantities in the receiver (x, y) plane, and the subscript τ will be used to denote quantities in the target (u, v) plane when the functional arguments are omitted.

a. Ensemble Average Mutual Intensity

$$\langle J_\rho \rangle \equiv \langle J(x_1, y_1; x_2, y_2) \rangle \triangleq \langle E(x_1, y_1) E^*(x_2, y_2) \rangle. \quad (3.11)$$

From Eq. (3.3), we may write

$$\langle J_\rho \rangle = (\lambda h)^{-2} \left\langle \int_{-\infty}^{\infty} \int_{-\infty}^{\infty} \int_{-\infty}^{\infty} \int_{-\infty}^{\infty} E_p(u_1, v_1) E_p^*(u_2, v_2) \cos \varphi_1 \cos \varphi_2 e^{jk(R_{11} - R_{22})} du_1 dv_1 du_2 dv_2 \right\rangle \quad (3.12)$$

or

$$\langle J_\rho \rangle = (\lambda h)^{-2} \int_{-\infty}^{\infty} \int_{-\infty}^{\infty} \int_{-\infty}^{\infty} \int_{-\infty}^{\infty} \langle E_p(u_1, v_1) E_p^*(u_2, v_2) \rangle \cos \varphi_1 \cos \varphi_2 e^{jk(R_{11} - R_{22})} du_1 dv_1 du_2 dv_2 \quad (3.13)$$

where we have used the approximation $R' \approx h$ in the denominator of Eq. (3.3) and R_{ij} is defined as

$$R_{ij} \triangleq \left\{ [x_i - u_j]^2 + [y_i - v_j]^2 + [h - w(u_j, v_j)]^2 \right\}^{1/2} . \quad (3.14)$$

The quantity in ensemble brackets $\langle \rangle$ in the integrand will be recognized as the mutual intensity $\langle J_T \rangle$ in the target plane so that Eq. (3.13) may be restated as

$$\langle J_\rho \rangle = (\lambda h)^{-2} \iiint_{-\infty}^{\infty} \langle J_T \rangle \cos \varphi_1 \cos \varphi_2 e^{jk(R_{11} - R_{22})} du_1 dv_1 du_2 dv_2 . \quad (3.15)$$

b. Ensemble Average Intensity

$$\langle I_\rho \rangle \equiv \langle I(x, y) \rangle \triangleq \langle E(x, y) E^*(x, y) \rangle . \quad (3.16)$$

If we proceed as above, the result is

$$\langle I_\rho \rangle = (\lambda h)^{-2} \iiint_{-\infty}^{\infty} \langle J_T \rangle \cos \varphi_1 \cos \varphi_2 e^{jk(R_{11} - R_{12})} du_1 dv_1 du_2 dv_2 . \quad (3.17)$$

c. Ensemble Average Autocorrelation Function

$$\langle R_\rho \rangle \equiv \langle R(x_1, y_1; x_2, y_2) \rangle \triangleq \langle I(x_1, y_1) I(x_2, y_2) \rangle . \quad (3.18)$$

We next make use of the relationship* (valid only for Gaussian fields $E_p(x, y)$)

$$\langle R_p \rangle = \langle I(x_1, y_1) \rangle \langle I(x_1 - \Delta x, y_1 - \Delta y) \rangle \left[1 + |\langle \gamma_p(\Delta x, \Delta y) \rangle|^2 \right] \quad (3.19)$$

where $\langle \gamma_p(\Delta x, \Delta y) \rangle$ is the normalized spatial coherence function given by

$$\langle \gamma_p(\Delta x, \Delta y) \rangle \triangleq \frac{\langle E(x_1, y_1) E^*(x_1 - \Delta x, y_1 - \Delta y) \rangle}{\left[\langle I(x_1, y_1) \rangle \langle I(x_1 - \Delta x, y_1 - \Delta y) \rangle \right]^{1/2}} \quad (3.20)$$

with

$$x_2 = x_1 - \Delta x \text{ and } y_2 = y_1 - \Delta y .$$

d. Ensemble Average Space Average Autocorrelation Function over Finite Aperture

$$\langle R'_p \rangle \triangleq A^{-1} \iint_{-\infty}^{\infty} f(x_1, y_1) f(x_1 - \Delta x, y_1 - \Delta y) \langle R_p \rangle dx_1 dy_1 \quad (3.21)$$

with

$$A = \iint_{-\infty}^{\infty} f(x_1, y_1) dx_1 dy_1 \quad (3.22)$$

*See Appendix C for a proof of this relationship.

where $f(x, y)$ is an aperture function defining the finite aperture in the (x, y) plane over which the average intensity is known. This aperture function has value unity within the aperture and is zero outside the aperture. Using Eqs. (3.19) and (3.21) yields

$$\begin{aligned} \langle R'_\rho \rangle &= A^{-1} \left[1 + |\langle \gamma_\rho(\Delta x, \Delta y) \rangle|^2 \right] \bullet \\ &\bullet \iint_{-\infty}^{\infty} f(x_1, y_1) f(x_1 - \Delta x, y_1 - \Delta y) \langle I(x_1, y_1) \rangle \langle I(x_1 - \Delta x, y_1 - \Delta y) \rangle dx_1 dy_1. \end{aligned} \quad (3.23)$$

e. Ensemble Average Power Spectral Density over Finite Aperture

$$\langle S_\rho \rangle \equiv \langle S(\alpha, \Omega) \rangle \triangleq \frac{\langle |G(\alpha, \Omega)|^2 \rangle}{A} \quad (3.24)$$

with

$$G(\alpha, \Omega) \triangleq \iint_{-\infty}^{\infty} f(x, y) I(x, y) e^{-j2\pi(x\alpha + y\Omega)} dx dy \quad (3.25)$$

where (α, Ω) are spatial frequencies in the (x, y) plane. Equation (3.24) can be expanded with the help of Eq. (3.25)

$$\begin{aligned} \langle S_\rho \rangle &= A^{-1} \left\{ \iiint_{-\infty}^{\infty} f(x_1, y_1) f(x_1 - \Delta x, y_1 - \Delta y) \bullet \right. \\ &\bullet \langle I(x_1, y_1) I(x_1 - \Delta x, y_1 - \Delta y) \rangle e^{-j2\pi(\Delta x\alpha + \Delta y\Omega)} dx_1 dy_1 d\Delta x d\Delta y \left. \right\} \end{aligned} \quad (3.26)$$

where the transformation $x_2 = x_1 - \Delta x$ and $y_2 = y_1 - \Delta y$ has been used. Finally, with the help of Eqs. (3.18) and (3.21),

$$\langle S_\rho \rangle = \iint_{-\infty}^{\infty} \langle R'_\rho \rangle e^{-j2\pi(\Delta x \alpha + \Delta y \Omega)} d\Delta x d\Delta y . \quad (3.27)$$

From Eq. (3.27), it is clear that $\langle S_\rho \rangle$ and $\langle R'_\rho \rangle$ are Fourier transform pairs and thus Eq. (3.27) is a statement of the Wiener-Khintchin theorem.

In summary, it should be mentioned that even though the ensemble relationships in Eqs. (3.15), (3.17), (3.19), (3.23), and (3.27) can be evaluated very accurately by numerical techniques, their validity is ultimately restricted by the conditions of validity of the Huygens-Fresnel principle in its form in Eq. (3.3).

C. FURTHER APPROXIMATIONS TO THE GENERAL THEORY

The approximations used in this section are commonly used in diffraction theory and do not necessarily imply great loss in accuracy. In fact, the expressions stated in this section are applicable to a large class of practical problems. Nevertheless, there are some practical problems for which these approximations could lead to serious inaccuracies; thus, the conditions of validity will have to be examined carefully before the expressions developed here can be applied. However, it will be convenient to defer the discussion of accuracy and conditions of validity until a later section where specific numerical calculations are presented.

First, we restrict our considerations to small angles φ . In this case, $\cos \varphi$ in Eq. (3.1) and (3.3) may be replaced by unity with little loss of accuracy. If the surface slopes are small and the angle β that the incident plane wave makes with the z -axis is small, $\cos [\vec{z}_0, \vec{n}(u, v)]$ can be replaced by unity and the Fresnel amplitude reflectance $\eta(u, v)$ can be taken to be a constant η_β independent of (u, v) .

Next we expand R and R' , defined respectively by Eq. (3.2) and (3.4), in binomial series.

$$R = h + \frac{hB}{2} \left(1 - \frac{B}{4}\right) - w(u, v) \left[1 - \frac{B}{2} \left(1 - \frac{3B}{4}\right)\right] + \frac{w^2(u, v) B}{2h} \left[1 - \frac{3B}{2}\right] + \dots \quad (3.28)$$

and

$$R' = h + \frac{hB}{2} \left(1 - \frac{B}{4}\right) + \dots \quad (3.29)$$

where the notation

$$B \triangleq \frac{(x - u)^2 + (y - v)^2}{h^2} \quad (3.30)$$

has been used. To simplify calculations using the Huygens-Fresnel principle, we shall approximate the infinite series of Eqs. (3.28) and (3.29) with a finite number of terms. The resulting loss of accuracy will be discussed in a later section. For our current purpose, we choose to drop all terms in the series second order or higher in B or $w(u, v)$ and first order or higher in $B w(u, v)$. Loosely speaking, this imposes the following conditions:

- $\frac{w(u, v)}{h} \ll 1$ surface roughness not too large
- $\frac{u_{\max} v_{\max}}{h^2} \ll 1$ illuminated spot size not too large
- $\frac{x_{\max} y_{\max}}{h^2} \ll 1$ angle φ not too large.

With these approximations made, the two forms of the Huygens-Fresnel principle become

$$E(x, y) \approx \frac{1}{j\lambda h} \iint_{-\infty}^{\infty} E_s(u, v) e^{jk \left[h - w(u, v) + \frac{(x-u)^2 + (y-v)^2}{2h} \right]} ds \quad (3.31)$$

and

$$E(x, y) \approx \frac{1}{j\lambda h} \iint_{-\infty}^{\infty} E_p(u, v) e^{jk \left[h + \frac{(x-u)^2 + (y-v)^2}{2h} \right]} ds \quad (3.32)$$

from which

$$E_p(u, v) = e^{-jk w(u, v)} E_s(u, v) \quad (3.33)$$

results. By the use of Eqs. (3.7) and (3.10) in Eq. (3.33), the field in the (u, v) plane is given by

$$E_p(u, v) = j\sqrt{I_0} e^{-jk[w(u, v)(1 + \cos \beta) + u \sin \beta]} \quad (3.34)$$

Here it should be emphasized that even though Eq. (3.33) indicates that the mathematical field $E_p(u, v)$ on the (u, v) plane is related to the actual field $E_s(u, v)$ on the scattering surface through the simple propagator $\exp[-jk w(u, v)]$, the relationship obviously incorrectly describes field propagation between the two surfaces. However, Eq. (3.33) can be used to calculate quantities in the (x, y) plane provided the conditions of validity for the Huygens-Fresnel principle are satisfied.

At this point, we wish to develop explicit expressions in the (x, y) plane for the following ensemble average quantities: power spectral density $\langle S(\alpha, \Omega) \rangle$, mutual intensity $\langle J_{\rho} \rangle$, and intensity $\langle I_{\rho} \rangle$. To simplify the mathematics, we first develop expressions in one-dimension only and then generalize to two-dimensions. We define a deterministic aperture function $g(u, v)$ belonging to the field in the (u, v) plane. For example, if a rectangle L by M of the surface is illuminated, the aperture function has the value $\text{rect}\left(\frac{u}{L}\right) \cdot \text{rect}\left(\frac{v}{M}\right)$; or if the intensity distribution incident on the scattering surface is Gaussian having radius w_0 and peak intensity I_0 , the aperture function has the value $\exp\left\{-\frac{u^2 + v^2}{2w_0^2}\right\}$.

Thus, Eq. (3.34) now takes the form

$$E_p(u, v) = j\sqrt{I_0} g(u, v) \exp\{-jk[w(u, v)(1 + \cos\beta) + u \sin\beta]\} \quad (3.35)$$

1. Ensemble Average Intensity and Mutual Intensity

With the Huygens-Fresnel principle in its form in Eq. (3.32), the one-dimensional ensemble average mutual intensity in the (x, y) plane can be written as

$$\langle J_{\rho} \rangle = \left\langle (\lambda h)^{-2} \iint_{-\infty}^{\infty} E_p(u_1) E_p^*(u_2) e^{j\frac{2\pi}{\lambda h} \left[\frac{(x_1 - u_1)^2 + (y_1 - v_1)^2}{2} \right]} du_1 dv_1 \right\rangle \quad (3.36)$$

Let $u_1 = u_0 + \frac{\Delta u}{2}$ and $u_2 = u_0 - \frac{\Delta u}{2}$ so that $u_1 - u_2 = \Delta u$

$$\langle J_{\rho} \rangle = (\lambda h)^{-2} \iint_{-\infty}^{\infty} \left\langle E_p\left(u_0 + \frac{\Delta u}{2}\right) E_p^*\left(u_0 - \frac{\Delta u}{2}\right) \right\rangle e^{j2\pi\beta} du_0 d\Delta u \quad (3.37)$$

with

$$\beta = \frac{1}{\lambda h} \left[\left(\frac{x_1^2 - x_2^2}{2} \right) + u_0 (x_2 - x_1 + \Delta u) - \Delta u \left(\frac{x_2 + x_1}{2} \right) \right] . \quad (3.38)$$

The quantity in ensemble brackets in Eq. (3.37) is the mutual intensity in the (u, v) plane and with the help of Eq. (3.35) can be expressed as

$$\langle J_T \rangle = I_0 g \left(u_0 + \frac{\Delta u}{2} \right) g \left(u_0 - \frac{\Delta u}{2} \right) \langle \gamma_T(\Delta u) \rangle \quad (3.39)$$

with

$$\langle \gamma_T(\Delta u) \rangle = \left\langle e^{-jk \left[\left\{ w \left(u_0 + \frac{\Delta u}{2} \right) - w \left(u_0 - \frac{\Delta u}{2} \right) \right\} (1 + \cos \beta) + \Delta u \sin \beta \right]} \right\rangle . \quad (3.40)$$

We now note that, for conditions of practical interest, $\langle \gamma_T(\Delta u) \rangle$ in Eq. (3.39) becomes vanishingly small as Δu increases from zero to a value very much smaller than the aperture size. In this case, Eq. (3.39) may be approximated by

$$\langle J_T \rangle = I_0 [g(u_0)]^2 \langle \gamma_T(\Delta u) \rangle , \quad (3.41)$$

and Eq. (3.37) becomes

$$\begin{aligned} \langle J_\rho \rangle = & \frac{I_0}{(\lambda h)^2} e^{j \frac{2\pi}{\lambda h} \left(\frac{x_1^2 - x_2^2}{2} \right)} \int_{-\infty}^{\infty} \langle \gamma_\tau(\Delta u) \rangle e^{-j \frac{2\pi}{\lambda h} \left(\frac{x_2 + x_1}{2} \right) \Delta u} \\ & \int_{-\infty}^{\infty} [g(u_0)]^2 e^{j \frac{2\pi}{\lambda h} (x_2 - x_1 + \Delta u) u_0} du_0 d\Delta u . \end{aligned} \quad (3.42)$$

Now let $x_2 = x_0 + \frac{\Delta x}{2}$ and $x_1 = x_0 - \frac{\Delta x}{2}$ so that Eq. (3.42) becomes

$$\begin{aligned} \langle J_\rho \rangle = & \frac{I_0}{(\lambda h)^2} e^{-j \frac{2\pi x_0 \Delta x}{\lambda h}} \left[\int_{-\infty}^{\infty} \langle \gamma_\tau(\Delta u) \rangle e^{-j \frac{2\pi x_0 \Delta u}{h}} \right] \cdot \\ & \left[\int_{-\infty}^{\infty} [g(u_0)]^2 e^{j \frac{2\pi \Delta x u_0}{\lambda h}} du_0 \right] \end{aligned} \quad (3.43)$$

where the factor $e^{j \frac{2\pi u_0 \Delta u}{\lambda h}}$ has been approximated by unity. The condition of validity for this approximation is given by

$$h > \frac{8 u_{0\max} l_c}{\lambda} \quad (3.44)$$

where l_c , the coherence distance of the fields, is the smallest value of Δu for which $\langle \gamma_\tau(\Delta u) \rangle$ has negligible value.

Equation (3.42) now may be written as

$$\langle J_\rho \rangle = \frac{I_o}{(\lambda h)^2} e^{-j \frac{2\pi x_o \Delta x}{\lambda h}} \mathcal{F}_{\frac{x_o}{\lambda h}}^{\Delta u} \left\{ \langle \gamma_T(\Delta u) \rangle \right\} \cdot \mathcal{F}_{-\frac{\Delta x}{\lambda h}}^{u_o} \left\{ [g(u_o)]^2 \right\} \quad (3.45)$$

where the symbol \mathcal{F}_a^b has been used to indicate a Fourier transform and a and b explicitly indicate the spatial frequency and variable of integration respectively.

The interpretation of Eq. (3.45) is best revealed by evaluating $\langle J_\rho \rangle$ for $\Delta x = 0$.

$$\left. \langle J_\rho \rangle \right|_{\Delta x=0} \equiv \langle I_\rho \rangle = \frac{I_o}{(\lambda h)^2} \int_{-\infty}^{\infty} [g(u_o)]^2 du_o \cdot \mathcal{F}_{\frac{x_o}{\lambda h}}^{\Delta u} \left\{ \langle \gamma_T(\Delta u) \rangle \right\} \quad (3.46)$$

The total power P illuminating the (u, v) plane is given by

$$P = \frac{I_o}{2z_o} \int_{-\infty}^{\infty} [g(u_o)]^2 du_o \quad (3.47)$$

where $z_0 = 120 \pi \Omega$ is the impedance of free space. Thus, Eq. (3.46) may be written

$$\langle I_\rho \rangle = \frac{2z_0 P}{(\lambda h)^2} \cdot \mathcal{F}_{\frac{x_0}{\lambda h}}^{\Delta u} \left\{ \langle \gamma_\tau(\Delta u) \rangle \right\}, \quad (3.48)$$

and Eq. (3.45) may be written

$$\langle J_\rho \rangle = \frac{I_0 \langle I_\rho \rangle}{2z_0 P} e^{-j \frac{2\pi x_0 \Delta x}{\lambda h}} \cdot \mathcal{F}_{-\frac{\Delta x}{\lambda h}}^{u_0} \left\{ [g(u_0)]^2 \right\}. \quad (3.49)$$

Finally, the normalized spatial coherence in the (x, y) plane is given by

$$\langle \gamma_\rho(\Delta x) \rangle = \frac{I_0}{2z_0 P} e^{-j \frac{2\pi x_0 \Delta x}{\lambda h}} \cdot \mathcal{F}_{-\frac{\Delta x}{\lambda h}}^{u_0} \left\{ [g(u_0)]^2 \right\}. \quad (3.50)$$

We now express the important results of this section in two dimensional form.

$$\langle I(x, y) \rangle = \frac{2z_0 P}{(\lambda h)^2} \cdot \mathcal{F}_{\frac{x}{\lambda h}, \frac{y}{\lambda h}}^{\Delta u, \Delta v} \left\{ \langle \gamma_\tau(\Delta u, \Delta v) \rangle \right\} \quad (3.51)$$

$$\langle \gamma_p(\Delta x, \Delta y) \rangle = \frac{I_o}{2z_o P} e^{-j 2\pi \left(\frac{x\Delta x + y\Delta y}{\lambda h} \right)} \mathcal{F}_{\frac{\Delta x}{\lambda h}, \frac{\Delta y}{\lambda h}}^{u, v} \left\{ [g(u, v)]^2 \right\}$$

(3.52)

The importance of Eqs. (3.51) and (3.52) can be emphasized by expressing the relationships in words. Equation (3.51) states that the spatial distribution of the ensemble average intensity in the (x, y) plane is proportional to the Fourier transform of the ensemble average normalized spatial coherence of the field in the (u, v) plane. In other words, if the character of the surface is such that the spatial coherence of the field is nearly destroyed, the radiation will be scattered over wide angles. On the other hand, if the character of the surface is such that the field is correlated over significant distances, the radiation will be scattered into a narrow distribution around the specular direction. In a later section, we shall show how the spatial coherence can be related to surface characteristics.

Equation (3.52) expresses the fact that the ensemble average normalized spatial coherence in the (x, y) plane is proportional to the Fourier transform of the normalized average intensity distribution in the (u, v) plane. This can be considered as the ensemble equivalent to the Van Cittert-Zernike theorem for spatial coherence. It is clear from Eq. (3.52) that a measurement of spatial coherence in the receiver plane would reveal nothing about the surface characteristics, but rather it would yield information about the distribution of average intensity in the target plane.

Finally, it is worth mentioning the symmetry of the two relationships in Eqs. (3.51) and (3.52). They both express the fact that the spatial coherence in one plane is related to the intensity distribution in the other plane through a Fourier transform.

2. Ensemble Average Power Spectral Density for Finite Aperture

The one-dimensional power spectral density is given by

$$\langle S(\alpha) \rangle = \int_{-\infty}^{\infty} \langle R'(\Delta x) \rangle e^{-j 2\pi \alpha \Delta x} d\Delta x . \quad (3.53)$$

Using Eq. (3.23) in Eq. (3.53) yields

$$\begin{aligned} \langle S(\alpha) \rangle &= A^{-1} \iint_{-\infty}^{\infty} \left[1 + |\langle \gamma_p(\Delta x) \rangle|^2 \right] f(x) f(x - \Delta x) \\ &\quad \langle I(x) \rangle \langle I(x - \Delta x) \rangle e^{-j 2\pi \alpha \Delta x} dx d\Delta x . \end{aligned} \quad (3.53)$$

For convenience, we separate Eq. (3.54) into two terms defined by

$$\langle S(\alpha) \rangle_0 \triangleq A^{-1} \iint_{-\infty}^{\infty} f(x) \langle I(x) \rangle f(x - \Delta x) \langle I(x - \Delta x) \rangle e^{-j 2\pi \alpha \Delta x} dx d\Delta x \quad (3.55)$$

and

$$\begin{aligned} \langle S(\alpha) \rangle_1 &\triangleq A^{-1} \iint_{-\infty}^{\infty} |\langle \gamma_p(\Delta x) \rangle|^2 f(x) \langle I(x) \rangle f(x - \Delta x) \\ &\quad \langle I(x - \Delta x) \rangle e^{-j 2\pi \alpha \Delta x} dx d\Delta x \end{aligned} \quad (3-56)$$

so that

$$\langle S(\alpha) \rangle = \langle S(\alpha) \rangle_0 + \langle S(\alpha) \rangle_1 \quad (3.57)$$

Equation (3.55) can be written

$$A \langle S(\alpha) \rangle_0 = \int_{-\infty}^{\infty} f(x) \langle I(x) \rangle \left[\int_{-\infty}^{\infty} f(x - \Delta x) \langle I(x - \Delta x) \rangle e^{-j 2\pi \alpha \Delta x} d\Delta x \right] dx \quad (3.58)$$

or

$$A \langle S(\alpha) \rangle_0 = H^*(\alpha) \int_{-\infty}^{\infty} f(x) \langle I(x) \rangle e^{-j 2\pi \alpha x} dx = |H(\alpha)|^2 \quad (3.59)$$

where $H(\alpha)$ is defined by

$$H(\alpha) = \int_{-\infty}^{\infty} f(x) \langle I(x) \rangle e^{-j 2\pi \alpha x} dx \quad (3.60)$$

Alternatively, $H(\alpha)$ may be expressed by

$$H(\alpha) = F(\alpha) * \Gamma(\alpha) \quad (3.61)$$

where the symbol $*$ indicates convolution and $F(\alpha)$ and $\Gamma(\alpha)$ are defined by

$$F(\alpha) = \int_{-\infty}^{\infty} f(x) e^{-j 2\pi \alpha x} dx \quad (3.62)$$

and

$$\Gamma(\alpha) = \int_{-\infty}^{\infty} \langle I(x) \rangle e^{-j 2\pi\alpha x} dx \quad (3.63)$$

We next rewrite Eq. (3.56) in the form

$$A \langle S(\alpha) \rangle_1 = \int_{-\infty}^{\infty} f(x) \langle I(x) \rangle \left[\int_{-\infty}^{\infty} f(x - \Delta x) \langle I(x - \Delta x) \rangle \right. \\ \left. |\gamma_p(\Delta x)|^2 e^{-j 2\pi\alpha\Delta x} d\Delta x \right] dx \quad (3.64)$$

which reduces to

$$A \langle S(\alpha) \rangle_1 = \int_{-\infty}^{\infty} \left[f(x) \langle I(x) \rangle H^*(\alpha) e^{-j 2\pi\alpha x} \right] * \\ \left[\mathcal{F}_{\alpha}^{\Delta x} \left\{ |\gamma_p(\Delta x)|^2 \right\} \right] dx \quad (3.65)$$

or finally,

$$A \langle S(\alpha) \rangle_1 = \left[|H(\alpha)|^2 \right] * \left[\mathcal{F}_{\alpha}^{\Delta x} \left\{ |\gamma_p(\Delta x)|^2 \right\} \right] \quad (3.66)$$

Combining Eqs. (3.57), (3.59) and (3.66) yields

$$A \langle S(\alpha) \rangle = \left[|H(\alpha)|^2 \right] + \left[|H(\alpha)|^2 \right] * \left[\int_{\alpha}^{\Delta x} \left\{ |\langle \gamma_{\rho}(\Delta x) \rangle|^2 \right\} \right] \quad (3.67)$$

We next use the result of the previous section, Eq. (3.48) to evaluate $\Gamma(\alpha)$ explicitly from Eq. (3.63).

$$\Gamma(\alpha) = \frac{2z_0 P}{(\lambda h)^2} \int_{-\infty}^{\infty} \langle \gamma_{\tau}(\Delta u) \rangle \left[\int_{-\infty}^{\infty} e^{-j 2\pi \frac{x}{\lambda h} [\alpha \lambda h + \Delta u]} dx \right] d\Delta u \quad (3.68)$$

but

$$\int_{-\infty}^{\infty} e^{-j 2\pi \frac{x}{\lambda h} [\alpha \lambda h + \Delta u]} dx = \lambda h \delta(\alpha \lambda h + \Delta u) \quad (3.69)$$

The sifting property of this δ -function can be used to obtain

$$\Gamma(\alpha) = \frac{2z_0 P}{\lambda h} \langle \gamma_{\tau}(\alpha \lambda h) \rangle \quad (3.70)$$

We next use the results of the previous section, Eq. (3.50), to evaluate

$$\int_{\alpha}^{\Delta x} \left\{ |\langle \gamma_{\rho}(\Delta x) \rangle|^2 \right\} \text{ explicitly.}$$

$$\mathcal{F}_{\alpha}^{\Delta x} \left\{ |\langle \gamma_{\rho}(\Delta x) \rangle|^2 \right\} = \left[\frac{I_o}{2z_o P} \right]^2 \iint_{-\infty}^{\infty} [g(u)]^2 [g(u_o)]^2 \left[\int_{-\infty}^{\infty} e^{-j 2\pi \frac{\Delta x}{\lambda h} \alpha \lambda h + u - u_o} d\Delta x \right] du du_o. \quad (3.71)$$

But the integral in square brackets will be recognized as a δ -function so that

$$\mathcal{F}_{\alpha}^{\Delta x} \left\{ |\langle \gamma_{\rho}(\Delta x) \rangle|^2 \right\} = \left[\frac{I_o}{2z_o P} \right]^2 (\lambda h) \int_{-\infty}^{\infty} [g(u_o)]^2 [g(u_o - \alpha \lambda h)]^2 du_o \quad (3.72)$$

or

$$\mathcal{F}_{\alpha}^{\Delta x} \left\{ |\langle \gamma_{\rho}(\Delta x) \rangle|^2 \right\} = \left[\frac{I_o}{2z_o P} \right]^2 (\lambda h) [g(\alpha \lambda h)]^2 \star [g(\alpha \lambda h)]^2 \quad (3.73)$$

where the symbol \star indicates autocorrelation.

We may now use these results to write an explicit expression for the one-dimensional power spectral density from Eq. (3.67).

$$\begin{aligned} \langle S(\alpha) \rangle &= \frac{1}{A} \left[\frac{2z_o P}{\lambda h} \right]^2 |F(\alpha)|^2 \star |\langle \gamma_{\tau}(\alpha \lambda h) \rangle|^2 \\ &+ \frac{1}{A} \frac{I_o^2}{\lambda h} |F(\alpha)|^2 \star |\langle \gamma_{\tau}(\alpha \lambda h) \rangle|^2 \star [g(\alpha \lambda h)]^2 \star [g(\alpha \lambda h)]^2 \end{aligned} \quad (3.74)$$

The two-dimensional power spectral density may now be written as

$$\begin{aligned}
 \langle S(\alpha, \Omega) \rangle = & \left[\iint_{-\infty}^{\infty} f(x, y) dx dy \right]^{-1} \left\{ [2z_0 P]^2 |F(\alpha, \Omega) * \langle \gamma_T(\alpha \lambda h, \Omega \lambda h) \rangle|^2 \right. \\
 & + [I_0 \lambda h]^2 |F(\alpha, \Omega) * \langle \gamma_T(\alpha \lambda h, \Omega \lambda h) \rangle|^2 * \left([g(\alpha \lambda h, \Omega \lambda h)]^2 \right. \\
 & \left. \left. \star [g(\alpha \lambda h, \Omega \lambda h)]^2 \right) \right\} .
 \end{aligned}$$

(3.75)

Since Eq. (3.75) is one of the principal results of this section, we wish to discuss its meaning in some detail. It should be emphasized that it is valid only for Gaussian fields, which is equivalent to requiring the scattering surface to be rough compared to the wavelength of the incident radiation.

The function $F(\alpha, \Omega)$ is defined as the Fourier transform of the aperture function $f(x, y)$ over which the power spectral density is averaged. When the aperture is small, its Fourier transform $F(\alpha, \Omega)$ is broad. This broad function convolved with $\langle \gamma_T(\alpha \lambda h, \Omega \lambda h) \rangle$ has the effect of spreading the narrow maximum in $\langle S(\alpha, \Omega) \rangle$ near zero spatial frequency by its contribution to the first term in Eq. (3.75) and smoothing $\langle S(\alpha, \Omega) \rangle$ throughout the entire spatial frequency range by its contribution to the second term in Eq. (3.75). On the other hand, when the aperture is very large, its Fourier transform is very narrow and approaches a δ -function. This δ -function when convolved with the spatial coherence function $\langle \gamma_T(\alpha \lambda h, \Omega \lambda h) \rangle$ merely replicates this function, and so the first term in Eq. (3.75) becomes a very narrow distribution at the origin whose shape is the squared modulus of the spatial coherence function. The second term is this same shape convolved with a factor that is proportional to the autocorrelation of the average intensity distribution in the (u, v) plane.

It is instructive to illustrate the functional dependence of Eq. (3.75) on physical parameters by using well behaved functional forms. For example, instead of choosing an infinite aperture $f(x, y)$ let us choose a finite aperture in the receiver plane of the form

$$f(x, y) = \exp \left[- (x^2 + y^2)/w^2 \right]$$

where w is the radius of the Gaussian aperture. With this choice of $f(x, y)$, the function

$$F(\alpha, \Omega) \triangleq \int_{\alpha, \Omega}^{x, y} f(x, y) = \pi w^2 \exp \left[- \pi w^2 (\alpha^2 + \Omega^2) \right],$$

and the normalizing area A becomes

$$A \triangleq \iint_{-\infty}^{\infty} f(x, y) dx dy = \pi w^2.$$

Next, we choose $\langle \gamma_T(\Delta u, \Delta v) \rangle$ to be a narrow Gaussian of the form

$$\langle \gamma_T(\Delta u, \Delta v) \rangle = \exp \left[- (\Delta u^2 + \Delta v^2)/R^2 \right]$$

where R is the "coherence radius" of the spatial coherence function. We can now evaluate the convolution integral

$$F(\alpha, \Omega) * \langle \gamma_T(\alpha \lambda h, \Omega \lambda h) \rangle = \frac{\pi^2}{\pi + \left(\frac{\lambda h}{wR}\right)^2} \cdot \exp \left[- \frac{\left(\frac{\lambda h}{R}\right)^2}{\pi + \left(\frac{\lambda h}{wR}\right)^2} (\alpha^2 + \Omega^2) \right]$$

which is itself a Gaussian distribution that is broadened by the effect of the finite aperture of radius W .

When the receiver aperture becomes very large, that is, when

$$(\lambda h / WR)^2 \ll \pi ,$$

$$\begin{aligned} \langle S(\alpha, \Omega) \rangle &\doteq \frac{(2z_o \pi P)^2}{\pi W^2} \left\{ \exp \left[-2 (\lambda h / R)^2 (\alpha^2 + \Omega^2) \right] \right. \\ &+ \left[\frac{I_o \lambda h}{2z_o P} \right]^2 \exp \left[-2 (\lambda h / R)^2 (\alpha^2 + \Omega^2) \right] * \left(\left[g(\alpha \lambda h, \Omega \lambda h) \right]^2 \right. \\ &\left. \star \left[g(\alpha \lambda h, \Omega \lambda h) \right]^2 \right) \left. \right\} \end{aligned}$$

which, for emphasis, may be written as

$$\begin{aligned} \langle S(\alpha, \Omega) \rangle &\doteq \frac{(2z_o \pi P)^2}{W^2} \left\{ \left| \langle \gamma_T(\alpha \lambda h, \Omega \lambda h) \rangle \right|^2 \right. \\ &+ \left[\frac{I_o \lambda h}{2z_o P} \right]^2 \left| \langle \gamma_T(\alpha \lambda h, \Omega \lambda h) \rangle \right|^2 * \left(\left[g(\alpha \lambda h, \Omega \lambda h) \right]^2 \right. \\ &\left. \star \left[g(\alpha \lambda h, \Omega \lambda h) \right]^2 \right) \left. \right\} . \end{aligned}$$

An important practical conclusion can be extracted from the preceding example relative to the requirement on aperture size W in order to faithfully determine $\langle \gamma_T(\alpha \lambda h, \Omega \lambda h) \rangle$ from a measurement of $\langle S(\alpha, \Omega) \rangle$. In the next section where we relate it to characteristics of the scattering surface, we shall demonstrate the importance of knowing $\langle \gamma_T(\alpha \lambda h, \Omega \lambda h) \rangle$. The size of a resolution element r_o associated with an aperture of size W located at a distance h from an object is given approximately by

$$r_o \doteq \lambda h / W .$$

Thus, the above condition $(\lambda h / WR)^2 \ll \pi$ is equivalent to requiring that $r_o \ll R$.

In other words, to determine characteristics of the scattering surface through a measurement of power spectral density, the aperture that is used must be sufficiently large to resolve surface structure smaller than the coherence area on the surface.

D. SPATIAL COHERENCE AS A FUNCTION OF SURFACE CHARACTERISTICS

The normalized spatial coherence in the (u, v) plane is defined in terms of the fields $E_p(u_1, v_1)$ and $E_p(u_2, v_2)$ which we will relate to statistical characteristics of the scattering surface. Using Eq. (3.34) and the definition of the normalized coherence function, we may write

$$\langle \gamma_T(\Delta u, \Delta v) \rangle = \left\langle e^{-jk \left\{ \left[w(u_1, v_1) - w(u_2, v_2) \right] (1 + \cos \beta) \right\}} e^{-jk(u_1 - u_2) \sin \beta} \right\rangle_e \quad (3.76)$$

To evaluate the ensemble average indicated in Eq. (3.76), we need to know the statistical distribution function $P\{w(u, v)\}$ for the surface height $w(u, v)$. We shall take the surface height to be a stationary zero-mean Gaussian random variable with probability distribution

$$P \{w(u, v)\} \triangleq e^{-\frac{[w(u, v)]^2}{2\sigma^2}} \quad (3.77)$$

It follows directly that the joint probability distribution function is given by

$$P \{w_1, w_2\} = \left[2\pi\sigma^2 \sqrt{1-\rho^2} \right]^{-1} \exp \left\{ -\frac{w_1^2 - 2\rho w_1 w_2 + w_2^2}{2\sigma^2 (1-\rho^2)} \right\} \quad (3.78)$$

where we have adopted, for convenience, the notation

$$w_1 \equiv w(u_1, v_1) \quad (3.79a)$$

$$w_2 \equiv w(u_2, v_2) \quad (3.79b)$$

$$\rho \equiv \rho(\Delta u, \Delta v) \quad (3.79c)$$

and where ρ , the normalized correlation function of the surface heights, is defined by

$$\rho(\Delta u, \Delta v) \triangleq \frac{\langle w(u, v) w(u - \Delta u, v - \Delta v) \rangle}{\sigma^2} \quad (3.80)$$

with

$$\sigma^2 \triangleq \langle [w(u, v)]^2 \rangle. \quad (3.81)$$

We now recognize that the quantity in ensemble brackets in Eq. (3.76) can be interpreted as the characteristic function for the distribution $p\{w_1, w_2\}$, and thus Eq. (3.76) can be written

$$\langle \gamma_T(\Delta u, \Delta v) \rangle = e^{-jk\Delta u \sin \beta} \left\{ e^{-\left[k\sigma(1 + \cos \beta) \right]^2 \left[1 - \rho(\Delta u, \Delta v) \right]} \right\}. \quad (3.82)$$

We now have an expression for the normalized spatial coherence in the (u, v) plane in terms of surface characteristics σ and ρ .

The surface height autocorrelation function $\rho(\Delta u, \Delta v)$ can be evaluated for a given surface if the surface height power spectral density $\psi(f_u, f_v)$ is known since these quantities are known to form a Fourier transform pair.

$$\rho(\Delta u, \Delta v) = \iint_{-\infty}^{\infty} \psi(f_u, f_v) e^{-j2\pi \left[f_u \Delta u + f_v \Delta v \right]} df_u df_v. \quad (3.83)$$

E. COMPARISON OF RESULTS WITH PREVIOUS WORK

1. The Work of Crane

In Appendix B, Goodman has reviewed Crane's theory⁸ and has shown that Crane's Eq. (39) is valid only when the rms surface roughness is much less than one wavelength. On the other hand, the present theory assumes that the phases of the fields on the scattering surface are uniformly distributed on the interval $[0, 2\pi]$ which assumption is valid only when the rms surface roughness is on the order of a wavelength or greater. Thus, our present result and Crane's Eq. (39) are valid for different regimes of rms surface roughness and cannot be directly compared. However, in Appendix B, Goodman also, has used Crane's more general expression Eq. (38) as a starting point to develop an expression for the power spectral density of the speckle pattern in the (x, y) plane

that is valid for large surface roughness, and we shall compare our results with that expression.

First, let us restate here the result of Goodman's extension of Crane's theory as developed in Appendix B. Goodman used an illuminated spot on the (u, v) plane of dimension L by L and assumed a symmetric Gaussian autocorrelation function of the form*

$$\rho(\Delta u, \Delta v) = \exp \left\{ -\frac{\Delta u^2 + \Delta v^2}{R^2} \right\} \quad (3.84)$$

where R is the surface correlation length. The result of his extension predicts that the power spectral density should have the approximate form

$$E \left[S(\alpha^1, 0) \right] \propto e^{-32\pi^2 \left(\frac{\sigma}{\lambda} \right)^2 \left(\frac{L}{R} \right)^2 \left(\frac{\alpha^1}{\alpha_{\max}^1} \right)^2} \quad (3.85)$$

for low spatial frequencies and the approximate form

$$E \left[S(\alpha^1, 0) \right] \propto \frac{\Lambda \left(\frac{\alpha^1}{\alpha_{\max}^1} \right)}{32\pi \left(\frac{\sigma}{\lambda} \right)^2 \left(\frac{L}{R} \right)^2} \quad (3.86)$$

for high spatial frequencies where $\Lambda \left(\frac{\alpha^1}{\alpha_{\max}^1} \right)$ is a triangle function having value unity for zero argument and value zero for unity argument and

$$\alpha_{\max}^1 = \frac{2\pi L}{\lambda h} \quad (3.87)$$

*Although we have chosen a Gaussian autocorrelation function for simplicity in this illustration, Goodman has shown that almost any autocorrelation function that behaves parabolically near the origin will yield the same result as we obtain here. For a discussion of this, see Appendix B.

We note that the spatial frequency as defined in Appendix B is 2π times the spatial frequencies used in the text so that in order to distinguish the two, we place a prime on spatial frequencies from Appendix B.

Now we turn to our expression in Eq. (3.75) and note that if the aperture $f(x, y)$ over which the power spectral density is averaged is infinite in extent as Crane has taken it to be, $F(\alpha, \Omega)$ becomes a δ -function and Eq. (3.75) reduces to

$$\begin{aligned} \left\langle S\left(\frac{\alpha^1}{2\pi}, 0\right) \right\rangle &\propto \left| \left\langle \gamma_\tau \left(\frac{\alpha^1 \lambda h}{2\pi}, 0 \right) \right\rangle \right|^2 \\ &+ \left[\frac{I_o \lambda h}{2z_o P} \right]^2 \left| \left\langle \gamma_\tau \left(\frac{\alpha^1 \lambda h}{2\pi}, 0 \right) \right\rangle \right|^2 * \left[g\left(\frac{\alpha^1 \lambda h}{2\pi}, 0\right) \right]^2 \star \left[g\left(\frac{\alpha^1 \lambda h}{2\pi}, 0\right) \right]^2. \end{aligned} \quad (3.88)$$

But from Eq. (3.82)

$$\begin{aligned} \left| \left\langle \gamma_\tau \left(\frac{\alpha^1 \lambda h}{2\pi}, 0 \right) \right\rangle \right|^2 &= e^{-2(2k\sigma)^2} \left[1 - \rho \left(\frac{\alpha^1 \lambda h}{2\pi}, 0 \right) \right] \\ &\approx e^{-32\pi^2 \left(\frac{\sigma}{\lambda} \right)^2 \left(\frac{L}{R} \right)^2 \left(\frac{\alpha^1}{\alpha_{\max}^1} \right)^2} \end{aligned} \quad (3.89)$$

where we have taken the normal incidence case for which $\cos \beta = 1$.

In the second term of Eq. (3.88), we make the approximation that

$$\left| \left\langle \gamma_\tau \left(\frac{\alpha^1 \lambda h}{2\pi}, 0 \right) \right\rangle \right|^2 \text{ behaves like a } \delta\text{-function as is done in Appendix B}$$

so that the result is

$$\left\langle S\left(\frac{\alpha^1}{2\pi}, 0\right) \right\rangle \propto e^{-32\pi^2 \left(\frac{\sigma}{\lambda}\right)^2 \left(\frac{L}{R}\right)^2 \left(\frac{\alpha^1}{\alpha_{\max}^1}\right)^2} \quad (3.90)$$

for low frequencies and

$$\left\langle S\left(\frac{\alpha^1}{2\pi}, 0\right) \right\rangle \propto \frac{\Lambda\left(\frac{\alpha^1}{\alpha_{\max}^1}\right)}{32\pi \left(\frac{\sigma}{\lambda}\right)^2 \left(\frac{L}{R}\right)^2} \quad (3.91)$$

for high frequencies. We note that Eqs. (3.90) and (3.91) are identical to Eqs. (3.85) and (3.86) respectively. That is, we note here that our general Eq. (3.75) reduces to the specific result Goodman obtained in Appendix B when he extended Crane's theory for the case of rough surfaces and infinite aperture $f(x, y)$.

2. The Early Work of Goodman and Goldfischer

In 1963 Goodman¹⁷ and in 1965 Goldfischer¹⁸ predicted that the power spectral density should have the form of the sum of a δ -function at the origin and a term that is proportional to the autocorrelation of the average brightness distribution at the target.^{5,7} In their analysis, the power spectral density was averaged over (x, y) space; the implicit assumption in their model of the surface was that the spatial coherence at the target was completely destroyed by the diffuse surface, i.e., the spatial coherence behaved similarly to a δ -function. In our notation, these conditions correspond to

$$\langle \gamma_{\tau}(\alpha\lambda h, \Omega\lambda h) \rangle = \frac{N\delta(\alpha\lambda h, \Omega\lambda h)}{\iint_{-\infty}^{\infty} d(\alpha\lambda h) d(\Omega\lambda h)} \quad (3.92)$$

where N is a normalization factor

and

$$F(\alpha, \Omega) = \delta(\alpha, \Omega) \quad . \quad (3.93)$$

Thus, Eq. (3.75) takes the form

$$\begin{aligned} \langle S(\alpha, \Omega) \rangle = \mu(\alpha\lambda h, \Omega\lambda h) & \left\{ \left[2z_o \Gamma \right]^2 \delta(\alpha\lambda h, \Omega\lambda h) \right. \\ & \left. + \left[I_o \lambda h \right]^2 \left[g(\alpha\lambda h, \Omega\lambda h) \right]^2 \star \left[g(\alpha\lambda h, \Omega\lambda h) \right]^2 \right\} . \end{aligned} \quad (3.94)$$

We note that (3.94) has exactly the form predicted by Goodman and Goldfischer; namely, a δ -function behavior at the origin and a term proportional to the autocorrelation of the average brightness distribution at the scattering surface.

F. SCATTERING FROM THE SEA

1. General

The Huygens-Fresnel principle has been applied with considerable success to the scattering of optical radiation from diffuse surfaces such as opal glass, paint, paper, sandblasted metals, ground and etched glass, and the like and the experimental evidence is such that the underlying theory appears to be sound. However, the theoretical concept developed here which relates surface characteristics to average scattered intensity distribution through the spatial coherence function, to our knowledge has not been experimentally verified for the scattering of optical radiation from the surface of the ocean. Nevertheless, there is every reason to believe that this approach is sound within the constraints of scalar diffraction theory and small angle approximations.

Normally, one might describe the rather smooth surface of the ocean as specular rather than diffuse in nature. However, characterizing the ocean's surface with these rather loosely defined terms should either be avoided or the terms should be carefully defined because the surface can either be characterized as diffuse or specular depending, among other things, on the size of the illuminating beam. Moreover, no such distinction is required in applying the Huygens-Fresnel principle; but it does require the radius of curvature of the surface to be large compared to the wavelength of the radiation used.

In the following sections, we apply the results of our theoretical work specifically to scattering from the ocean surface. In doing this, we recognize several important considerations that are specific to this application. In particular, finite apertures both in space and time must be used to obtain measurements; thus, the sampling requirements for meaningful measurements must be carefully analyzed. These sampling requirements are intimately related to the conditions of validity of the theoretical work and, among other things, will dictate constraints on such things as viewing angle, height of the observation plane, and the like. Furthermore, in the evaluation of the feasibility

of the concept for measuring surface characteristics, it is important to know, through calculations, the sensitivity of the measured quantity to the assumed surface characteristics and expected perturbations in these characteristics. In what follows, we have only superficially examined these considerations and expect to treat them in more depth as our work continues.

2. Conditions of Validity

In this subsection, we examine conditions imposed on surface roughness, spot size, wavelength, range, and viewing angle in order to validate the approximations made in Section III-C. We note that the conditions imposed here are sufficient, but they may be unnecessary for numerical accuracy. In fact, we strongly suspect that in some cases the conditions are much more stringent than is necessary and that given further effort, less stringent conditions could be found that would still permit the use of the expressions developed in Section III-C.

In Section III-C, the distance R from a point on the illuminated spot to the observation point in the (x, y) plane was expanded in a binomial series (Eq. 3.28); and subsequently, all terms in the series second order and higher in B and $w(u, v)$ and first order and higher in the product $Bw(u, w)$ were dropped. The resulting approximate expressions are valid when the terms that were dropped are negligible. Thus, it is sufficient to impose conditions which will ensure that the next higher order terms in the series have a negligible effect on the result. These terms are listed here as:

$$T_1 = -\frac{h B^2}{8} \quad (3.96a)$$

$$T_2 = \frac{B w(u, v)}{2} \quad (3.96b)$$

$$T_3 = \frac{B w^2(u, v)}{2h} \quad (3.96c)$$

Dropping these terms is equivalent to making the statement that

$$e^{j \frac{2\pi}{\lambda} T} \approx 1 \quad (3.97)$$

We arbitrarily choose the criterion

$$\left| \frac{2\pi T}{\lambda} \max \right| < \frac{\pi}{4} \quad (3.98)$$

as satisfying Eq. (3.97).

a. On-axis

We now examine the on-axis case, that is, the case for which the observation point is directly above the illuminated spot so that $x = y = 0$. If the illuminated spot has dimensions L by L , the following three conditions result from Eqs. (3.96) and (3.98):

$$h^3 > \frac{L^4}{4\lambda} \quad (3.99a)$$

$$h^2 > \frac{\sigma L^2}{\lambda} \quad (3.99b)$$

$$h^3 > \frac{\sigma^2 L^2}{\lambda} \quad (3.99c)$$

where we have used σ , the rms value of $w(u, v)$, instead of $w(u, v)$ in Eq. (3.92). For the purpose of illustration, we choose a numerical example for which $L = 30$ m, $\lambda = 10^{-5}$ m, and $\sigma = 0.5$ m. Then Eqs. (3.99a, b, c) become

$$h > \sqrt[3]{\frac{(30)^4}{4 \times 10^{-5}}} = 2.7 \times 10^3 \text{ m} \quad (3.100a)$$

$$h > \sqrt[2]{\frac{(0.5)^2 (30)^2}{10^{-5}}} = 6.7 \times 10^3 \text{ m} \quad (3.100b)$$

$$h > \sqrt[3]{\frac{(0.5)^2 (30)^2}{10^{-5}}} = 2.82 \times 10^2 \text{ m} \quad (3.100c)$$

respectively.

b. Off-axis

The conditions become much more stringent when the observation point (Q, Q) is not on the z-axis. If we define $\tan \theta = Q/h$ and take $Q \gg L$, the following conditions result:

$$\tan^3 \theta < \frac{\lambda}{16Q^5} \quad (3.101a)$$

$$\tan^2 \theta < \frac{\lambda}{8\sigma} \quad (3.101b)$$

$$\tan^2 \theta < \frac{h\lambda}{8\sigma^2} \quad (3.101c)$$

3. Numerical Calculations and Physical Interpretation

In Section III-C, we showed that the ensemble average intensity in the observation plane is proportional to the Fourier transform of the normalized spatial coherence in the target plane. Later, in Section III-D, we demonstrated how the ensemble characteristics of the surface, σ and $\rho(\Delta u, \Delta v)$, determine the target spatial coherence. Finally, we indicated that these ensemble characteristics of the surface can be calculated if the surface height power spectral density is known. We shall make use of these relationships to calculate

the average intensity distributions in the observation plane from certain assumed surface height power spectral densities that are known to approximately describe the ocean surface. From these calculations, we hope to demonstrate the sensitivity of the scattered intensity to perturbations in the surface height power spectral density, particularly at high spatial frequencies.

To begin, we restate Eq. (3.51), (3.82), and (3.83) in one-dimensional form.

$$\langle I(x) \rangle \propto \frac{\Delta u}{\frac{x}{\lambda h}} \left\{ \langle \gamma_T(\Delta u) \rangle \right\} \quad (3.102)$$

$$\langle \gamma_T(\Delta u) \rangle = e^{-(2k\sigma)^2} [1 - \rho(\Delta u)] \quad (3.103)$$

$$\rho(\Delta u) = \int_{-\infty}^{\infty} \psi(f) e^{-j2\pi f \Delta u} df \quad (3.104)$$

Combining these equations yields an explicit expression for the average intensity in terms of the known surface height power spectral density $\psi(f)$.

$$\langle I(x) \rangle \propto \int_{-\infty}^{\infty} e^{-j\frac{2\pi x \Delta u}{\lambda h}} e^{-(2k\sigma)^2} \left\{ 1 - \int_{-\infty}^{\infty} \psi(f) e^{-j2\pi f \Delta u} df \right\} d \Delta u \quad (3.105)$$

We choose to express the surface height power spectral density as the sum of an unperturbed and a perturbing function. In normalized form, it is given by

$$\psi(f) = \psi_0(f) + \psi_1(f) \quad (3.106)$$

where $\psi_0(f)$ is the unperturbed function and $\psi_1(f)$ is the perturbing function. Similarly, from Eq. (3.104) we define

$$\rho_0(\Delta u) \triangleq \int_{-\infty}^{\infty} \psi_0(f) e^{-j 2 \pi f \Delta u} d f \quad (3.107)$$

and

$$\rho_1(\Delta u) \triangleq \int_{-\infty}^{\infty} \psi_1(f) e^{-j 2 \pi f \Delta u} d f \quad (3.108)$$

so that

$$\rho(\Delta u) = \rho_0(\Delta u) + \rho_1(\Delta u) \quad (3.109)$$

Thus, we associate $\rho_0(\Delta u)$ with the unperturbed power spectral density and $\rho_1(\Delta u)$ with the perturbing power spectral density.

Now Eq. (3.105) may be rewritten as

$$\langle I(x) \rangle \propto \int_{-\infty}^{\infty} e^{-j 2 \pi \frac{x \Delta u}{\lambda h}} e^{-(2k\sigma)^2 [1 - \rho(\Delta u)]} d \Delta u \quad (3.110)$$

This Fourier transformation is difficult to do analytically. However, if $\rho(\Delta u)$ is expressed as a power series in $(\Delta u)^2$ and we retain only the first two terms, the approximate expression for the ensemble average intensity becomes

$$\langle I(x) \rangle \propto \frac{1}{2k\sigma K_0} \exp - \left[\frac{\pi x}{2k\sigma K_0 \lambda h} \right]^2 \quad (3.111)$$

where K_0^2 is the coefficient of $(\Delta u)^2$ in the Maclaurin's expansion for $\rho(\Delta u)$ i.e.,

$$\rho(\Delta u) = 1 - K_0^2 \Delta u^2 + K_1^4 \Delta u^4 - \dots \quad (3.112)$$

To illustrate the concepts developed here, we choose a sample power spectral density in the form

$$\psi_0(f) = \begin{cases} K f_m^{-5} f^4 & 0 < |f| < f_m \\ K f_m^3 f^{-4} & f_m < |f| < f_c \\ 0 & \text{elsewhere} \end{cases} \quad (3.113a)$$

$$(3.113b)$$

$$(3.113c)$$

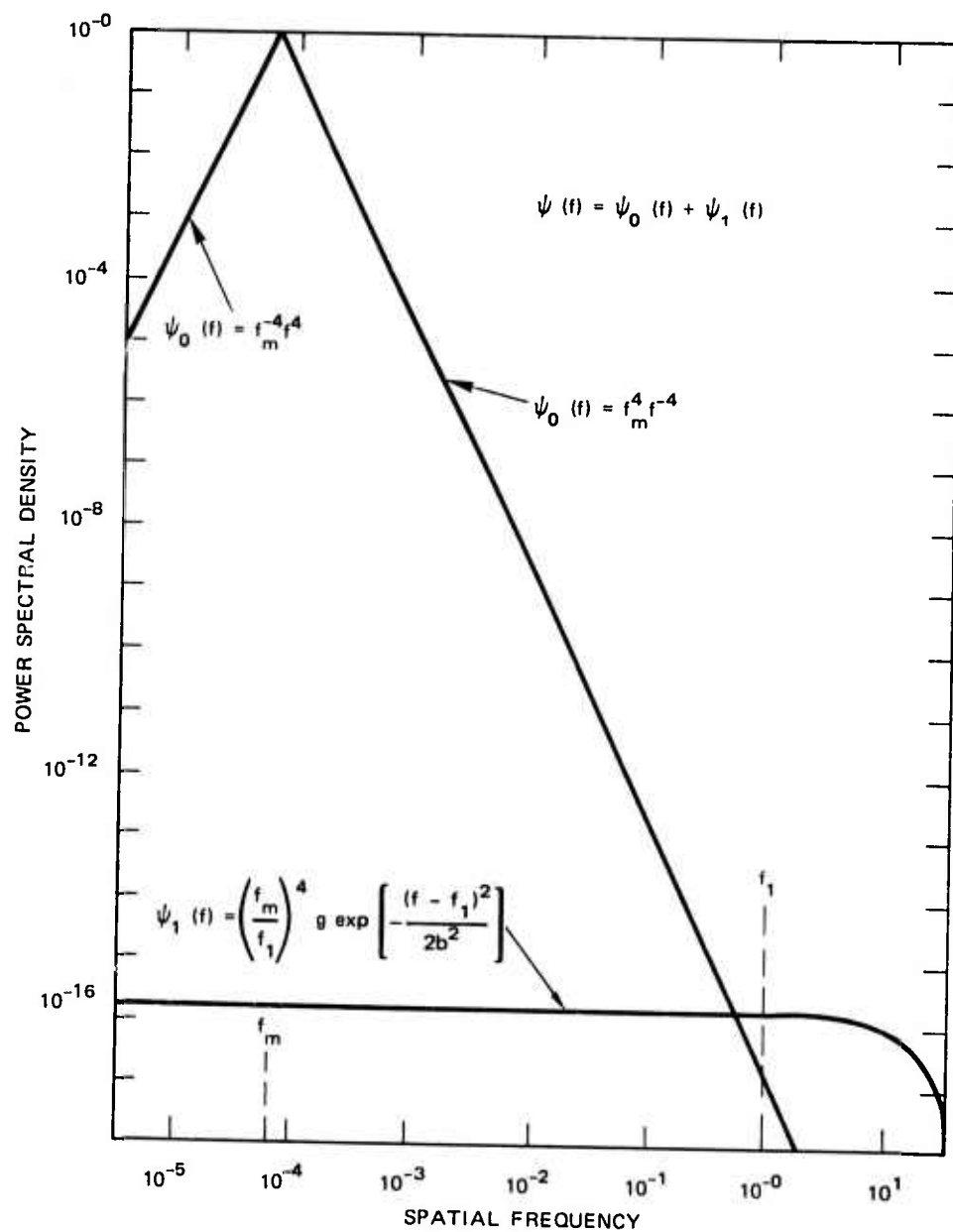
and a perturbing function of the form

$$\psi_1(f) = \begin{cases} K g \left(\frac{f_m}{f_1} \right)^3 \left(\frac{1}{f_1} \right) \left[e^{-\frac{(f-f_1)^2}{2b^2}} + e^{-\frac{(f+f_1)^2}{2b^2}} \right] & -f_c < f < f_c \\ 0 & \text{elsewhere} \end{cases} \quad (3.114a)$$

$$(3.114b)$$

Normalized forms of $\psi_0(f)$ and $\psi_1(f)$ are plotted in Figure 25. We note that f_m is the spatial frequency for which $\psi_0(f)$ is maximum, f_1 is the center spatial frequency for the Gaussian perturbation, b is the bandwidth of the Gaussian perturbation, and g is the ratio of the strength of the Gaussian perturbation at its center spatial frequency to the strength of the unperturbed function. Thus,

$$g \triangleq \psi_1(f_1)/\psi_0(f_1) \quad (3.115)$$



SA-2422-12

FIGURE 25 ASSUMED FORM OF THE POWER SPECTRAL DENSITIES OF NATURAL WAVE HEIGHT AND PERTURBATION

Further, f_c is a cutoff frequency beyond which the spectral densities are identically zero. Using these sample functions and the relations developed above, we have obtained approximate analytical expressions for $\rho_0(\Delta u)$, $\rho_1(\Delta u)$, and K_0 .

$$\rho_0(\Delta u) \approx K \left[\frac{16}{15} - \frac{2}{3} \left(\frac{f_m}{f_c} \right)^3 \right] - K \Delta u^2 \frac{(2\pi f_m)^2}{2!} \left[\frac{16}{7} - 2 \frac{f_m}{f_c} \right] \quad (3.116)$$

$$\rho_1(\Delta u) \approx K g \left(\frac{f_m}{f_1} \right)^3 \left(\frac{b}{f_1} \right) \sqrt{2\pi} \left\{ M - \Delta u^2 \frac{(2\pi)^2}{2!} \left[(f_1^2 + b^2) M - \frac{2b}{\sqrt{2\pi}} N \right] \right\} \quad (3.117)$$

and

$$K_0 = \frac{\frac{(2\pi)^2}{2!} \left\{ f_m^2 \left(\frac{16}{7} - 2 \frac{f_m}{f_c} \right) + \sqrt{2\pi} g \left(\frac{f_m}{f_1} \right)^3 \left(\frac{b}{f_1} \right) \left[M (f_1^2 + b^2) - \frac{2b}{\sqrt{2\pi}} N \right] \right\}}{\left[\frac{16}{15} - \frac{2}{3} \left(\frac{f_m}{f_c} \right)^3 + \sqrt{2\pi} g \left(\frac{f_m}{f_1} \right)^3 \left(\frac{b}{f_1} \right) M \right]} \quad (3.118)$$

where

$$M = \operatorname{erf} \left[(f_c - f_1) / \sqrt{2b} \right] + \operatorname{erf} \left[(f_c + f_1) / \sqrt{2b} \right] \quad (3.119)$$

$$N = (f_c - f_1) \exp \left[-(f_c + f_1)^2 / 2b^2 \right] + (f_c + f_1) \exp \left[-(f_c - f_1)^2 / 2b^2 \right] \quad (3.120)$$

$$\text{and } K = \left[\frac{16}{15} - \frac{2}{3} \left(\frac{f_m}{f_c} \right)^3 + \sqrt{2\pi} g \left(\frac{f_m}{f_1} \right)^3 \left(\frac{b}{f_1} \right) M \right] \quad (3.121)$$

To obtain numerical results, we assume the following set of values that appear reasonable.

$$f_m = 6.4 \times 10^{-5} \text{ cm}^{-1} \quad f_1 = 1 \text{ cm}^{-1} \quad f_c = 100 \text{ cm}^{-1} \quad b = 10 \text{ cm}^{-1}.$$

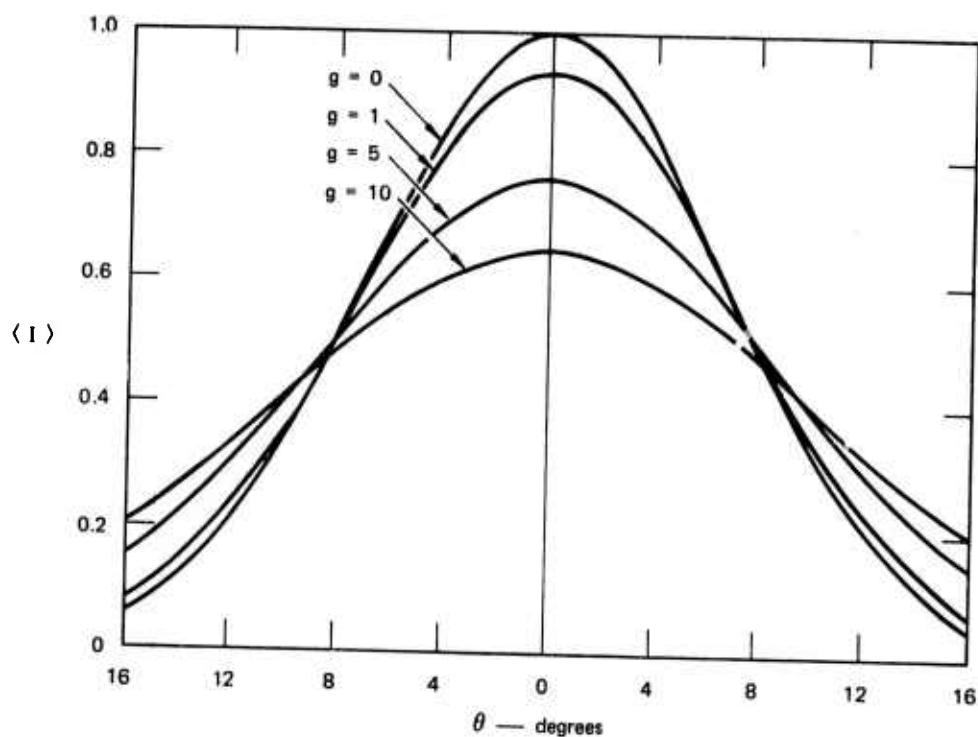
An examination of the expressions for ρ_0 and ρ_1 given by Eqs. (3.116) - (3.121) shows that the introduction of the cutoff has an extremely small effect on these expressions as long as the following conditions are met.

$$f_m \ll f_1 \ll f_c; \quad 5b < f_c. \quad (3.122)$$

These conditions seem appropriate for the assumed sample functions. In the subsequent treatment, the cutoff frequency is considered essentially infinite since these conditions are satisfied.

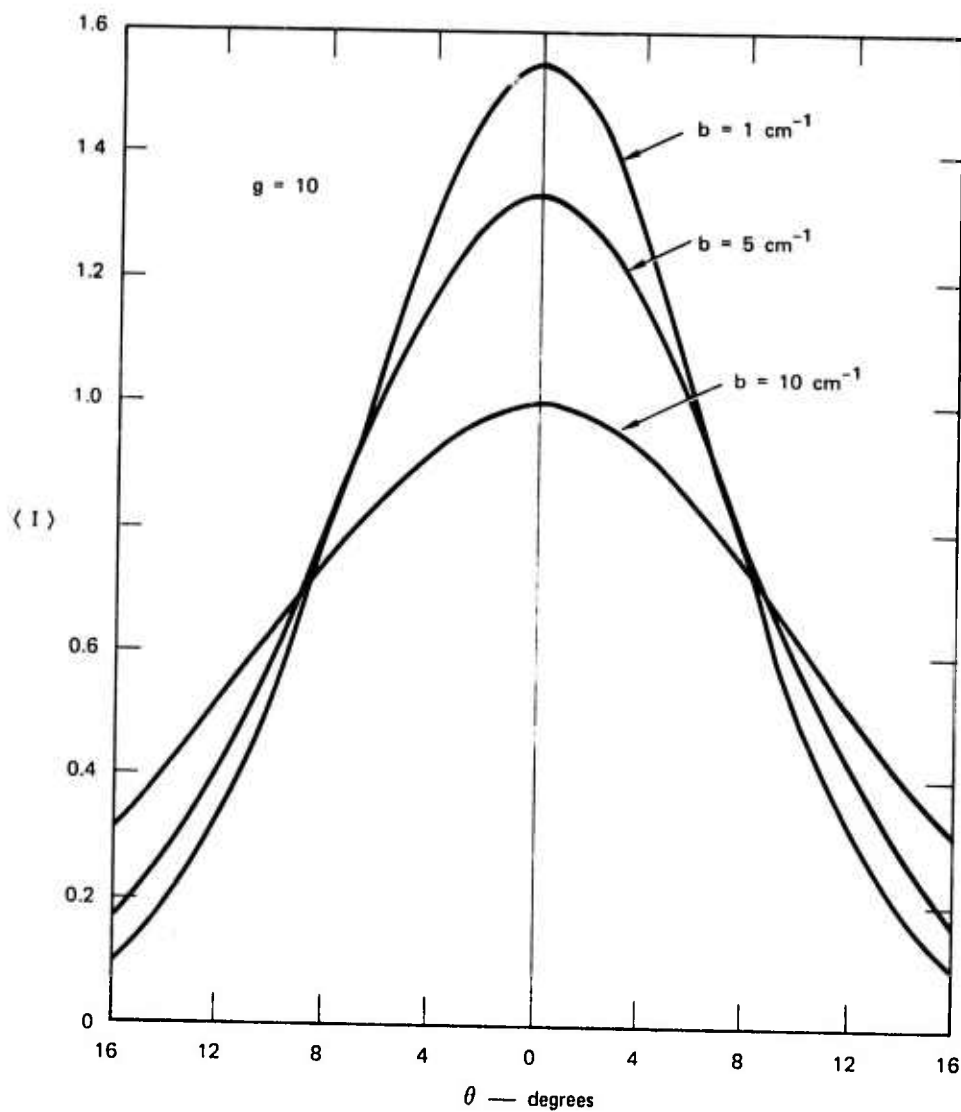
The ensemble average intensity was then calculated by using Eq. (3.111) for several combinations of the values of g , the magnitude of the Gaussian perturbation and b , its width, keeping f_m and f_1 constant. Plots of the ensemble average intensity versus (x/h) , the angle from the vertical in the observation plane are shown in Figures 26 and 27. In Figure 26, the curves show the changes in intensity that occur when increasing amounts of perturbation are introduced. The curves have been normalized with respect to the value of the intensity when the perturbation is absent. The intensity is seen to decrease appreciably when the perturbation increases in peak magnitude with the width of the Gaussian perturbation held constant. Figure 27 shows the behavior of the average intensity as the width of the Gaussian perturbation is changed with the peak magnitude held constant. These curves have been normalized with respect to the curve with $b = 10$.

Both these sets of curves suggest that the changes in the intensity are related to the energy content of the perturbation (area under the Gaussian). However, examination of the expression for K_0 [Eq. (3.118)] shows that while



SA-2422-13

FIGURE 26 PLOTS OF AVERAGE INTENSITY DISTRIBUTION SHOWING EFFECT OF DIFFERENT STRENGTHS OF GAUSSIAN PERTURBATION OF CONSTANT WIDTH



SA-2422-14

FIGURE 27 PLOTS OF AVERAGE INTENSITY DISTRIBUTION SHOWING EFFECT OF DIFFERENT WIDTHS OF GAUSSIAN PERTURBATION OF CONSTANT STRENGTH

the energy content (the product bg) is involved, an increase in the width is much more effective than an increase in the magnitude of the perturbation resulting from the presence of additional factors involving b .

Consideration of the same equation also brings out the effect of changing f_1 , the location of the perturbation. Since g is defined relative to the magnitude of the sample function $\psi_0(f_1)$ [Eq. (3.113b)], keeping g constant while decreasing f_1 increases the energy content of the perturbation. However, if the product gf_1^{-4} is kept constant, Eq. (3.114a) shows that $\psi_1(f)$ is unchanged in energy content; and Eq. (3.118) shows that K_0 is also constant to first order ($f_1 \ll b$). Thus, the observed average intensity is unchanged. Therefore, the conclusion is that identical perturbations have the same effect (to first order) on the average intensity regardless of their spectral position.

We are uncertain about the physical implications of these numerical results. Several assumptions had been made to complete this first order analysis. It will be of interest to examine more realistic power spectral density functions and carry out these calculations in more detail. For example, of fundamental importance to the ultimate objective of the program would be to observe the dissipation of a narrow band perturbation at high wave numbers as it moves to lower wave numbers, simultaneously increasing in bandwidth and losing energy content.

The approximation made in Eq. (3.111) implies that only the effect of wave slopes has been retained in the analysis, since the coefficients of successive even powers of Δu in the Maclaurin's expansion [Eq. (3.112)] can be related to the slope spectrum, curvature spectrum, and the like. Successively higher approximations may be made by the use of numerical Fourier transform techniques. The effects of the slopes, the curvatures, and so on can then conceivably be isolated.

REFERENCES

1. N. G. Jerlov, Optical Oceanography (Elsevier Publishing Co., New York, 1968).
2. J. E. Tyler, Measurements of Spectral Irradiance Underwater (Gordon & Breach, New York, 1970).
3. V. M. Zolotarev, et al., "Dispersion and Absorption of Liquid Water in the Infrared and Radio Regions of the Spectrum," Optics and Spectroscopy, 27, 430 (1969).
4. W. L. Wolfe, ed., Handbook of Military Infrared Technology, (Superintendent of Documents, U.S. Government Printing Office, Washington, D.C., 1965).
5. K. K. Chow and W. B. Leonard, "Efficient Octave-bandwidth Microwave Light Modulators," IEEE J. Quant. Electronics, QE-6, 789 (1970).
6. Private communication with GTE Sylvania Electro-optic Organization, Mountain View, California.
7. Private communication with II-VI Incorporated, Glenshaw, Pennsylvania.
8. J. E. Kiefer, et al., "Intracavity CdTe Modulators for CO₂ Lasers," IEEE J. Quant. Electronics, QE-8, 173 (1972).
9. J. E. Fieffer, et al., "Electro-optic Characteristics of CdTe at 3.39 and 10.6 μ ," Appl. Phys. Lett., 15, 26 (1969).
10. J. W. Goodman, "Some Effects of Target-Induced Scintillation on Optical Radar Performance," Proc. IEEE, 53, 1688 (1965).
11. American Institute of Physics Handbook (McGraw-Hill Book Company, New York, New York, 1957).
12. Electro-optics Handbook (RCA Defense Electronic Products, Burlington, Massachusetts, 1968).
13. W. K. Pratt, Laser Communication Systems (John Wiley and Sons, Inc., New York, New York, 1969).
14. L. Esterowitz, et al., Proceedings of the IRIS Detector Specialty Group Meeting (U), Willow Run Laboratories, Ann Arbor, Michigan, May 1972 (SECRET).

15. C. Vériè, et al., "Gigahertz Cutoff Frequency Capabilities of CdHgTe Photovoltaic Detectors at 10.6μ ," IEEE J. Quant. Electronics, QE-8, 180 (1972).
16. P. Bratt, et al., "A Status Report on Infrared Detectors," Infrared Physics, 1, 27 (1961).
17. J. W. Goodman, Statistical Properties of Laser Sparkle Patterns, Stanford Electronics Laboratory Report, Stanford, California (December 1963).
18. L. I. Goldfischer, "Autocorrelation Function and Power Spectral Density of Laser-Produced Speckle Patterns," J. Opt. Soc. Am., 55, 247 (1965).
19. R. B. Crane, "Use of a Laser-Produced Speckle Pattern to Determine Surface Roughness," J. Opt. Soc. Am., 60 1658 (1970).
20. B. Kinsman, Wind Waves, p. 344 (Prentice-Hall Inc., Englewood Cliffs, New Jersey, 1965).
21. J. D. Rigden, et al., "The Granularity of Scattered Optical Maser Light," Proc. IEEE, 50, 2367 (1962).
22. B. M. Oliver, "Sparkling Spots and Random Diffraction," Proc. IEEE, 51, 220 (1963).
23. S. Lowenthal, et al., "Image Formation for Coherent Diffuse Objects: Statistical Properties," J. Opt. Soc. Am., 60, 1478 (1970).
24. H. H. Arsenault, "Roughness Determination with Laser Speckle," J. Opt. Soc. Am., 61, 1425 (1971).

APPENDIX A

NOTES ON DISCUSSIONS ON SPECKLE THEORIES

On August 7, 1971 Dr. Robert B. Crane of Willow Run Laboratories came to SRI for a discussion on Laser Speckle Theory with Professor Joseph W. Goodman from Stanford University and Dr. Kamala S. Krishnan and Mr. Norman A. Peppers from SRI. Before this meeting the theory as developed by Crane¹⁹ and the theory as developed by Goodman^{10, 17} and Goldfischer¹⁸ were generally assumed to be incompatible inasmuch as the different approaches led to apparently different predictions when the expressions for power spectral density were evaluated for a specific example. The general purpose of the meeting was to examine in detail the published theoretical papers so that the nature of the discrepancies could be determined and a reconciliation of the different approaches could be effected. The notes of this meeting are appended below.

1. Summary of Discussions

The discussion began with Crane stating his criticism of Goldfischer's paper¹⁸. In essence:

- (1) For the case of coherent illumination, the contribution to the field from an infinitesimal area should be proportional to the area and not to the square root of the area as Goldfischer has stated. Thus Eq. (1) is incorrect. Crane provided a copy of a reply by Goldfischer to this criticism.
- (2) During the averaging process in Eq. (16) leading to Eq. (17), Goldfischer lost half his terms, which results in a factor of two error.
- (3) An extra $\Delta u \Delta v$ appears in Eq. (17).

It was agreed that statements (2) and (3) above were valid criticisms. A discussion of statement (1) above followed. Although it was agreed that the field contribution resulting from a coherent source is not proportional to the square root of the area of the source, Goodman suggested that provided the surface was very rough Goldfischer's averaging procedure would nevertheless yield the correct average result. He gave the analogy of adding independent noise voltage at a point and then summing on a power basis to obtain the average power. Crane stated that Goldfischer's procedure assumes the ensemble average and then calculates the average again.

A discussion of Goldfischer's Eq. (20) and Crane's¹⁹ Eq. (13) took place.

$$S(\omega, \Omega) = \frac{\alpha^2 \lambda^2}{32 \pi^4 h^2} \iint_{-\infty}^{\infty} du dv P(u, v) P\left(u - \frac{\lambda h \omega}{2\pi}, v - \frac{\lambda h \Omega}{2\pi}\right) \quad G(20)$$

$$S(\omega, \Omega) = \left| \iint_{-\infty}^{\infty} p(u, v) \bar{p}\left(u - \frac{\lambda h \omega}{2\pi}, v - \frac{\lambda h \Omega}{2\pi}\right) du dv \right|^2 \quad C(13)$$

where $P(u, v)$ is the power density incident on the diffuser at (u, v) and $p(u, v)$ is the field at (u, v) . Although $|p(u, v)|^2$ is proportional to $P(u, v)$, the two expressions are not identical. Goodman argued that if Crane's Eq. (13) were averaged over the ensemble, it would yield the same result as G(20) provided the surface was very rough compared with λ . This argument, in one dimension, proceeds as follows: Consider the diffuse surface as consisting of N correlation cells of length ℓ_c so that the integrand of Eq. (13) would be equivalent to a sum of $N - \frac{\lambda h \omega}{2\pi \ell_c}$ terms of the form $p(u) \bar{p}\left(u - \frac{\lambda h \omega}{2\pi}\right)$, each one being an independent complex number because the cells are uncorrelated. When $N - \frac{\lambda h \omega}{2\pi \ell_c}$ is a large number, the sum of the random numbers is equivalent to the random walk problem. If the surface is very rough compared with λ , the phase of each complex component of the walk is uniformly distributed on $(0, 2\pi)$, and a complex Gaussian random process results. The

square of the sum then obeys negative exponential statistics with a mean proportional to the number of random complex numbers. Thus, $\overline{S(\omega)}$ is proportional to the area of overlap of p and \bar{p} (shifted); that is, to the autocorrelation of the brightness distribution across the scattering spot. This is equivalent to Goldfischer's result. Therefore, it appears from the above argument that both $G(20)$ and $C(13)$ (averaged) would predict a triangle (Δ) power spectral density function and not (Δ^2) , for the special case of uniform coherent illumination of a rectangular aperture provided the surface roughness is much greater than λ .

Remarks similar to the above were made about Crane's Eq. (15) that deals with the Fresnel region. It was agreed that the presence of the additional deterministic phase factor would not affect the averaging procedure outlined by Goodman provided, of course, that the scattering surface was very rough compared to λ .

Crane showed a photograph of a speckle pattern obtained by illuminating a shirt fabric with laser light. He also showed a photograph of the Fourier transform of the speckle pattern and pointed out structure that he suggested contained information about the periodic nature of the fabric. It was agreed that the Fourier transform probably did contain this information but that more accurate information about the surface would be required in order to verify any particular theory.

Attention was given to the function $g(u,v)$ defined on page 1660 of Crane's paper. Crane remarked that some statements made in his paper concerning $g(u,v)$ were incorrect. The function $g(u,v)$ is to be interpreted as a combination aperture function and a function describing amplitude and phase changes upon reflection that are not accounted for by the path difference phase changes contained within $(R_1 + R_2)$.

There was a discussion of the assumptions about the reflected field implicit in Crane's Eq. (17). The implicit assumption is that the reflected

field can be described by a pure phase function. It was agreed that this approximation carries with it restrictions on the surface roughness and slope distribution and that the exact nature of these restrictions should be investigated.*

In the afternoon session, the apparent differences between the theories of Goodman¹⁰ and Crane were considered. To obtain the ensemble average autocorrelation function from Crane's treatment the expression $\overline{I(u_1, v_1) I^*(u_2, v_2)}$ must be evaluated, whereas, Goodman first calculates $\overline{E(u_1, v_1) E^*(u_2, v_2)}$ and makes use of the relationship

$$\overline{I(u_1, v_1) I^*(u_2, v_2)} = \bar{I}_1 \bar{I}_2 \left[1 + |\gamma(u_1, v_1; u_2, v_2)|^2 \right]$$

where γ is the normalized spatial coherence function. This approach is valid only when E has complex Gaussian statistics and therefore applies only to the case for which the surface roughness is large compared with λ . Thus, Goodman's theory should be compared with Crane's theory for the case where the surface is very rough.

*We have since examined this problem and have made some progress toward defining the conditions for which the approximation is valid. We have tentatively concluded that for normal incidence the approximation is valid when

$$\frac{\sigma}{\lambda} \leq \frac{R^2}{8 [(u-x)^2 + (v-y)^2]_{\max}}$$

where σ is the rms surface roughness, and R is the range to the observation point (Fresnel approximation). Further conditions are that the surface slopes should be less than about $\pm 30^\circ$ to the normal to the mean reference plane and that the local radius of curvature must be large compared with λ .

This led to a consideration of the approximations used by Crane in arriving at Eq. (39), and, in particular, the conditions that these approximations imposed on surface roughness. It was agreed that, subject to the conditions already mentioned, Crane's general Eq. (38) appeared to be correct. The validity of Eq. (39), however, depends both on the surface correlation length and the surface roughness. In the limiting case for which the surface correlation function is zero corresponding to a specular mirror, Eq. (39) predicts that the power spectral density has the form of a squared triangle function (Λ^2) when the illuminated aperture is a rectangle. This result agrees with both experience and diffraction theory applied to specular reflection. However, this is exactly the case for which Goodman's theory is inapplicable because his theory is valid only for surfaces much rougher than λ . In the other limiting extreme for which the surface roughness $\sigma^2 \Rightarrow \infty$, it was agreed that Eq. (39) was invalid.

The discussion then centered on the magnitude of the contribution to the integral of Eq. (38) for intermediate values of σ^2 . Goodman felt that the approximation used to obtain Eq. (39) from Eq. (38) -- namely, that the integrand becomes negligibly small for small strips along $u_1 = u - \frac{\lambda h \omega}{2\pi}$ -- may not be valid for intermediate values of σ^2 . In particular, he suggested that when $\sigma \gg \lambda$, an entirely different approximation to Eq. (38) might be required and suggested that in this case Eq. (38) might reduce to the Goodman-Goldfischer result. Goodman indicated that he would attempt to develop an approximation to Eq. (38) for this case.

There was a discussion of experiments that might be performed to clarify remaining theoretical difficulties. An experiment could be designed to measure the shape of the power spectral density function and to determine whether it was a triangle or a triangle squared function for a rectangular aperture. Goodman suggested that as the surface roughness went from very smooth to very rough a transition from a triangle squared to a triangle function might be observed. It was agreed that determining the shape of the power spectral density function near dc would be a more difficult experiment. Peppers suggested that the speckle pattern at large angles from the normal would have to be sampled in

order to obtain information about the power spectral density near dc. Consequently, this raises basic questions about the validity of all of the theories for large angles. It was agreed that the numerical aperture of the recording system should be great enough to resolve the surface irregularities.

The discussion then turned to the application of speckle pattern theory to remote sensing of the wave amplitude statistics of the sea. Peppers remarked that the angular distribution of the average intensity contains information about the surface statistics because the Fourier transform of the spatial coherence function at the surface relates it to the surface autocorrelation function. Furthermore, because the average intensity provides this information, he suggested that the temporal coherence of the laser is not being used for this measurement, and, in principle, an ordinary bright incoherent source would provide the same information. Goodman agreed, but pointed out that the Fourier transform relationship scales with λ ; and, therefore, the incoherent source should be quasi-monochromatic (filtered) to avoid an ambiguity in the Fourier transform.

Some thought was given to possible experimental configurations for collecting data from real seawater. For a diagnostic experiment from a floating platform, multiple detectors or a scanning boom could be used to measure the intensity distribution. For an experiment with an airborne platform, one is constrained to essentially monostatic angles; further theoretical work would be required to predict the results of scanning the monostatic angle.

2. Important Conclusions

The theories of Goodman and Goldfischer are inapplicable to relatively smooth surfaces. Crane's Eq. (39) is inapplicable to relatively rough surfaces but yields the correct result for relatively smooth surfaces. Crane's more general Eq. (38) is thought to be correct also for relatively rough surfaces -- subject to certain conditions stated in these notes. In the one case to which all theories were applied (see page A-2 of this Appendix) identical results were obtained.

APPENDIX B
COMPARISON OF VARIOUS THEORIES CONCERNING LASER SPECKLE
J. W. Goodman

1. Historical Background

After the operation of the first CW He-Ne laser, considerable interest arose in the speckled appearance of typical diffuse surfaces illuminated by coherent light. It was soon recognized that the origin of these granular patterns lay in the optical roughness of the surfaces from which the light was scattered.^{21, 22}

The first detailed statistical treatment of this phenomenon, now known as laser speckle, was that of Goodman.¹⁷ Treating the scattering or reflecting surface as a statistical ensemble of many point-scatterers with independent and uniformly distributed phases on $(0, 2\pi)$, Goodman showed, among other results, that the power spectral density (or Wiener spectrum) of the intensity pattern of reflected light was, up to scaling factors, identical with the autocorrelation function of brightness (i.e., intensity) distribution across the scattering spot.

Goldfischer¹⁸ independently derived the same result using essentially the same model as Goodman.¹⁷ Again the scatterers were assumed infinitesimal in size and independent and were taken to have phases uniformly distributed on $(0, 2\pi)$.

In an extension of his previous results, Goodman¹⁰ later discussed the properties of speckle patterns as they affect the performance of optical radars.⁶ In an appendix to this paper, he presented a generalized theory that allowed a finite correlation area to exist in the fields at the scattering surface. Thus, the assumption of infinitesimal scatterers was removed, but, significantly, the

phase of the scattered light at any point on the object was still assumed to be uniformly distributed on $(0, 2\pi)$. Hence, the theory applies only for surfaces that are quite rough on the scale of the wavelength of the illumination.

Following this early work that dealt with the intensity patterns existing in the scattered light, other investigators -- notably Lowenthal and Arsenault²³-- have studied the properties of similar patterns observed in the images of coherently illuminated diffuse objects. These treatments have assumed that the complex fields in the image plane obey circular Gaussian statistics, i. e., the real and imaginary parts of the field are zero mean, uncorrelated Gaussian random variables, with identical variances. Such an assumption is valid if the correlation area of the diffusely transmitted or reflected wavefront is small compared with the area of the point-spread function of the imaging system and if the phase of the light at each point on the object is approximately uniformly distributed on $(0, 2\pi)$. In the current discussion, we shall limit attention to speckle patterns observed by direct measurement of intensity in the scattered light, without any intervening optics. We shall, therefore, not be addressing the problem studied by Lowenthal and Arsenault.

The next important piece of work dealing with directly observed speckle patterns is that of Crane.¹⁹ He derives results that appear in various respects to conflict with earlier results of Goodman and Goldfischer.^{10,17,18} Crane's comments are directed at the paper by Goldfischer, but his chief criticism applies equally well to the work of Goodman. The chief criticism is as follows: Goldfischer assumes that the field produced by a small subsection of a diffuse surface is proportional to the square root of the area of that subsection; but for coherent light, the field must be directly proportional to the area because the field contributions add on an amplitude basis. Thus, Crane concludes that Goldfischer used a physically incorrect model and that this is the reason for the apparent differences between the results of the two theories. We should also point out that Crane's theory has the merit of allowing for a finite correlation area of the diffuse surface. Of the work preceding Crane's, only that of Goodman¹⁰ allowed for this possibility.

Crane's criticism of Goldfischer's work was answered in a letter by Arsenault.²⁴ Arsenault asserts that the differences between Goldfischer's and Crane's results arise because the former theory derives statistical average results while the latter is entirely a deterministic theory. Arsenault addresses his comments only to the early part of Crane's paper and in particular, to that portion through Eq.(16). In a later portion of the paper leading to Eq.(38) and (39), Crane has derived expressions for the statistical average power spectral density, the same quantity derived by Goldfischer. Important differences between the results of the two theories remained even in this case. Thus, Arsenault's comments do not fully explain the discrepancies between the two papers. As we shall see in a later section of this appendix, the major discrepancies arise from the fact that Goldfischer implicitly assumes that the standard deviation of the phase of the reflected wave is comparable with or larger than 2π radians, whereas Crane's final result, Eq.(39), only holds when the standard deviation of the phase is considerably less than 2π radians. Thus, Crane's final result holds only for relatively smooth surfaces.

2. Approximations and Assumptions Inherent in the Various Theories of Laser Speckle

All of the theories concerning laser speckle contain certain approximations. Here we wish to outline the approximations common to all theories and those which are specific to the various individual theories.

a. Approximations Common to all Theories

Past analyses of the properties of laser speckle patterns are by no means exact. All of the previous work mentioned is based on the scalar theory of diffraction and scattering, a theory which is accurate only when reasonably small diffraction angles are involved. Many diffuse reflectors scatter radiation into a wide cone of angles, so there will be cases in which the predictions of the scalar theory are not entirely accurate.

Most of the detailed analyses referred to have started with the Huygens-Fresnel principle stated here as Eq. (1).

$$E(x,y) = \frac{1}{j\lambda} \iint_{-\infty}^{\infty} \frac{E(u,v) e^{jk|\vec{r}_0 - \vec{r}|} \cos \varphi}{|\vec{r}_0 - \vec{r}|} dS \quad (B.1)$$

Here, $E(x,y)$ is the field at (x,y) in the observation plane, $E(u,v)$ is the field at (u,v) in the reference plane, \vec{r}_0 is the vector distance from the origin of (u,v) to the observation point (x,y) , \vec{r} is the vector distance from the origin of (u,v) to a point in the (u,v) plane, φ is the angle between \vec{r}_0 and the normal to the (u,v) plane, dS is the elemental area in the (u,v) plane, and k has the value $2\pi/\lambda$ where λ is the wavelength of the radiation used.

An approximation common to all past theories has been the so-called Fresnel approximation to the Huygens-Fresnel principle, in which the spherical secondary wavelets are approximated by quadratic-phase surfaces. In addition, the obliquity factor $\cos \varphi$ is generally replaced by unity, and the factor $\frac{1}{|\vec{r}_0 - \vec{r}|}$ in the denominator of Eq. (B.1) is usually replaced by the normal distance h between the mean scattering surface and the parallel observation plane. Such approximations are valid only in a limited region of the observation space.

Lastly, we note that all theories neglect the effects of shadowing of the surface profile. Thus, all points on the surface must be viewable from the observation and illumination points.

b. Assumptions in the Work of Goodman and Goldfisher

In addition to the general approximations mentioned above, two major assumptions are common to the early work of Goodman and Goldfisher.^{17,18} These assumptions are: (1) the correlation area of the diffusely reflecting surface is infinitesimal, and (2) the surface height fluctuations are of the order

of λ or greater, leading to a uniformly distributed phase associated with each elementary scattering area. Later work by Goodman¹⁰ showed that when the first assumption is removed,⁶ the correlation function of the scattered wave influences the mean distribution of intensity over the observation plane but does not influence the fine structure of the speckles themselves. The second assumption however, is more vital to the theory and can not be removed without major modifications.

We disagree with Crane's claim that the theories under discussion contain a fundamental flaw through the assumption that the power contributed by a scattering element is directly proportional to its area of that element rather than to the square of the area. In a deterministic treatment such as that in the early part of Crane's paper, amplitudes must surely be added. However, the results obtained (e.g., Crane's Eqs. (13) and (15)) are not very useful in deterministic form because the detailed functions $p(u,v)$ to be inserted cannot be specified. They are in fact sample functions of a random process. If the ensemble average power at a given point is to be calculated, then provided assumptions (1) and (2) above are satisfied, the average power contributed at a given point must indeed be directly proportional to the scattering area. We shall demonstrate in subsection 3 that Crane's results reduce to Goldfischer's results when assumptions (1) and (2) are satisfied.

c. Assumptions in the Work of Goodman

The primary assumption inherent in Goodman's generalized treatment is that the scattering surface is rough on the scale of a wavelength.¹⁰ This assumption enters through the assignment of circular complex Gaussian statistics to the scattered field at the observation point. Such statistics arise only when the scattered field components generate a complex random walk, with approximately uniform phase associated with the various field contributions. A phase distribution approximately uniform on $(0, 2\pi)$ will be observed only when the surface roughness is comparable with or greater than a wavelength. The Gaussian statistics of the fields are used in Goodman's Eq. (13), which specifies

the correlation function of the speckle intensity pattern in terms of the correlation function of the fields. This specific relation does not hold for non-Gaussian fields.

Goodman's Eq. (63) and (13) indicate that the autocorrelation function of the speckle intensity pattern $I(x,y)$ may be expressed as*†

$$\begin{aligned} R_{I_0}(x_1, y_1; x_2, y_2) &= \langle I(x_1, y_1) I(x_2, y_2) \rangle \\ &= \langle I(x_1, y_1) \rangle \langle I(x_2, y_2) \rangle \left[1 + |\gamma_0(\Delta x, \Delta y)|^2 \right] \quad (\text{B. 2}) \end{aligned}$$

where $\Delta x = x_1 - x_2$, $\Delta y = y_1 - y_2$. Here $\langle I(x,y) \rangle$ represents the distribution of mean intensity in the (x,y) observation plane and can be shown to be proportional to a scaled Fourier transform of the normalized autocorrelation function $\gamma_t(\Delta u, \Delta v)$ of the fields in an (u,v) plane that exists just above the scattering surface. The function $\gamma_0(\Delta x, \Delta y)$ represents a normalized autocorrelation function of the field in the (x,y) plane and can be shown to be a scaled Fourier transform of the brightness distribution across the scattering surface.

In applying these results, particularly when the surface structure information is of interest, we need to find some way to relate the surface height profile $w(u,v)$ to the autocorrelation function of the fields in the (u,v) plane just above the surface. In general, this is a nontrivial problem and we will discuss it in more detail when considering Crane's assumptions in the following section.

* We use here Crane's notation, with (x,y) variables in the observation plane and (u,v) variables in the target plane.

† Here we use the symbol $I(x,y) = E(x,y) E^*(x,y)$ for intensity. To convert in intensity to power density one must divide by $2z_0$ where $z_0 = 120\pi\Omega$ is the impedance of free space.

d. Assumptions and Approximations in the Work of Crane

Here we restrict attention to the one case in which Crane computed the average power spectral density in a speckle pattern generated by a random surface.¹⁹ No assumptions concerning the roughness of the surface are explicitly stated, but the surface height profile $w(u, v)$ is explicitly assumed to be a stationary Gaussian random process. Presumably, the standard deviation of this surface can vary from zero (a mirror surface) to infinity (an infinitely rough surface).

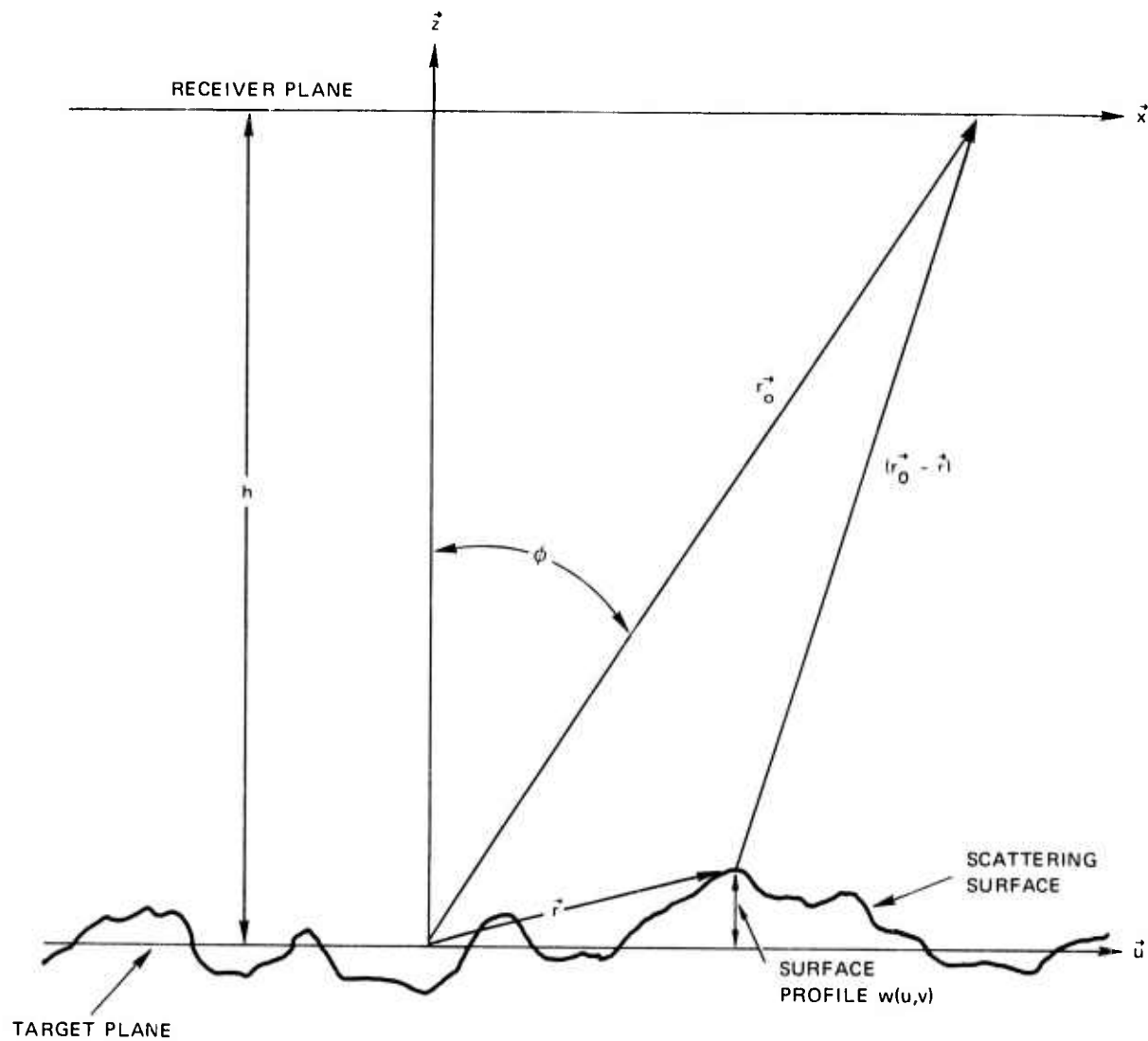
Crane uses the Fresnel approximation to the Huygens-Fresnel principle in making his calculations, using a field

$$p(u, v) = \exp \left\{ -j \frac{2\pi}{\lambda} [w(1 + \cos \phi)] \right\} g(u, v) \quad (\text{B.3})$$

where $g(u, v)$ is not carefully defined in the paper but is generally implied to be a positive and real-valued function, the square of which is proportional to the irradiance distribution incident on the surface. Crane explicitly uses $g(u, v)$ in this way in the example preceding the random-surface analysis (see his Eq. (26)).

Important approximations inherent in the use of Eq. (B.3) have been pointed out by N. Peppers in the course of this study. First, it neglects the variation of the Fresnel-reflection coefficient of the surface as the slope of the surface changes. Second, it neglects phase terms that can be important in some applications (including scattering from the ocean surface) when the speckle pattern is not observed directly above the scattering spot. To illustrate, with reference to Fig. B.1, the distance $|\vec{r}_0 - \vec{r}|$ from a point on the rough surface to a point (x, y) on the observation plane is

$$|\vec{r}_0 - \vec{r}| = \left[(h + w)^2 + (x - u)^2 + (y - v)^2 \right]^{1/2} \quad (\text{B.4})$$



SA-2422-11

FIGURE B-1 GEOMETRY AND COORDINATE SYSTEMS USED IN THE HUYGENS-FRESNEL PRINCIPLE

For simplicity, we define

$$A \triangleq \frac{(x-u)^2 + (y-v)^2}{h^2} \quad (\text{B.5})$$

and expand $|\vec{r}_0 - \vec{r}|$ in a binominal series, keeping only those terms of second order or lower in A and w .

$$\vec{r}_0 - \vec{r} \approx -w + \frac{hA}{2} + h - \frac{hA^2}{4} + \frac{wA}{2} \left(1 - \frac{3A}{4}\right) + \frac{w^2A}{2h} \left(1 - \frac{3A}{2}\right) \quad (B.6)$$

In Crane's approximation, all but the first two terms in this expansion are dropped. For a large class of practical problems, this results in sufficient accuracy, but when A/w is large, as in the case for scattering from the surface of the sea, dropping the remaining terms could lead to appreciable errors in estimating the field in the observation plane.

Lastly, we wish to discuss a subtle but important approximation in Crane's mathematics, which is responsible for the most dramatic conflict between Crane's results and those of Goodman and Goldfisher. This approximation arises in passage from Crane's Eq. (38) to his Eq. (39). We repeat Crane's Eq. (38), in slightly simplified notation, as follows:

$$E[S(\alpha, \Omega)] = \exp \left\{ -2\sigma_\beta^2 \left[1 - \rho_w \left(\frac{\lambda h \alpha}{2\pi}, \frac{\lambda h \Omega}{2\pi} \right) \right] \right\} \cdot \quad (B.7)$$

$$\cdot \iiint_{-\infty}^{\infty} \exp \left\{ \sigma_\beta^2 \left[2\rho_w(u - u_1, v - v_1) - \rho_w \left(u - u_1 + \frac{\lambda h \alpha}{2\pi}, v - v_1 + \frac{\lambda h \Omega}{2\pi} \right) - \rho_w \left(u - u_1 - \frac{\lambda h \alpha}{2\pi}, v - v_1 - \frac{\lambda h \Omega}{2\pi} \right) \right] \right\} \cdot g(u, v) g^*(u_1, v_1) \cdot g^* \left(u - \frac{\lambda h \alpha}{2\pi}, v - \frac{\lambda h \Omega}{2\pi} \right) g \left(u_1 - \frac{\lambda h \alpha}{2\pi}, v_1 - \frac{\lambda h \Omega}{2\pi} \right) du dv du_1 dv_1 \quad (B.8)$$

where

$$\sigma_\beta^2 = \left[\frac{2\pi}{\lambda} (1 + \cos \phi) \right]^2 \sigma_w^2$$

with ρ_w representing the normalized autocorrelation function of the surface height profile and ρ_w^2 representing its variance. Crane notes that the exponential factors differ from unity only in strips in the (u, u_1) and (v, v_1) planes that are narrow compared with the total area over which the g functions are nonzero. He assumes that the contribution from these narrow strips is negligible and replaces the exponential functions within the integrand by unity. The result is his Eq. (39),

$$E[S(\alpha, \Omega)] \simeq \exp \left\{ -2\sigma_\beta^2 \left[1 - \rho_w \left(\frac{\lambda h \alpha}{2\pi}, \frac{\lambda h \Omega}{2\pi} \right) \right] \right\} \cdot \left| \iint_{-\infty}^{\infty} g(u, v) g^* \left(u - \frac{\lambda h \alpha}{2\pi}, v - \frac{\lambda h \Omega}{2\pi} \right) du dv \right|^2 \quad (B.9)$$

The replacement of the exponential factors

$$\exp \left\{ -\sigma_\beta^2 \rho_w \left(u - u_1 + \frac{\lambda h \alpha}{2\pi}, v - v_1 + \frac{\lambda h \Omega}{2\pi} \right) \right\}$$

and

by

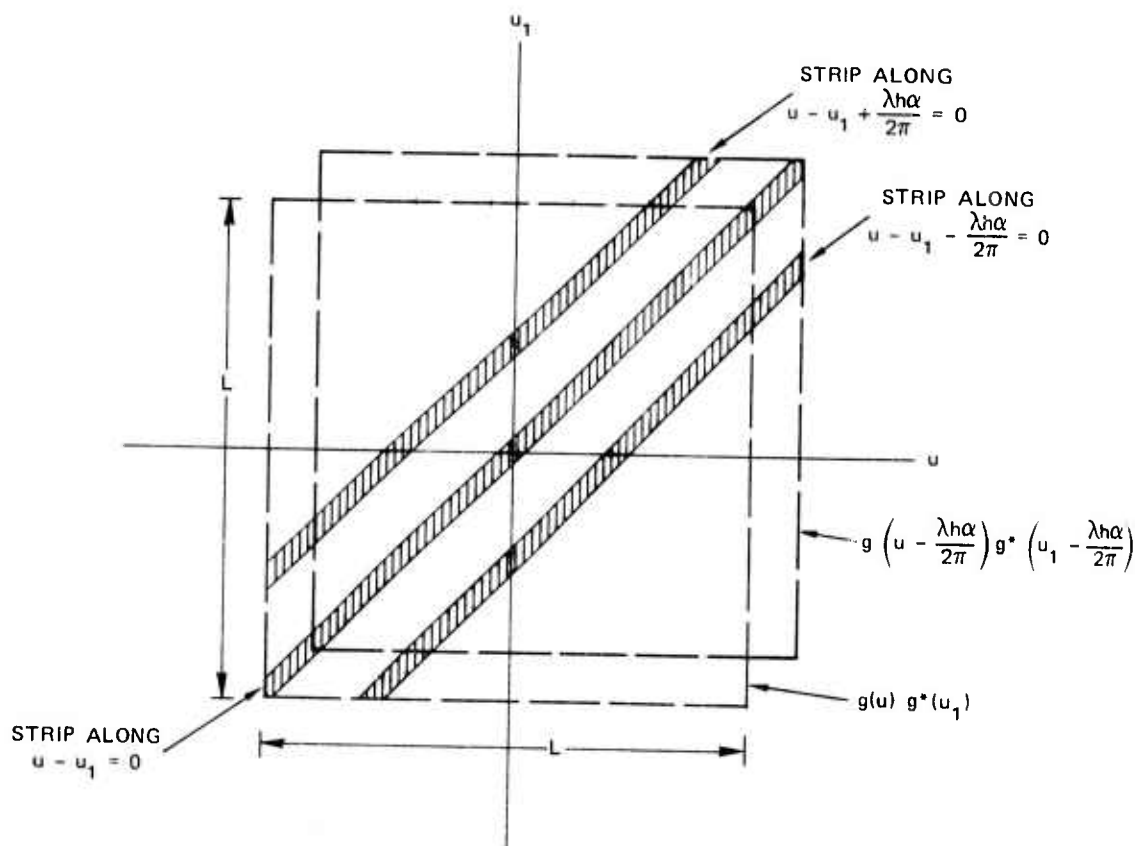
$$\exp \left\{ -\sigma_\beta^2 \rho_w \left(u - u_1 - \frac{\lambda h \alpha}{2\pi}, v - v_1 - \frac{\lambda h \Omega}{2\pi} \right) \right\}$$

unity is an excellent approximation because within the narrow strips where they differ from unity, they can at worst (large σ_β^2) drop toward zero. The change in the value of the integral resulting from these two strips will indeed be negligible.

However, the replacement of the term $\exp \left\{ 2\sigma_\beta^2 \rho_w(u - u_1, v - v_1) \right\}$ by unity involves a much more serious approximation, for when σ_β^2 is large, the value of this exponential becomes very large indeed. Although this factor differs from unity only in narrow strips in the (u, u_1) and (v, v_1) planes, it can nonetheless change the value of the integral if σ_β^2 is too large.

To analyze the exact restrictions on σ_β^2 , we find it convenient to consider a one-dimensional problem for which the quadruple integral of Eq. (B.7) reduces to a double integral. The results will then be generalized to the two-dimensional (quadruple integral) case. Figure B-2 shows the region of integration in the (u, u_1) plane, with the strips in question indicated, and the one-dimensional scattering spot assumed uniformly bright over a length L . As argued previously, the exponentials that drop toward zero in strips centered on

$$u - u_1 + \frac{\lambda h \alpha}{2\pi} = 0 \quad \text{and} \quad u - u_1 - \frac{\lambda h \Omega}{2\pi} = 0$$



SA-2422-16

FIGURE B-2 REGION OF INTEGRATION IN THE (u, u_1) PLANE SHOWING STRIPS WHERE VALUE OF $\exp \{2\sigma_\beta^2 \rho_w(u - u_1, v - v_1)\}$ DIFFERS FROM UNITY

Figure B-2. Region of Integration in the (u, u_1) Plane Showing Strips Where Value of $\exp \{2\sigma_\beta^2 \rho_w(u - u_1, v - v_1)\}$ Differs from Unity

can be replaced by unity. This leaves

$$E[S(\alpha)] = \exp \left\{ -2 \sigma_\beta^2 \left[1 - \rho_w \left(\frac{\lambda h \alpha}{2\pi} \right) \right] \right\} \cdot \int_{-\infty}^{\infty} \int_{-\infty}^{\infty} \exp \left\{ 2 \sigma_\beta^2 \rho_w(u - u_1) \right\} \cdot g(u) g^*(u_1) g^* \left(u - \frac{\lambda h \alpha}{2\pi} \right) g \left(u_1 - \frac{\lambda h \alpha}{2\pi} \right) du du_1 \quad (B.10)$$

To estimate the effect of the exponential term on the integral, we replace it by a flat-topped ridge of height $\exp \left\{ 2 \sigma_\beta^2 \right\}$, length $\sqrt{2} \left(L - \frac{\lambda h \alpha}{2\pi} \right)$ and width U . Here U represents the width (in the u -direction) over which the exponential factor differs significantly from unity. In general, U is somewhat larger than the correlation width of the random height variations. The volume under the broad flat-topped plateau of height unity [i.e., the plateau $g(u) g^*(u_1) g^* \left(u - \frac{\lambda h \alpha}{2\pi} \right) g \left(u_1 - \frac{\lambda h \alpha}{2\pi} \right)$] is $\left(L - \frac{\lambda h \alpha}{2\pi} \right)^2$. Thus, for the extra volume under the sharp ridge to be negligible, we require that

$$\exp \left\{ 2 \sigma_\beta^2 \right\} \sqrt{2} \left(L - \frac{\lambda h \alpha}{2\pi} \right) \sqrt{2} U \ll \left(L - \frac{\lambda h \alpha}{2\pi} \right)^2 \quad (B.11)$$

or

$$\sigma_\beta^2 \ll \frac{1}{2} \ln \left[\frac{\left(L - \frac{\lambda h \alpha}{2\pi} \right)}{2U} \right] \quad (B.12)$$

For the corresponding four-dimensional integral, the restriction becomes

$$\sigma_\beta^2 \ll \ln \left[\frac{\left(L - \frac{\lambda h \alpha}{2\pi} \right)}{2U} \right] \quad (B.13)$$

where an $L \times L$ scattering spot and a $U \times U$ correlation area have been assumed.

We now calculate an upper limit on the rms phase deviation σ_β^2 for Crane's Eq. 39 to be accurate at a frequency half way across the spectrum $(L - \frac{\lambda h \alpha}{2\pi}) = \frac{L}{2}$. We have

$$\sigma_\beta < \sqrt{\ln \left(\frac{L}{4U} \right)} \quad (B.14)$$

To calculate the largest allowable σ_β , we assume $L = 200\text{m}$ and $U = 0.5 \times 10^{-6}\text{m}$, which will lead to the largest bound that might be encountered in most practical cases. Substituting the numbers, we find the requirement

$$\sigma_\beta < 4.3 \text{ radians} \quad (B.15)$$

As a reasonable engineering approximation, Crane's result will be accurate if the rms surface deviation is no greater than about 0.2λ . Because of the logarithmic nature of the inequality in Eq. (B.14), the bound on σ_β is not very sensitive to the exact values used for L and U . Thus, Crane's Eq.(39) is valid only for relatively smooth surfaces. As we shall show later, for surface roughness greater than 0.2λ , Crane's Eq.(38) approaches Goldfischer's result except at very low frequencies.

3. An Extension of Crane's Results to Rough Surfaces

a. Analysis

As shown in the preceding section, Crane's Eq.(39) is valid only when the surface roughness does not exceed about 0.2λ in the most generous case. Here we wish to extend Crane's results to the case of truly rough surfaces, i.e., surfaces for which σ_β may be comparable with or greater than 2π radians. As a starting place, we use Crane's Eq.(38), which we believe to be valid for a Gaussian surface of any roughness, subject to the approximations stated in sections 2a and 2d. Thus,

$$\begin{aligned}
E[S(\alpha, \Omega)] = & \exp \left\{ -2\sigma_\beta^2 \left[1 - \rho_w \left(\frac{\lambda h \alpha}{2\pi}, \frac{\lambda h \Omega}{2\pi} \right) \right] \right\} \cdot \\
& \iiint \exp \left\{ 2\sigma_\beta^2 \left[\rho_w(u-u_1, v-v_1) - 1/2 \rho_w(u-u_1 + \frac{\lambda h \alpha}{2\pi}, \right. \right. \\
& \left. \left. v-v_1 + \frac{\lambda h \Omega}{2\pi}) - 1/2 \rho_w(u-u_1 - \frac{\lambda h \alpha}{2\pi}, v-v_1 - \frac{\lambda h \Omega}{2\pi}) \right] \right\} \cdot \\
& \cdot g(u, v) g^*(u_1, v_1) g^*(u - \frac{\lambda h \alpha}{2\pi}, v - \frac{\lambda h \Omega}{2\pi}) g(u_1 - \frac{\lambda h \alpha}{2\pi}, \\
& v_1 - \frac{\lambda h \Omega}{2\pi}) du dv du_1 dv_1
\end{aligned} \tag{B.16}$$

In approximating this equation, we find it necessary to concentrate separately on the cases of high frequency components $\left[\frac{\lambda h \alpha}{2\pi} \text{ and } \frac{\lambda h \Omega}{2\pi} \right]$ larger than the correlation width of ρ_w and low frequency components $\left[\frac{\lambda h \alpha}{2\pi} \text{ and } \frac{\lambda h \Omega}{2\pi} \right]$ less than the correlation width of ρ_w . Our attention will be focused first on the high frequency case.

For large σ_β^2 , the second and third exponential factors in the integrand approach zero only in narrow strips in the (u, u_1) and (v, v_1) planes but are unity elsewhere. They can be replaced by unity with little loss of accuracy. Furthermore, at high frequencies, we may replace the term $\exp \left\{ 2\sigma_\beta^2 \rho_w \left(\frac{\lambda h \alpha}{2\pi}, \frac{\lambda h \Omega}{2\pi} \right) \right\}$ by unity. Thus,

$$\begin{aligned}
E[S(\alpha, \Omega)] \simeq & \iiint \exp \left\{ -2\sigma_\beta^2 \left[1 - \rho_w(u-u_1, v-v_1) \right] \right\} \cdot \\
& \cdot g(u, v) g^*(u_1, v_1) g^*(u - \frac{\lambda h \alpha}{2\pi}, v - \frac{\lambda h \Omega}{2\pi}) g(u_1 - \frac{\lambda h \alpha}{2\pi}, v_1 - \frac{\lambda h \Omega}{2\pi}) \\
& du dv du_1 dv_1
\end{aligned} \tag{B.17}$$

Now we note that if σ_β^2 is large, the exponential function in the integrand is very narrow indeed. This function will, in fact, drop to zero for very small arguments of ρ_w . Thus, to determine the behavior of $E[S(\alpha, \Omega)]$ for large

σ_β^2 , we can replace ρ_w by its functional form near zero argument. For a wide class of autocorrelation functions, we can write

$$\rho_w(\xi, \eta) \approx 1 - a\xi^2 - b\eta^2 + c\xi\eta \quad (\text{B.18})$$

for small values of ξ, η . With a simple rotation of the (ξ, η) coordinate system, the cross term can be eliminated, and, therefore, we shall use the form

$$\rho_w(\xi, \eta) \approx 1 - a\xi^2 - b\eta^2 \quad (\text{B.19})$$

Such behavior near the origin is common to correlation functions of all random processes that have finite variances associated with their first derivatives. A notable case that violates this condition is the negative-exponential correlation function, which in the isotropic two-dimensional case may be written and approximated as follows:

$$\rho_w(\Delta r) = e^{-\frac{\Delta r}{R}} \approx 1 - \frac{\Delta r}{R} \quad (\text{B.20})$$

where $\Delta r = \sqrt{\xi^2 + \eta^2}$ and R is a constant.

We shall use the form of Eq. (B.19) in our calculations and simply state the result when Eq. (B.20) is used.

Using Eq. (B.19), we find

$$\exp \left\{ -2\sigma_\beta^2 \left[1 - \rho_w(u-u_1, v-v_1) \right] \right\} \approx \exp \left\{ -2\sigma_\beta^2 \left[a(u-u_1)^2 + b(v-v_1)^2 \right] \right\}. \quad (\text{B.21})$$

Next we note that, for large σ_β^2 ,

$$\exp \left\{ -2\sigma_\beta^2 \left[a(u-u_1)^2 + b(v-v_1)^2 \right] \right\} \approx \frac{2\pi}{4\sqrt{ab}\sigma_\beta^2} \cdot \delta(u-u_1) \delta(v-v_1) \quad (\text{B.22})$$

Substitution of Eqs. (B.21) and (B.22) in Eq. (B.17) yields the result

$$E[S(\alpha, \Omega)] \approx \frac{\pi}{2\sqrt{ab}} \sigma_\beta^2 \iint_{-\infty}^{\infty} |g(u, v)|^2 \left| g\left(u - \frac{\lambda h \alpha}{2\pi}, v - \frac{\lambda h \Omega}{2\pi}\right) \right|^2 du dv \quad (B.23)$$

where the sifting property of the δ -functions has been used to reduce the 4-D integral to a 2-D integral. The particular value of the constants a and b can be determined only when the form of the surface correlation function is specified. For the case of a negative exponential autocorrelation function of Eq. (B.20), we obtain

$$E[S(\alpha, \Omega)] \approx \frac{\pi R^2}{2\sigma_\beta^4} \iint_{-\infty}^{\infty} |g(u, v)|^2 \left| g\left(u - \frac{\lambda h \alpha}{2\pi}, v - \frac{\lambda h \Omega}{2\pi}\right) \right|^2 du dv \quad (B.24)$$

We shall shortly discuss the significance of the results of Eqs. (B.23) and (B.24) and compare them with the previous results of Crane and Goldfischer. First, however, we wish to consider just how large σ_β^2 must be for these equations to accurately represent the power spectral density. For simplicity, we consider only an isotropic correlation function that behaves as

$$\rho_w(\bar{\Delta}r) \approx 1 - d \bar{\Delta}r^2 + f \bar{\Delta}r^4 \quad (B.25)$$

near the origin. We wish to find the requirement on σ_β^2 to justify neglecting the $\bar{\Delta}r^4$ term. We have

$$\exp \left\{ -2\sigma_\beta^2 \left[1 - \rho_w(\bar{\Delta}r) \right] \right\} \approx \exp \left\{ -2\sigma_\beta^2 d \bar{\Delta}r^2 \right\} \exp \left\{ 2\sigma_\beta^2 f \bar{\Delta}r^4 \right\} \quad (B.26)$$

The maximum value of $\bar{\Delta}r$ for which the first exponential factor has significant value is

$$\bar{\Delta}r_{\max} \approx \frac{1}{\sqrt{2\sigma_\beta^2 d}} \quad (B.27)$$

For the second exponential factor to be negligible, we require

$$2\sigma_\beta^2 f \bar{\Delta r}_{\max}^4 \ll 1 \quad (\text{B. 28})$$

or

$$\sigma_\beta^2 \gg \frac{f}{2d^2} \quad (\text{B. 29})$$

Thus, $\sigma_\beta \gg \sqrt{\frac{f}{2d^2}}$ is a sufficient condition for our approximation to be accurate. For the particular case of a Gaussian correlation function

$$\rho_w(\bar{\Delta r}) = e^{-\left(\frac{\bar{\Delta r}}{R}\right)^2} \quad (\text{B. 30})$$

we have $d = R^{-2}$, $f = \frac{R^{-4}}{2}$, and the requirement for accuracy becomes

$$\sigma_\beta \gg \sqrt{\frac{1}{4}} = \frac{1}{2} \text{ radian} \quad (\text{B. 31})$$

Taking a factor of 4 to represent the condition much greater than, our results will be accurate if

$$\sigma_\beta \geq 2 \text{ radians} \quad (\text{B. 32})$$

or if the surface height fluctuations are greater than about 0.3λ .

We should also point out that a second approximation used in Eq. (B.22) exists in our analysis. However, this approximation turns out to be accurate for σ_β greater than a very small fraction of a radian, so the condition in Eq. (B.28) is the more stringent requirement.

Lastly, we turn to an approximation to Eq. (B.16) valid at low frequencies, i.e., frequencies for which $\frac{\lambda h \alpha}{2\pi}$ and $\frac{\lambda h \Omega}{2\pi}$ are smaller than the width of ρ_w . In this case, we have

$$\begin{aligned} \rho_w(u-u_1, v-v_1) - \frac{1}{2} \rho_w(u-u_1 + \frac{\lambda h \alpha}{2\pi}, v-v_1 + \frac{\lambda h \Omega}{2\pi}) \\ - \frac{1}{2} \rho_w(u-u_1 - \frac{\lambda h \alpha}{2\pi}, v-v_1 - \frac{\lambda h \Omega}{2\pi}) \approx 0 \end{aligned} \quad (B.33)$$

and

$$g^*(u - \frac{\lambda h \alpha}{2\pi}, v - \frac{\lambda h \Omega}{2\pi}) \approx g^*(u, v) \quad (B.34)$$

and

$$g(u_1 - \frac{\lambda h \alpha}{2\pi}, v_1 - \frac{\lambda h \Omega}{2\pi}) \approx g(u_1, v_1) . \quad (B.35)$$

It follows that

$$\begin{aligned} E[S(\alpha, \Omega)] \approx \exp \left\{ -2\sigma_\beta^2 \left[1 - \rho_w\left(\frac{\lambda h \alpha}{2\pi}, \frac{\lambda h \Omega}{2\pi}\right) \right] \right\} \cdot \\ \cdot \left| \iint_{-\infty}^{\infty} |g(u, v)|^2 du dv \right|^2 \end{aligned} \quad (B.36)$$

But we further note that for low frequencies, using Eq. (B.19) we have

$$\exp \left\{ -2\sigma_\beta^2 \left[1 - \rho_w\left(\frac{\lambda h \alpha}{2\pi}, \frac{\lambda h \Omega}{2\pi}\right) \right] \right\} \approx \exp \left\{ -2\sigma_\beta^2 \left[a\left(\frac{\lambda h \alpha}{2\pi}\right)^2 + b\left(\frac{\lambda h \Omega}{2\pi}\right)^2 \right] \right\} \quad (B.37)$$

for any correlation function ρ_w that behaves quadratically near the origin. Thus, near zero frequency, the power spectral density behaves as

$$\begin{aligned} E[S(\alpha, \Omega)] \approx \exp \left\{ -2\sigma_\beta^2 \left[a\left(\frac{\lambda h \alpha}{2\pi}\right)^2 + b\left(\frac{\lambda h \Omega}{2\pi}\right)^2 \right] \right\} \cdot \\ \cdot \left| \iint_{-\infty}^{\infty} |g(u, v)|^2 du dv \right|^2 . \end{aligned} \quad (B.38)$$

Thus, for a wide class of truly rough surfaces, the low frequency hump in the power spectral density has a Caussian shape, regardless of the particular shape of the surface correlation function.

b. Discussion and Conclusions

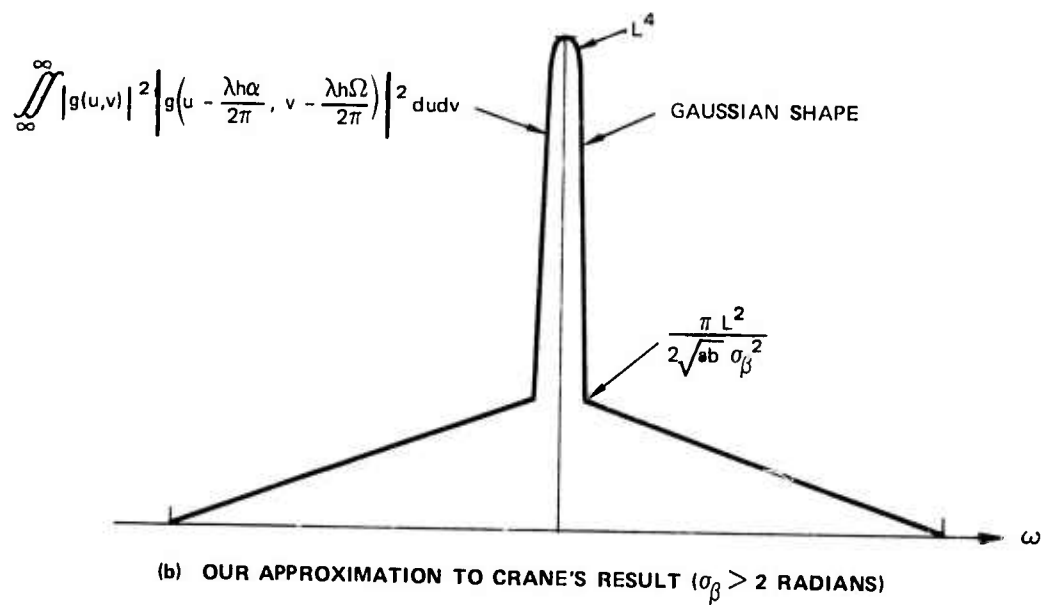
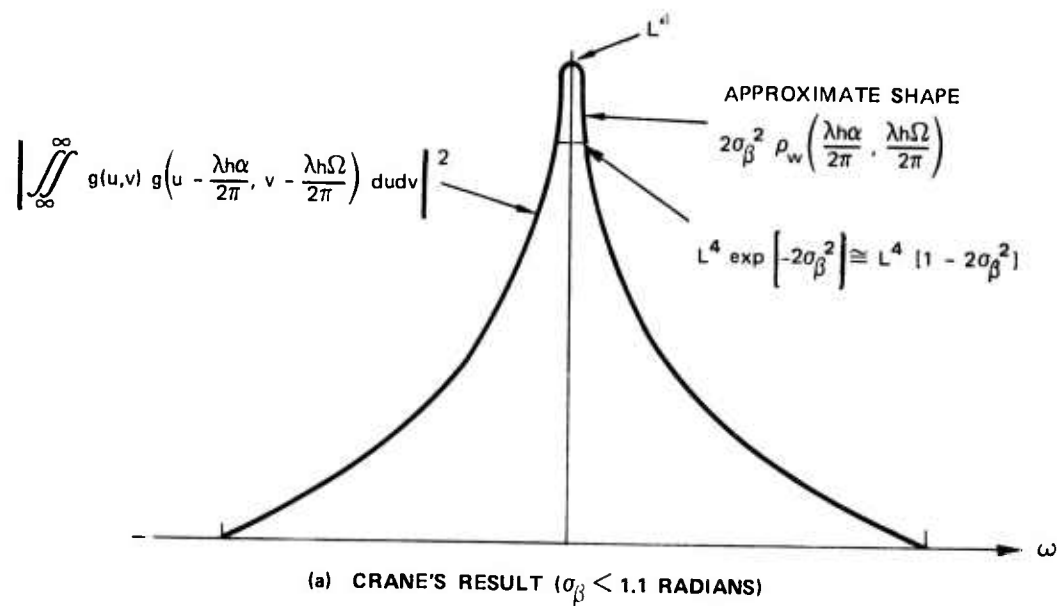
We have shown that Crane's Eq. (39) is valid only for relatively smooth surfaces, with surface roughnesses on the order of 0.2λ or less. On the other hand, we have found a new approximation to Crane's Eq. (38) valid only for rough surfaces, with roughnesses on the order of 0.3λ or greater. Figure B-3 illustrates the predictions in the two cases for a square, $L \times L$ scattering spot of uniform unit brightness. In the case of Crane's Eq. (39), σ_β^2 must be so small that the low frequency hump has the shape

$$\exp \left\{ -2\sigma_\beta^2 \left[1 - \rho_w \left(\frac{\lambda h \alpha}{2\pi}, \frac{\lambda h \Omega}{2\pi} \right) \right] \right\} \approx \left[1 - 2\sigma_\beta^2 \right] + 2\sigma_\beta^2 \rho_w \left(\frac{\lambda h \alpha}{2\pi}, \frac{\lambda h \Omega}{2\pi} \right) . \quad (\text{B.39})$$

Thus, information about the correlation function of the surface height variations is indeed contained in the very low frequency components of the power spectral density. However, this information is relatively weak in magnitude compared with the first term $\left[1 - 2\sigma_\beta^2 \right]$ in our Eq. (B.39) above.

If the surface roughness is large, again a hump exists in the low frequency portion of the power spectral density. The hump is larger compared with the higher frequency components in this case, but its shape is Gaussian, and detailed information about the surface correlation function cannot be derived from it, other than possibly the constants a , b , and σ_β^2 .

As for the high frequency components, Crane's approximation predicts that the power spectral density has the shape of the square of a triangle function



SA-2422-15

FIGURE B-3 CROSS SECTION OF POWER SPECTRAL DENSITY FOR $L \times L$ SQUARE SCATTERING SPOT

for a square scattering spot, whereas our approximation predicts a triangle function. Our approximation is in accord with the previous predictions of Goodman and Goldfischer,^{17,18} namely, that the power spectral density has the shape of the autocorrelation function of the brightness distribution across the scattering surface.

It is instructive to consider a numerical example to demonstrate how the shape of the expected value of the power spectral density changes as the surface roughness changes from very smooth to very rough. We use a symmetric Gaussian correlation function given by

$$\rho_w(\alpha, \Omega) = e^{-\frac{\Delta u^2 + \Delta v^2}{R^2}} = e^{-\left(\frac{\lambda h}{2\pi R}\right)^2 [\alpha^2 + \Omega^2]} \quad (\text{B.40})$$

and note that

$$\alpha_{\max} = \frac{2\pi L}{\lambda h} \quad \text{and} \quad \Omega_{\max} = \frac{2\pi L}{\lambda h} \quad (\text{B.41})$$

for an illuminated square $L \times L$. Thus,

$$\rho_w = e^{-\left(\frac{L}{R}\right)^2 \left[\left(\frac{\alpha}{\alpha_{\max}}\right)^2 + \left(\frac{\Omega}{\Omega_{\max}}\right)^2 \right]} \quad (\text{B.42})$$

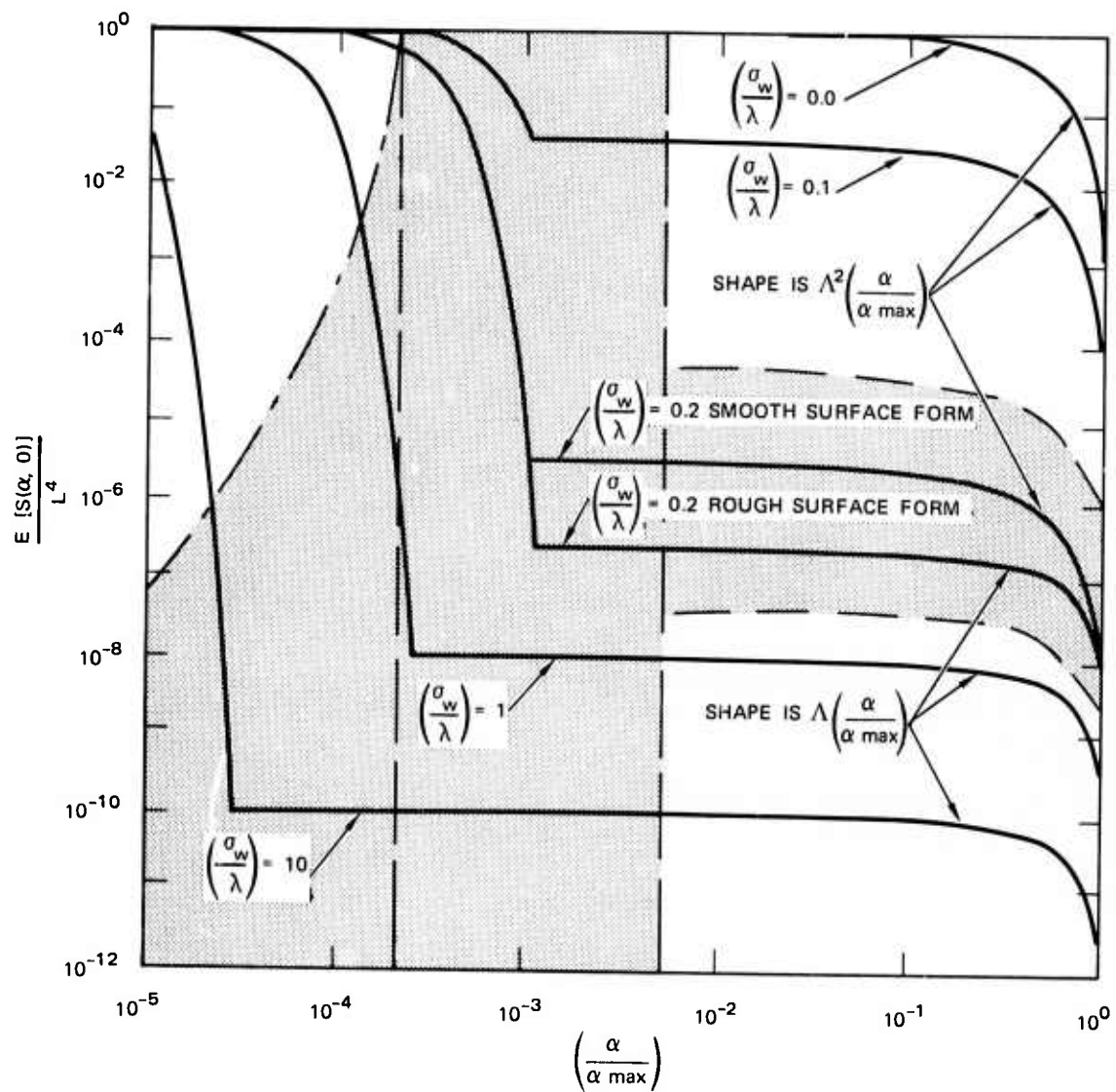
We now construct table B.1 to show the limiting forms of $E[S(\alpha, o)]$ for smooth and rough surfaces and use the reasonable numerical value 10^3 for (L/R) in these forms to plot the result in Figure B-4. Note that we have shaded regions of Figure B-4 for which our approximations are invalid and for which the exact shape of the power spectral density is unknown. Note also that the ordinate and abscissa are scaled differently.

LIMITING FORMS OF THE POWER SPECTRAL DENSITY FOR AN ILLUMINATED SQUARE SURFACE
L X L AND SURFACE CORRELATION LENGTH R

Table B. 1

Frequency	Smooth Surface ($\sigma_w < 0.2\lambda$)	Rough Surface ($\sigma_w > 0.3\lambda$)
Low Frequency $\alpha \ll \frac{2\pi R}{wh}$ or $\frac{\alpha}{\alpha_{\max}} \ll \frac{R}{L}$	$E[S(\alpha, 0)] \approx L^4 e^{-32\pi^2 \left(\frac{\sigma_w}{\lambda}\right)^2 \left(\frac{L}{R}\right)^2 \left(\frac{\alpha}{\alpha_{\max}}\right)^2}$	$E[S(\alpha, 0)] \approx L^4 e^{-32\pi^2 \left(\frac{\sigma_w}{\lambda}\right)^2 \left(\frac{L}{R}\right)^2 \left(\frac{\alpha}{\alpha_{\max}}\right)^2}$
High Frequency $\alpha \gg \frac{2\pi R}{\lambda h}$ or $\frac{\alpha}{\alpha_{\max}} \gg \frac{2\pi R}{\lambda L}$	$E[S(\alpha, 0)] \approx L^4 e^{-32\pi^2 \left(\frac{\sigma_w}{\lambda}\right)^2 \Lambda^2 \left(\frac{\alpha}{\alpha_{\max}}\right)^2}$	$E[S(\alpha, 0)] \approx \frac{L^4 \Lambda^2 \left(\frac{\alpha}{\alpha_{\max}}\right)^2}{32 \left(\frac{\sigma_w}{\lambda}\right)^2 \left(\frac{L}{R}\right)^2}$

Note: The symbol $\Lambda \left(\frac{\alpha}{\alpha_{\max}}\right)$ is used here to denote a triangle function having the value unity for zero argument and zero for unity argument.



SA-2422-17

FIGURE B-4 NORMALIZED POWER SPECTRAL DENSITY FOR SMOOTH AND ROUGH SURFACES FOR WHICH $(L/R) = 10^3$

The important conclusions to be drawn from the analysis of this appendix are summarized as follows:

- Equation(39) of Crane's paper is valid only for relatively smooth surfaces ($\sigma_w < 0.2\lambda$).
- When the surface is smooth enough to satisfy this requirement, information about the surface correlation function is present in the power spectral density function near zero frequency, but it may be difficult to extract.
- For surfaces smooth enough to satisfy this requirement, the high frequency portion of the power spectral density has a shape determined by the squared modulus of the autocorrelation of the square root of the brightness distribution across the scattering spot.
- For truly rough surfaces ($\sigma_w > 0.3\lambda$), our approximation to Crane's Eq. (38) is the proper result, and Crane's Eq. (39) is incorrect.
- For a truly rough surface, the low frequency components in the power spectral density function have a shape that depends only on the shape of the surface correlation function near zero argument. Detailed information on the exact nature of the surface correlation function is thus not derivable from the power spectral density.
- For a truly rough surface, the high frequency components of the power spectral density have a shape that is determined by the autocorrelation function of the brightness distribution across the scattering spot. Thus, for a truly rough surface, the previous predictions of Goodman and Goldfischer are correct.^{17,18}

Thus, the apparent contradictions between Crane's theory and those theories that preceded his have been reconciled by our analysis.

APPENDIX C
THE VALIDITY OF $\overline{I_1 I_2} = \overline{I_1} \overline{I_2} (1 + |\gamma|^2)$ FOR SPACE
VARYING COMPLEX GAUSSIAN PROCESSES

J. W. Goodman

Let $E(P_1) = x_1 + jy_1$, $E(P_2) = x_2 + jy_2$, where x_1, y_1 are independent, identically distributed Gaussian random variables, and x_2, y_2 have similar properties. Consider $\overline{I_1 I_2} = |E(P_1)|^2 |E(P_2)|^2$.

Now

$$\begin{aligned} I_1 I_2 &= \overline{(x_1^2 + y_1^2)(x_2^2 + y_2^2)} = \overline{x_1^2 x_2^2} + \overline{y_1^2 y_2^2} \\ &\quad + \overline{x_1^2 y_2^2} + \overline{y_1^2 x_2^2} \end{aligned} \quad (C.1)$$

Now using the result

$$\overline{z_1 z_2 z_3 z_4} = \overline{z_1 z_2} \overline{z_3 z_4} + \overline{z_1 z_3} \overline{z_2 z_4} + \overline{z_1 z_4} \overline{z_2 z_3} \quad (C.2)$$

valid for any four real, zero mean Gaussian random variables z_1, z_2, z_3, z_4 , we obtain

$$\begin{aligned} I_1 I_2 &= \overline{x_1^2 x_2^2} + \overline{2(x_1 x_2)^2} + \overline{y_1^2 y_2^2} + \overline{2(y_1 y_2)^2} + \overline{x_1^2 y_2^2} + \overline{2(x_1 y_2)^2} \\ &\quad + \overline{y_1^2 x_2^2} + \overline{2(y_1 x_2)^2} \end{aligned} \quad (C.3)$$

Assuming $\overline{x_1^2} = \overline{y_1^2} = \frac{1}{2} \overline{I_1}$, $\overline{x_2^2} = \overline{y_2^2} = \frac{1}{2} \overline{I_2}$.

$$\begin{aligned}\overline{I_1 I_2} &= \frac{1}{4} \overline{I_1} \overline{I_2} + 2R_X^2(1,2) + \frac{1}{4} \overline{I_1} \overline{I_2} + 2R_Y^2(1,2) \\ &+ \frac{1}{4} \overline{I_1} \overline{I_2} + 2R_{XY}^2(1,2) + \frac{1}{4} \overline{I_1} \overline{I_2} + 2R_{YX}^2(1,2)\end{aligned}\quad (C.4)$$

or

$$\begin{aligned}\overline{I_1 I_2} &= \overline{I_1} \overline{I_2} + 2R_X^2(1,2) + 2R_Y^2(1,2) \\ &+ 2R_{XY}^2(1,2) + 2R_{YX}^2(1,2)\end{aligned}\quad (C.5)$$

Now we must compare this result with

$$\overline{I_1} \overline{I_2} \left[1 + |\gamma(1,2)|^2 \right] \quad (C.6)$$

where

$$\gamma_{(1,2)} \triangleq \frac{(\overline{x_1 + jy_1})(\overline{x_2 - jy_2})}{\sqrt{\overline{I_1} \overline{I_2}}} \quad (C.7)$$

We find

$$\gamma_{(1,2)} = \frac{(\overline{x_1 x_2} + \overline{y_1 y_2}) + j(\overline{y_1 x_2} - \overline{x_1 y_2})}{\sqrt{\overline{I_1} \overline{I_2}}} \quad (C.8)$$

and therefore

$$|\gamma_{(1,2)}|^2 = \frac{\left[R_X(1,2) + R_Y(1,2) \right]^2 + \left[R_{YX}(1,2) - R_{XY}(1,2) \right]^2}{\sqrt{\overline{I_1} \overline{I_2}}} \quad (C.9)$$

Thus,

$$\begin{aligned} \bar{I}_1 \bar{I}_2 \left[1 + |\gamma(1,2)|^2 \right] &= \bar{I}_1 \bar{I}_2 + \left[R_X(1,2) + R_Y(1,2) \right]^2 \\ &+ \left[R_{YX}(1,2) - R_{XY}(1,2) \right]^2 . \end{aligned} \quad (C.10)$$

If we are to have

$$\overline{I_1 I_2} = \bar{I}_1 \bar{I}_2 \left[1 + |\gamma(1,2)|^2 \right] , \quad (C.11)$$

we must have equality of the right hand sides of Eqs. (C.5) and (C.10). This equality will hold if

$$R_X(1,2) = R_Y(1,2) \quad (C.12)$$

and

$$R_{YX}(1,2) = -R_{XY}(1,2) \quad (C.13)$$

Thus, it remains only to prove that these above relations hold. We can prove these relations if we assume that the surface is very rough; i. e. , that the phase of each scatter is uniformly distributed on $(0, 2\pi)$ and is independent of its strength. A proof of the crucial relations follows.

Let $A_n(1) e^{j\phi_n(1)}$ represent the amplitude and phase contributed at point P_1 by the n^{th} scatter. Thus,

$$E(P_1) = \sum_n A_n(1) e^{j\phi_n(1)} \quad (C.14)$$

$$E(P_2) = \sum_m A_m(2) e^{j\phi_m(2)} \quad (C.15)$$

where n and m range over all scatterers.

We first prove $R_X(1,2) = R_Y(1,2)$.

$$\begin{aligned} R_X(1,2) &= \overline{\sum_n A_n(1) \cos \phi_n(1) \sum_m A_m(2) \cos \phi_m(2)} \\ &= \sum_n \sum_m \overline{A_n(1) A_m(2)} \overline{\cos \phi_n(1) \cos \phi_m(2)} \quad . \quad (C.16) \end{aligned}$$

Now for $n \neq m$,

$$\overline{\cos \phi_n(1) \cos \phi_m(2)} = \overline{\cos \phi_n(1)} \cdot \overline{\cos \phi_m(2)} = 0 \quad (C.17)$$

by the assumption of independent scatterers and uniformly distributed phase.

Thus,

$$R_X(1,2) = \sum_n \overline{A_n(1) A_n(2)} \overline{\cos \phi_n(1) \cos \phi_n(2)} \quad . \quad (C.18)$$

Now,

$$\overline{\cos \phi_n(1) \cos \phi_n(2)} = \frac{1}{2} \overline{\cos [\phi_n(1) + \phi_n(2)]} + \frac{1}{2} \overline{\cos [\phi_n(1) - \phi_n(2)]} \quad . \quad (C.19)$$

Each ϕ_n consists of a random phase ψ_n^r because of the random phase of a scatterer, and a deterministic phase ψ_n^d from propagation delays.

Thus,

$$\phi_n = \psi_n^r + \psi_n^d \quad (C.20)$$

and

$$\overline{\cos [\phi_n(1) + \phi_n(2)]} = 0 \quad (C.21)$$

resulting from the addition of random phases, while

$$\overline{\cos [\phi_n(1) - \phi_n(2)]} = \cos [\psi_n^d(1) - \psi_n^d(2)] = \cos [\epsilon_n(1,2)] . \quad (C.22)$$

Thus,

$$R_X(1,2) = \frac{1}{2} \sum_n \overline{A_n(1) A_n(2)} \cos [\epsilon_n(1,2)] . \quad (C.23)$$

By identical arguments, using the identity

$$\overline{\sin \phi_n(1) \sin \phi_n(2)} = \frac{1}{2} \overline{\cos [\phi_n(1) - \phi_n(2)]} - \frac{1}{2} \overline{\cos [\phi_n(1) + \phi_n(2)]} , \quad (C.24)$$

we obtain

$$R_Y(1,2) = \frac{1}{2} \sum_n \overline{A_n(1) A_n(2)} \cos [\epsilon_n(1,2)] . \quad (C.25)$$

Thus, we have proved

$$R_X(1,2) = R_Y(1,2) .$$

To prove $R_{YX}(1,2) = -R_{XY}(1,2)$, a similar approach is used. We have (skipping obvious steps)

$$R_{YX}(1,2) = \sum_n \overline{A_n(1) A_n(2)} \overline{\sin \phi_n(1) \cos \phi_n(2)} \quad (C.26)$$

and

$$R_{XY}(1,2) = \sum_n \overline{A_n(1) A_n(2)} \cos \phi_n(1) \sin \phi_n(2) . \quad (C.27)$$

Finally noting

$$\overline{\sin \phi_n(1) \cos \phi_n(2)} = \frac{1}{2} \overline{\sin [\phi_n(2) + \phi_n(1)]} - \frac{1}{2} \overline{\sin [\phi_n(2) - \phi_n(1)]} \quad (C.28)$$

$$\overline{\cos \phi_n(1) \sin \phi_n(2)} = \frac{1}{2} \overline{\sin [\phi_n(2) + \phi_n(1)]} + \frac{1}{2} \overline{\sin [\phi_n(2) - \phi_n(1)]} , \quad (C.29)$$

we see

$$R_{YX}(1,2) = \frac{1}{2} \sum_n \overline{A_n(1) A_n(2)} \sin [\epsilon_n(1,2)] \quad (C.30)$$

and

$$R_{XY}(1,2) = - \frac{1}{2} \sum_n \overline{A_n(1) A_n(2)} \sin [\epsilon_n(1,2)] . \quad (C.31)$$

Thus,

$$R_{YX}(1,2) = - R_{XY}(1,2) \quad (C.13)$$

and

$$\overline{I_1 I_2} = \bar{I}_1 \bar{I}_2 \left[1 + |\gamma(1,2)|^2 \right] . \quad (C.11)$$